



Dipl.-Ing. Thomas Halbedl

**Low Frequency Neutral Point Currents on Transformer in
the Austrian Power Transmission Network**

DOCTORAL THESIS

to achieve the university degree of
Doktor der technischen Wissenschaften
submitted to

Graz University of Technology

Supervisor

Ao.Univ.-Prof. Dipl.-Ing. Dr.techn. Herwig Renner
Institute of Electrical Power Systems

Reviewer

Prof. Dr.-Ing. Peter Schegner
Institute of Electrical Power Supply – TU Dresden

Graz, January 2019

Abstract

A secure and reliable power supply is the first priority for transmission system operators. Therefore risk assessment has to be done, which ensures a safer power grid operation, to estimate any possible hazard and identify negative impacts on the transmission network. Instigated by unexpectedly higher noise level of some transformers in the field, investigations on very low frequency neutral point currents, especially on geomagnetically induced currents (GIC), were performed in the Austrian power transmission grid by the author of this thesis.

The thesis gives a brief overview of the space weather and the emergence of geomagnetic disturbances from solar wind. The geomagnetic impact-chain, starting with those disturbances down to the Earth ground effects, which results in GIC, will be further outlined. The GIC can be treated as quasi DC currents compared to the 50 Hz line frequency and enters the transmission grid through the direct-grounded neutral point of transformer. The negative repercussions of GIC flow through transformer for example transformer heating or half-cycle saturation effects, and consequences to other components in the transmission network are also pointed out in this work.

Further, a developed wide-area DC monitoring system is introduced to analyse the DC transformer neutral currents and the GIC distribution in the Austrian transmission network. The monitoring system is additionally implemented as a real-time web application, so the transmission system operator is able to observe the present DC flow at any time. Besides the GIC, other DC sources are identified from the monitoring system in the transformer neutral.

A key factor of this work is that several measurement units are simultaneously installed in different transformer neutrals in the investigated transmission system, most of them in the 400 kV, but also in the 230 kV system. Those data are used to evaluate the applied GIC simulation and validate the computed transformer neutral currents in both transmission system voltage levels.

The simulation model is used to compute the GIC distribution in the network and find endangered points in the transmission system. The modelling results are discussed and compared to the measured ones. It is observed that crucial and highly sensitive parameters for GIC modelling are the grounding resistances and earth conductivity structures. Therefore, one approach was attempted to determine the grounding resistances, based on the transformer neutral current measurements, for higher correlations between measurements and simulations. Beyond that another step forward is presented to determine the earth conductivity, respectively the earth structure, from the transformer neutral current measurements.

Keywords:

DC monitoring system, geomagnetically induced currents (GIC), plane-wave method, power transmission grid, transformer half-cycle saturation

Affidavit

I declare that I have authored this thesis independently, that I have not used other than the declared sources/resources, and that I have explicitly indicated all material which has been quoted either literally or by content from the sources used. The text document uploaded to TUGRAZonline is identical to the present doctoral thesis.

Date

Signature

Table of Contents

i.	List of Abbreviations	VII
ii.	List of Symbols	VIII
1	Introduction.....	1
1.1	General	1
1.2	Scope of Research	2
1.3	Research Questions	3
1.4	Outline of the Thesis	3
2	Literature Survey.....	5
2.1	Space Weather.....	5
2.1.1	Solar Cycle	5
2.1.2	Solar Wind	5
2.1.3	Earth's Magnetosphere.....	6
2.1.4	World Magnetic Field	8
2.2	Ground Effects of Space Weather.....	9
2.3	Historical Impacts of Space Weather	10
2.4	GIC Effects on Power Transformers and Human Infrastructure.....	13
2.4.1	General on Transformers.....	13
2.4.2	Consequences of DC/GIC Saturation Effects on Transformers	21
2.4.3	GIC Effects on other Power Systems Utilities	25
2.4.4	GIC Effects on Pipelines	26
2.5	GIC Mitigation Techniques.....	26
2.5.1	GIC Blocking and Mitigation Devices.....	27
2.5.2	Operational Risk Management.....	28
2.6	International GIC Research and Working Groups	30
2.6.1	NERC	30
2.6.2	EURISGIC	30
2.6.3	IEEE Guide	31
2.6.4	CIGRE Working Group	31
2.7	Summary	32
3	Geomagnetic Field Measurements and Activity Indices.....	33
3.1.1	Magnetic Field Data.....	33
3.1.2	Geomagnetic Indices.....	33
3.2	Summary	36

4	Field Measurements of Transformer Neutral Currents	37
4.1	General on DC Monitoring System.....	37
4.2	Measurement Unit.....	38
4.2.1	Current Probe	38
4.2.2	Signal Filter.....	39
4.2.3	Processor Unit and Data Logger	43
4.2.4	Investigations on External Impacts on the Measurement Unit.....	43
4.2.5	Installation Point in the Field	44
4.3	Communication.....	45
4.4	Location of Installed Measurement Units in the Austrian Transmission System ...	46
4.5	Summary	47
5	Field Measurement Analysis.....	48
5.1	Data Analysis Methods	48
5.1.1	Digital Signal Processing	48
5.1.2	Stochastic Method.....	50
5.2	Analysis of the Measurement.....	53
5.2.1	Stochastic Analysis of the DC Field Measurements	54
5.2.2	Auto-Correlation of the DC Field Measurements	56
5.2.3	Fourier Transform of the Measurements.....	57
5.3	Root Cause Analysis	60
5.3.1	Geomagnetic Field Influence	60
5.3.2	Human Sources	62
5.3.3	Photoelectric Effect.....	63
5.4	Summary	64
6	GIC Simulation Method and Analysis.....	66
6.1	Introduction	66
6.2	Geophysical Model	69
6.2.1	General on Electromagnetic Fields for Geomagnetic Induction	69
6.2.2	Earth Conductivity Model.....	71
6.2.3	Plane-wave Method.....	73
6.3	Power System Model	75
6.3.1	Fundamentals in GIC Driving Source Implementation.....	75
6.3.2	Power Network Model	76
6.3.3	Calculation of GIC using Network Theory	80
6.4	Application of the Modelling Method on the Austrian Transmission System.....	84
6.4.1	Surface Impedance	84
6.4.2	Geoelectric Field	84

6.4.3	Transformer Neutral Currents of Simulation and Measurements	87
6.5	GIC Distribution and Sensitivity Analysis.....	92
6.5.1	GIC Distribution.....	92
6.5.2	Critical Geoelectric Field Directions.....	93
6.5.3	Transformer Neutral Grounding Sensitivity	97
6.6	Reverse Calculation of System Parameters.....	98
6.6.1	Indirect Determination of the Substation Grounding Resistances	98
6.6.2	Indirect Determination of the Surface Impedance	99
6.7	Summary	105
7	Conclusion and Future Work	106
8	References.....	110

i. List of Abbreviations

AC	alternating current
ACF	auto-correlation function
ACSR	aluminium core steel reinforced
ADC	analog-to-digital converter
CCF	cross-correlation function
CIGRE	Conseil International des Grands Réseaux Électriques
CIM	complex-image method
CME	coronal mass ejection
DC	direct current
DFT	discrete Fourier-Transformation
ECDF	empirical cumulative distribution function
EURISGIC	European Risk from Geomagnetically Induced Currents
FFT	Fast Fourier-Transformation
GIC	geomagnetically induced currents
GMD	geomagnetic disturbances
GSR	global solar radiation
HTLS	high-temperature low-sag
HV	high-voltage
HVDC	high-voltage direct current
IAGA	International Association of Geomagnetism and Aeronomy
IDFT	inverse discrete Fourier-Transformation
IEEE	Institute of Electrical and Electronics Engineers
IGRF	International Geomagnetic Reference Field
IMF	Interplanetary magnetic field
lat, lon	latitude, longitude
LV	low-voltage
NERC	North American Electric Reliability Corporation
opamp	operational amplifier
p.u.	per unit
RMS	root mean square
TSO	transmission system operator
UT	Universal Time
UTC	Universal Coordinated Time
var	reactive power
WDC	world data center
WIC	international code for the Conrad Observatory
WMM	World Magnetic Model

ii. List of Symbols

α	internal gain
α_E	angle of the horizontal geoelectric field
α_n	reflexion coefficient
β_0	ordinate intersection of the trend line
β_1	gradient of the trend line
γ_n	propagation constant of layer n
δ	penetration depth
ε	electric permittivity
ε_0	electric permittivity of the free-space
ε_r	relative electric permittivity
ζ	damping constant
Θ	magnetomotive force
Λ	permeance
μ	magnetic permeability
μ_0	magnetic permeability of the free-space
μ_r	relative magnetic permeability
μ_x	expectation value
ν	ordinal number of the harmonic components
ρ	charge density per unit volume
σ	conductivity
σ_n	conductivity of layer n
σ_{opt}	optimised conductivity
σ_x	standard deviation
τ	time-shift
φ	phase shift
Φ	magnetic flux
ω	angular frequency
ω_1	fundamental frequency
ω_c	cut-off angular frequency
ω_n	normalised angular frequency
$ \underline{A} $	magnitude of the gain response
$A(s_n)$	transfer function
A	cross-section
A_0	passband gain at DC
A_p	linear geomagnetic activity index (average daily mean value)
\mathbf{B}	magnetic field
B_F	total geomagnetic field intensity
B_H	horizontal geomagnetic field intensity
\mathbf{B}_r	remanence
B_x, B_y, B_z	northward, eastward and vertically downward geomagnetic field component
BNM	weighted branch-node matrix
BNM_{Lin}	weighted line branch-node matrix

BNM_{Sub}	weighted substation branch-node matrix
BNM_{Tra}	weighted transformer branch-node matrix
BNM_{Tra}^{DC}	reduced transformer branch-node matrix
C	system network matrix
C_{Tra}^{DC}	reduced transformer system network matrix
$Cov(X, Y)$	covariance
D	electric field strength
Dst	disturbance storm time index
E	electric field
$E(X)$	expectation value
E^{DC}	geoelectric field from DC measurement
E_{1n}, E_{2n}	vertical component of electric field to cross-section
E_H	horizontal geoelectric field
E_x, E_y	northward and eastward geoelectric field
E_x^{DC}, E_y^{DC}	northward and eastward geoelectric field from DC measurement
$F(x)$	distribution function
H	magnetic field strength
H_c	magnetic coercitivity
I	electric current
I_0	no-load current
I_1, I_2'	primary and secondary currents
I_c	core-loss current
I_m	magnetising current
I_{Lin}	line currents
I_{RMS}	effective value of the current
I_{Sub}	total substation (grounding) currents
I_{Tra}	transformer (winding) currents
I_{Tra}^{DC}	measured transformer neutral current matrix
J	electric current density
K	local geomagnetic activity index
K_p	global geomagnetic activity index
K_s	standardised geomagnetic activity index
L	inductance
L_x, L_y	distance between substations in northward and eastward direction
N	number of samples
N_1, N_2	primary and secondary nominal number of turns
N_B	total amount of branches in the power grid network
N_{Lay}	total amount of horizontal layers
N_{Lin}	amount of transmission lines
N_N	total amount of network nodes
N_{Net}	amount of network nodes without the grounding nodes
N_{Sub}	amount of substations
N_T	number of turns
N_{Tra}	amount of transformer windings
$P(X \leq x)$	probability of the event
P_{Cu}	coper loss

P_{Fe}	no-load loss
Q_i	quality factor
R_1, R'_2	primary and secondary winding resistances
$R_{G,opt}$	optimised substation grounding
$R_{Y(X)}$	linear trend line
R_b	resistance of the branch
R_c	core-loss resistance
R_m	reluctance
T_s	sample interval
$\underline{U}_1, \underline{U}'_2$	primary and secondary voltages
U_{emf}	electromotive force
V_1, V_2	potential of P_1 and P_2
V_{21}	voltage between points P_1 and P_2
V_N	network nodal voltages
V_S	driving voltage source
$Var(X)$	variance
W_N	basis function
$X_{\{k\}}$	spectral values
X_1, X'_2	primary and secondary winding leakage reactances
X_m	magnetising reactance
Y	admittance matrix
Y_C	coupling admittance matrix
Y_G	grounding admittance matrix
Y_N	network admittance matrix
Z	total earth impedance
Z^{DC}	total surface impedance from DC measurement
Z_{0n}	intrinsic impedance of layer n
Z_m	earth impedance of half-space bottom layer m
Z_n	impedance of layer n
Z_{xy}^{DC}, Z_{yx}^{DC}	total surface impedance in xy-component from DC measurement
$Z_{\sigma opt}$	total surface impedance to optimise
a_0	DC Fourier coefficient
a_i, b_i	filter coefficient (positive, real)
a_p	linear geomagnetic activity index (3 h time period)
a_v, b_v	Fourier coefficients
d_n	thickness of layer n
e	residual
emf	electromotive force
Δf	frequency resolution
$f(x)$	density function
f_c	cut-off frequency
$f_{c(-3dB)}$	cut-off frequency for -3 dB condition
f_{max}	highest frequency component in the signal
f_s	sample frequency
k	spectral component index
l	path length

m	filter order
n	sample index
r_{XX}	auto-correlation coefficient
r_{XY}	cross-correlation coefficient
r_{n+1}	reflexion coefficient
s	complex frequency variable
s_n	normalised complex frequency variable
$t.r.$	turns ratio
$w[n]$	window function
\bar{x}	arithmetic mean value
$x_{\{n\}}$	sample values
x_i	data vector

1 INTRODUCTION

This section covers a general overview of the thesis. It will highlight the topics which are treated, defining the basic framework, list the scope of research and research questions and also outline what will not be addressed in the work.

1.1 General

One of the challenging topics for the last decades - and for the future - is the continuous increase of power demand and therefore the capacity of the transmission system progressively reaches their limits. Especially the energy revolution and decision of many federal governments in Europe to increase the renewable energy sources while at the same time the generation from fossil and nuclear power plants stagnate or decrease. The withdrawal of fossil or nuclear generation means that other alternative energy generations from solar, wind, biomass, etc. supposed to increase and compensate the missing base load in the power transmission grid. Consequently, because the generation from renewable energies is cheaper compared to the conventional ones, the demand from such sources in the electricity market increase and suppress the conventional from the market energy generation.

However, the repercussions of installing renewable energy generation to the power grid are well known. One topic is the volatility of power generation in contrast to any conventional power. Energy generation from wind or solar is naturally weather-dependent and therefore conventional energy generation is still needed to stabilise the power network.

Measures to stabilise the transmission grid in the event of high generation peaks from renewables are phase shifting transformers or flexible AC transmission systems or redispatch actions. To reduce the overload in the network, power plants close to the consumption are instructed from the grid operator to generate more energy as they originally planned. Due to the balance between consumption and production, renewable sources decrease their production, which results in load-flow-distribution improvements in the transmission grid. These are one of the many challenges to handle of the transmission system operator (TSO). Therefore, the task for TSOs is to ensure security and reliability of the power transmission grid. Besides that, additional risk assessment of human activity or natural phenomena has to be done to identify possible further impacts on the system. Regarding the assessment and identification of potential risks, system protection strategies and implementation of countermeasures can be developed to protect the system and avoid/minimise the hazard.

Space Weather Impact

Based on assumptions to load flow increase and therefore higher stress of network components, any additional incident to the power system should be prevented. During commissioning of a new transformer in the Austrian transmission system, an unexpected higher noise level from the transformer was recognised compared to laboratory tests. After performing some noise measurements, investigations of the signal spectral analysis revealed that not only frequency components with double-time of line frequency and integral multiple (100 Hz, 200 Hz, etc.), but also line frequency and odd integral multiple (50 Hz, 150 Hz, etc.) were visible which indicate the presence of a DC source. A first research project in Austria [1] took measurements of the neutral point current at one transformer and confirmed the presence of a DC component respectively extreme low frequency component. Due to the fact that there are no DC sources close to the substation, neither DC railway systems nor high-voltage direct current (HVDC) lines, the

only plausible explanation for the DC occurrence was the occurrence of geomagnetically induced currents. Further research confirmed the theory of GIC that originate from disturbances of the geomagnetic field and can enter the transmission system via the direct-grounded neutral points of the transformers. The GIC are characterised in the literature by extremely low frequencies of less than 1 Hz. It is pointed out later in the thesis, that the significant GIC frequency spectrum is even below 1 mHz. Due to the very low frequency, the GIC can be defined as quasi DC compared to the line frequency currents of 50 Hz.

The presence of the DC causes an additional stress to the transformer, which means for example transformer heating up to half-cycle saturation effects. When the transformer operates saturated, the magnetising current rises non-linearly, which leads on the one hand to higher harmonics and on the other hand to an increase in reactive power consumption and therefore a system voltage decrease. In combination with the previously higher stress level from overload conditions or adversely switching condition of the power system, this can lead to network stability problems, tripping of transformers or other network utilities up to system blackouts, which has already been reported in the past.

1.2 Scope of Research

The aim of this doctoral thesis is to deepen the knowledge of GIC-related issues in the transmission system, understanding of the physics of space weather and the effects of geomagnetic disturbances (GMD) on infrastructure in Austria. In order to illustrate the consequences of GMD events, a simulation model is to be set up to compute the geoelectric field on the earth's surface.

In a first step, a GIC monitoring system to quantify the DC transformer neutral currents in Austria is developed. The monitoring system consists of different located measurement systems designed as a long-time recording system. Derived from the data, the amplitudes and their distributions of DC neutral current levels during days, months or years should give a better understanding of GIC behaviour. Besides the quantitative determination of the currents, the measurements should be applied to evaluate and adjust the GIC simulation model for the Austrian transmission grid.

Another important aim according to the geoelectric field calculation is to determine an appropriate model of the earth conductivity and geological structure of Austria. A representative earth conductivity model is needed to compute realistic geoelectric fields on the earth's surface. Beyond that, it is required for performing reliable GIC simulations in Austria by using the power network model. The GIC simulation model is utilised on the one hand, to compute the flow and distribution of GIC through the transmission grid and on the other hand, to perform risk assessment of the power grid, to figure out endangered points where high GIC can occur and therefore the potential for transformer saturation effects rises.

A further main topic is the indirect determination of the substation grounding resistances and earth conductivities, based on the transformer neutral current measurements. The goal of this approach is to get more realistic parameters for the GIC simulation model and therefore higher correlations between measurement and simulation.

The principal approach of the GIC simulation method can be applied to any large scale conductive infrastructure like power transmission grids, railway systems or pipelines. This study focuses mainly on GIC in power systems, in particular on GIC in the Austrian power transmission grid.

Although a general overview of GIC countermeasures and mitigation strategies is outlined and discussed, this work does not deal with the development or field installation of those devices. Additionally not included in the thesis are load flow investigations to the transmission system.

1.3 Research Questions

The research questions of the thesis are listed as follows

- Low-frequency neutral point currents on transformers in Austria
 - What are the amplitudes and their distribution?
 - What is the typical spectral distribution?
- What are the sources of the very low frequency transformer neutral currents?
- How significant is the impact of geomagnetically induced currents in the power transmission grid for a mid-latitude region like Austria?
- What earth conductivity model is valid for Austria and how reliable are the computations compared to the measurements?
- Where are the endangered points in the Austrian transmission grid based on simulations?
- Is it possible to determine reliable values of specified simulation model parameters based on the transformer neutral current measurements?

1.4 Outline of the Thesis

A brief explanation of the thesis topics will be mentioned hereinafter.

Section 2 Literature Survey

The literature survey gives an overview of the fundamentals of the space weather and the interaction between solar storms and geomagnetic disturbances. Furthermore, the basics of space weather ground effects, which act as the driving source of GIC, and the distribution of the geomagnetically induced currents in the power transmission grid are explained. The impact of GIC on power transformer due to half-cycle saturation and consequences like mechanical vibrations, thermal losses or rise of harmonics are outlined. Mitigation strategies as blocking devices or operational management for TSOs are discussed and a selection of international GIC research studies conclude the section.

Section 3 Geomagnetic Field Measurements and Activity Indices

This section deals with the 3-dimensional geomagnetic field data and various geomagnetic activity indices, which are used for this thesis. The K_p index, which is common to describe the geomagnetic activity, is described in detail.

Section 4 Field Measurements of Transformer Neutral Currents

This chapter deals with the developed DC live monitoring and recording system. The challenges and boundary conditions for reliable transformer neutral current measurements are outlined and the realisation of the monitoring system with an appropriate measurement unit is described. Further the geographic locations of the measurement units in the Austrian transmission grid are outlined in this chapter.

Section 5 Field Measurement Analysis

Field measurements of the transformer neutral current and geomagnetic field are presented and, based on statistical methods and Fourier transform, the data are analysed in detail. Besides the determination of the characteristic frequency spectrum of geomagnetic field variations, root cause analysis of the transformer neutral currents are performed, focussing on the human influence and other physical effects.

Section 6 GIC Simulation Method

Starting with an overview of GIC simulation methods, a categorisation between geophysical and power system model is defined for computation. The geophysical model explained the applied simulation approach based on the plane-wave method, which requires the geomagnetic field and 1D-earth conductivity layers as an input parameter to compute the geoelectric field on the earth's surface. The power system model considers the implementation of the GIC driving source (geoelectric field) in the network model and the application of network theory for computations.

Additional analysis of the simulations and a comparison with the measurements, to validate the simulation model, are outlined. Further investigations consist of the GIC distribution and therefore detect endangered points in the investigated area, the geoelectric field sensitivity of substations and the effect of transformer outages on GIC network distribution. The chapter concludes with the optimisation and indirect determination of the substation grounding parameter and earth conductivities, based on the transformer neutral current measurements.

Section 7 Conclusion and Future Work

This section covers the conclusion and further answering the formulated research questions. An outlook of possible future investigations concerning the thesis topic finalises the work.

2 LITERATURE SURVEY

This chapter outlines the literature and topics that are relevant to this thesis. It describes the geophysical part like solar cycles, the effects of solar winds on the geomagnetic field and therefore impacts of geomagnetic disturbances on the human infrastructure. The section covers a general overview of the geomagnetic ground effects on power transmission systems and the impacts on transformers caused by GIC. Some mitigation strategies to avoid the flow of GIC in the transmission system and suggestions for TSOs to minimise the risk of voltage instability during strong geomagnetic disturbances.

2.1 Space Weather

Following this, the most important phenomena of space weather are briefly outlined. It concludes solar flares, coronal mass ejections (CME) of the sun and the interaction between the Earth's magnetosphere and the solar wind.

2.1.1 Solar Cycle

Sunspots observations have a long history. Increasing and decreasing sunspot counts can be derived from the recordings with an approximately 11-year cycle. The solar cycle can vary from a minimum 8-year cycle to a maximum of 14 years between two maxima. At the moment it is assumed to be in the decreasing part of cycle 24, which maxima was in the year 2014/2015. Compared to the past cycles, the amplitude and duration were similar to cycle 14 and 16. An overview of the numbered solar cycles (smoothed values) from the year 1900 up to now is displayed in Figure 2-1. It shows that the maxima of sunspot counts for each cycle differs on the observation time. The maxima of sunspots for the last decades was during cycle 19 around the year 1960 with a count of 285; conversely for the lower sunspot cycle, the amount was between 100 to 150. [2]

2.1.2 Solar Wind

Sunspots mean a high solar activity. During this period, CME of the sun are spread out into space, which is the origin of solar winds. The high energetic plasma cloud can reach velocities of 400 km/s up to 1000 km/s, so they can reach the Earth within 21 hours. When the solar wind hits the geomagnetic field, this will cause field fluctuations and therefore geomagnetic disturbances. [2]

The intensity of a GMD event can be described by different geomagnetic indices, which are described in subchapter 3.1.2. To identify stronger geomagnetic storm activities, the daily A_p index is chosen with values higher than 150 and added in Figure 2-1. From the combined plot of the solar cycle and the geomagnetic activity can be obtained, that especially in the decreasing part of a cycle, very strong solar storms can occur. Select the Hydro-Québec and Malmö transmission system blackout caused by GIC and mark them in the figure, it can be seen that for those events, the A_p index was 246 and 204 respectively.

Although there was a well-accepted statistical link between solar flares and geomagnetic storms [3], an acceptable evidence for the correlation between them is only given since space plasma measurements and coronagraph images are used. [4]

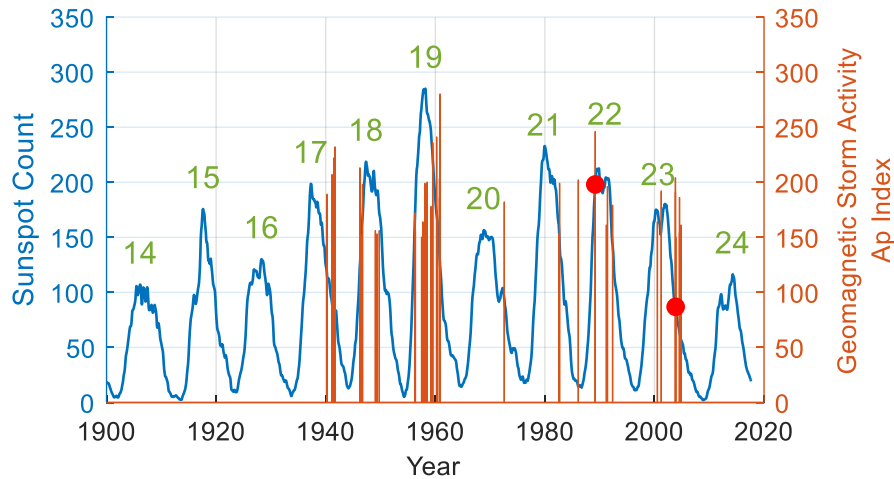


Figure 2-1 Sunspot cycles (blue) and stronger geomagnetic storm activities (orange) since 1939. The number of the cycles are plotted in green and the red dots mark the Hydro-Québec and Malmö power system blackout in 1989 and 2003. Data from [5], [6].

2.1.3 Earth's Magnetosphere

The source of the magnetosphere is characterised by two primary fields. The fluid flow of the Earth's core generates the internal magnetic field, which can be approximated as a dipole with magnetic north in the southern hemisphere and magnetic south close to the North Pole. The second part originates from external sources of continuous solar winds from the sun. [5] The ionised plasma clouds interact with the magnetic field as if they are frozen together, which forms for example the interplanetary magnetic field (IMF). Continue the approximation of frozen plasma to magnetic field, not only the solar wind plasma is fixed to the IMF, the Earth's plasma with the Earth's magnetic field too, so they cannot be mixed. Thus, the simplified assumption means, the solar plasma causes compression of the Earth's magnetic field on the dayside, and stretches the field lines on the darkside to an open magnetic tail. The magnetopause is the boundary, where the pressure of the solar wind equals the planetary field with a distance of approximately tenfold the Earth's radius on the upstream side. Outside the magnetopause, called the magnetosheath, the plasma flow is slowed down due to the impingement of solar wind and Earth's field, which additionally compresses and heats the plasma and results in swirl plasma. Inside the magnetopause, the magnetic field and ionospheric plasma rotates with the Earth. The intensities of the external fields are less than the internal [2], but experienced higher fluctuations [5] in case of alternating solar wind activities. An illustration of the fields is given in Figure 2-2 on the left side. [4]

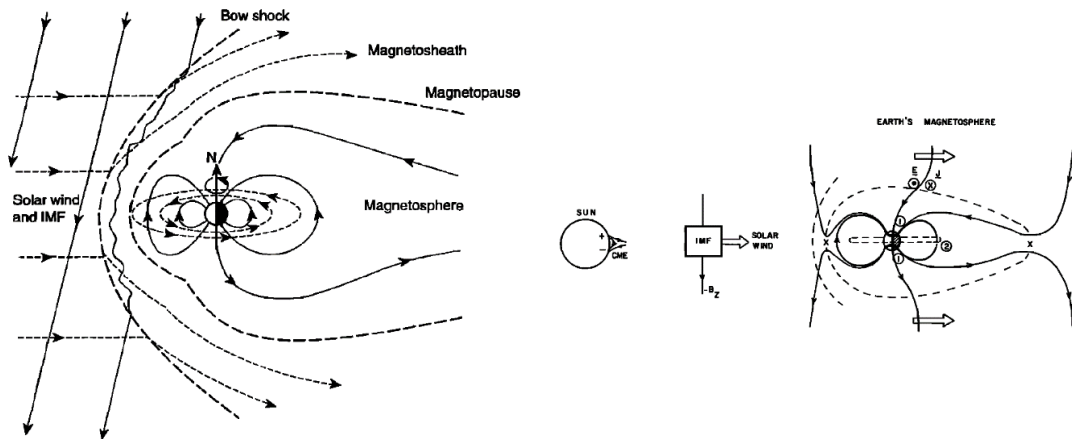


Figure 2-2 Structure of the Earth's magnetosphere and interplanetary magnetic field on the left. Due to the frozen plasma and magnetic fields, the Earth's magnetic field is compressed by solar wind on dayside and stretched on darkside (left picture). The right plot illustrates the open magnetosphere and reconnection process. Pictures taken from [4].

When high currents are present in the solar plasma or the magnetic field of the solar wind shows downwards to the south (geographical) by simultaneous the magnetospheric field goes northward, the frozen approximation will break down leading to merge the interplanetary with the planetary magnetic fields through the magnetopause boundary shown in Figure 2-2 on the right side. The process is called the magnetic reconnection. During this process, the plasma in the boundary is accelerated and formed open tubes (open magnetic flux) to the poles, where the solar wind plasma can enter the Earth's magnetosphere. It is assumed that a maximum of 20% of the interplanetary flux diffuses into the magnetosphere, the rest will be deflected. The open tubes drift in the magnetosheath downstream to the magnetic tail, where they may close again by reconnection. The closing field in the tail contracts back to the Earth and finally the cycle starts again. Beyond that, the plasma inside the closing field is compressed and accelerated to the nightside of the Earth too. The energized particles enter deep into the magnetosphere and augment the two main currents (electrojets) flowing in the ionosphere at 100 km to 150 km altitude at the auroral zone in the order of million amperes. The ring current is an equatorial flow of ions and electrons with an electrical flow from east to west (clockwise flow viewed from the Earth's north pole) in the inner Van Allen belt at distances between 3 to 5 Earth's radii. The magnetic field of the ring current counteracts the (inner) Earth's magnetic field on ground. An increase of the ring current from drifting particles causes a decrease of the magnetic field on Earth and can be measured at magnetic observatories. Therefore the disturbance storm time index (definition quotes later in subchapter 3.1.2.5) characterises the changes in the horizontal magnetic and indicates the impact of the geomagnetic storm. [4]

Local connections between the interplanetary and terrestrial magnetic fields can also occur at poles, where the parallel fields are close to each other [2]. The northern lights (aurora borealis) and southern lights (aurora australis) at the pole regions are results of the local field connections, where particles of the solar wind flow down towards the pole and ionise the atoms and molecules in the upper atmosphere. Recombination effects to the prior energy level involve release energy by visible light. [4]

2.1.4 World Magnetic Field

The magnetic field direction is from the magnetic north to the south. Actually, the magnetic north pole is in the southern hemisphere, and the magnetic south is located at higher north geographic latitudes. The magnetic poles (dip poles) are areas, where the inclination of the magnetic field equals 90° . Declination describes the angle between the horizontal magnetic field component (B_H) and the geographic north. The structure of the geomagnetic field is complex and difficult to model. Therefore, the geomagnetic field can be seen for simplicity as a dipole that also defines the geomagnetic coordinate system. The hypothetical axis through the geomagnetic dipole (dipole poles) differs from the Earth's rotational axis by about 10° [2] in the year 2015. Because the magnetic field changes over time, geomagnetic poles are also constantly wandering. [2]

The basic geomagnetic field components / indices are

- B_x – northward component
- B_y – eastward component
- B_z – vertically downward component
- B_H – horizontal field intensity
- B_F – total field intensity
- geomagnetic inclination (I)
- geomagnetic declination (D)

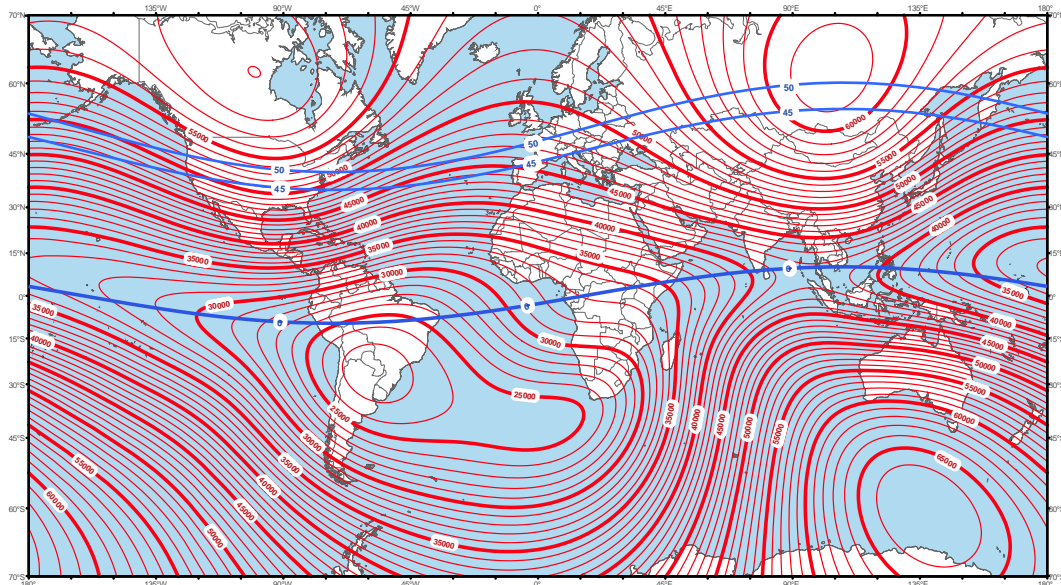


Figure 2-3 World magnetic main field (WMM) total intensity B_F (red) for the year 2015. The magnetic latitudes (blue) for the equator 0° and for Central Europe in the year 2010. Picture adapted from [6].

Observatories all over the world measure the geomagnetic field and bring together the recordings to a world magnetic field map. Calculations of the field component based on the World Magnetic Model (WMM) or the International Geomagnetic Reference Field (IGRF), both are accepted in geophysics for modelling. Figure 2-3 displays the worldwide contours of the magnetic main field total intensity based on WMM in the year 2015. It shows an occurrence of two areas in the northern hemisphere (Canada and Russia) with high magnetic field intensity B_F , compared to the southern hemisphere with one region (close to Antarctica). Beyond that, the geomagnetic latitude of the dipole is displayed in blue in Figure 2-3. The magnetic equator indicates zero degrees, and for Central Europe, the geomagnetic latitudes are between 45° and 50° N. From the picture can

be deduced, that locations with the same geographic latitude experienced different magnetic field strengths. That results from the drift between the geomagnetic dipole and the geographic north.

Table 2-1 lists the geomagnetic field components from the WMM model for specific locations derived by the historical GIC impacts. It can be seen from the table, that the towns experienced different field strength by the magnetic components. Generally can be said, that the northward field component is higher than the eastward. The geomagnetic and geographic coordinates of the locations are quoted too. Considering Vienna and Québec with approximately the same geographic latitudes, the geomagnetic latitudes have a greater difference. This is also reflected by the total field component B_F .

Table 2-1 WMM geomagnetic field components of selected towns for the 15 July 2018. Additionally quoted are the geomagnetic and geographic latitudes (lat) and longitudes (lon). Source [6], [7].

	B_x in nT	B_y in nT	B_z in nT	B_H in nT	B_F in nT	<i>Geomagnetic</i>		<i>Geographic</i>	
						lat in deg	lon in deg	lat in deg	lon in deg
Vienna	20 851	1 560	43 981	20 909	48 699	47.3 N	99.7 E	48.2 N	16.3 E
Québec	17 343	-4 923	50 767	18 029	53 873	56.1 N	2.1 E	46.8 N	71.3 W
Malmö	17 110	1 177	47 322	17 150	50 334	54.9 N	99.7 W	55.6 N	13.0 E
Cape Town	9 423	-4 468	-23 203	10 429	25 439	33.5 S	85.1 E	34.0 S	18.5 E

2.2 Ground Effects of Space Weather

The interaction between the Earth's magnetosphere and the solar wind can be determined by the geoeffectiveness. As described in the previous chapter, the energised particles of the solar wind disturb the geomagnetic field, especially with a southward field of the IMF. The time varying changes of the geomagnetic field, caused by electric currents in the ionosphere and magnetosphere, induce currents in the conductive subsurface Earth area, described by Faraday's induction law. The law implies that any magnetic variation is linked to an electric field. The driving electromotive force (*emf*) for the earth currents is called the geoelectric field [8], which amplitude is higher if the time derivation of the magnetic source increases or the conductivity of the Earth decreases. This is one reason why countries close to the magnetic poles experience higher geoelectric fields. [9]

Any man-made network system with spatial distribution and ground connection, for instance power transmission systems, offers a higher conductivity path for earth currents flow [10] compared to the earth. These currents, which originate from GMD events and enter the human infrastructure, are generally defined as geomagnetically induced currents. GIC are not only phenomena in the power grid, they can occur on railways, gas or oil pipelines [11], telecommunication cables [12, p. 4] or any other technological network system with connection to the ground and longer geographical distances [13].

The frequency of the GIC ranges from 1 Hz to 0.01 mHz. Field variations below this range are expected to generate no GIC and for frequencies higher than 1 Hz, it is assumed that the inductance of the power network will decrease the GIC [14]. Compared to the operational frequency in power transmission systems of 50 Hz or 60 Hz (Northern America), the GIC can be seen as quasi DC. Due to the very low frequency it is sufficient that the network model where the GIC flows is purely resistive.

An overview of GIC flow represents Figure 2-4. It shows the geoelectric field as driving GIC source. On the left and right side of the power transmission system, the transformers are directly grounded to earth, and in combination with the overhead lines, the transmission system offers an alternative, high conductance path for GIC flow.

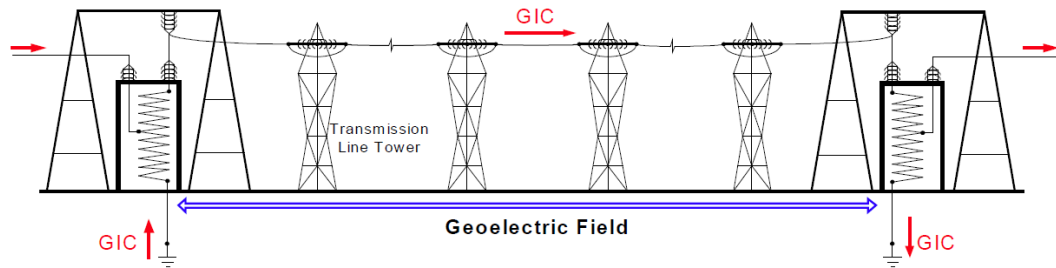


Figure 2-4 GIC flow through the power grid with the geoelectric field as driving source. Picture taken from [15].

Summarising the most relevant parameters of GIC hazard to man-made network technology as follows

- geomagnetic latitude
- geological structure and earth conductivity (for instance coastline)
- network topology and meshing degree (for instance long distances between two grounding points)

Especially for the power grid, additionally aspects like

- transformer type (for instance core design)
- voltage level (for instance 400 kV, 230 kV, 110 kV)
- transformer and network utilisation
- unusual switching state

are relevant to the geomagnetic disturbance impact and GIC consequences.

2.3 Historical Impacts of Space Weather

Several space weather disturbances on human technologies are documented in the literature. In this context, certain notable events in the past are quoted, which report in detail the dramatic consequences of a solar storm on earth and the impact of the GICs.

Carrington event. The greatest recorded space weather event in history was the “Carrington” event, lasting from 1. – 2. September 1859. While observing the sun, Carrington and Hodgson recognised independently from each other, an intensive bright light and their magnetometers on Earth being nearly simultaneous disturbed. [16], [17] About 17 h later, the tremendous coronal mass ejection hit the Earth’s magnetic field that led to the heaviest known solar storm ever. It is assumed that the geomagnetic disturbance (GMD), which can be denoted as disturbance storm time index (Dst), was about $-1600 \text{ nT} \pm 10 \text{ nT}$ [18] at the peak of the occurrence. [18]–[20]

Documentations at that time pointed out, that troubles in the telegraph systems all over the world, especially in Northern America and Europe, occurred, which even resulted in many fire sites in the case of high GIC that entered the system [21]. Another remarkable phenomenon was the appearance of auroras in both hemispheres of Earth, where they have never been expected. During the Carrington event, the auroras were visible in northern and southern latitudes within 23° of the

geomagnetic equator, which meant that they could be seen for example in Hawaii, Cuba or Jamaica [22], whereas normally the polar lights are visible at regions close to the magnetic poles.

Hydro-Québec blackout. Enormous CME occurred on the sun between 06. – 12. March 1989. Especially the eruption on 10th of March led to a solar storm that arrived in about three days the geomagnetic field and created rapid geomagnetic field fluctuations. On those days, the *Dst* peak value was about -589 nT¹ and the rate of change of the northward geomagnetic field reached values of about 1000 nT [23] within several minutes. [23], [24]

First voltage disturbances were recognised on the Hydro-Québec transmission grid on 13 March 1989 at 06:00 UT. The voltage instabilities had been noticed previously and after performing countermeasures, the high-voltage transmission system conditions were restored. But at 07:45 UT on the same day, an abrupt geomagnetic variation occurred which led to high GIC. The static compensators in the power network tripped after reaching the threshold for over-current or over-voltage. Initially two compensator outages occurred nearly simultaneously. Within one minute, several compensators and lines subsequently disconnected from the transmission grid, which caused a separation of the so-called La Grande system from the Hydro-Québec network. Isolating the La Grande network from the rest meant a loss of generation in the transmission grid of approximately 9400 MW. Due to this, the frequency decreased significantly and the automated load shedding detection could not compensate the difference. This resulted in a total blackout of the Hydro-Québec transmission network and in addition, a shut down of the nuclear power facility of Gentilly-2. It took about 9 h to restore 83 % of the full power supply in that region and the total amount of cost is estimated to have been 13.2 million USD. [23], [24]

Malmö blackout. The last intense space weather event in the recent history occurred from 19. October to 07. November 2003. During these period more than 250 solar energetic events were recorded; three especially immense solar eruptions on the sun emerged between 29. and 31. October 2003, which are also referred to in the literature as the “Halloween Storm”. The massive and intensive coronal mass ejection from the sun hit the Earth’s magnetic field and caused extensive geomagnetic disturbances which led to a maximum horizontal magnetic field derivation of $|dH/dt = 389.6 \text{ nT/min}^2$ and a maximum *Dst* of -422 nT³. [26], [27]

Flights at higher latitudes are rerouted to avoid the risk of higher exposure to particle radiation and the possibility of communication failure. Changing the flight route to an alternative means increasing travel time and costs between 10 000 USD up to 100 000 USD per flight. In general, satellites have been impacted by solar activity, and therefore it is assumed that the loss of the Japanese ADEOS-2 spacecraft with a value of 640 million USD was due to the solar storm of 2003. [26]

Additionally, the consequences of the solar storms to technological infrastructure on Earth were so immense, which caused an outage of the power transmission system in southern Sweden on 30. October 2003 at 20:07 UT. The blackout concerned 50 000 customers in the Malmö region without electricity for about one hour. Moreover, people had to be rescued out of elevators, the fire brigade marched out to several fire alarms and trains were delayed. According to the Malmö power transmission outage, the estimation of the total economic loss amounted to 500,000 USD. [27]

Investigations of the transmission system outage in Sweden revealed that the source of the blackout was a combination of the harmonics, due to GIC, and an unusual switching state of the power network system. Cables were added to the subsystem, which means higher phase-to-earth capacitances and therefore a higher sensitivity to voltage harmonic distortion. The relay was not

¹ Data from the World Data Center (WDC) for Geomagnetism, Kyoto, Japan. [7]

² Data from the Brorfelde observatory in Denmark. [25]

³ Data from the World Data Center (WDC) for Geomagnetism, Kyoto, Japan. [7]

designed for the unusual high 150 Hz currents and tripped which led to the Malmö system blackout. The computed GIC reveals transmission line currents up to 230 A per phase. [27]

Southern Africa. Triggered by the same solar storm event (“Halloween Storm”) from October to November 2003, there was an unusual chronology of transformer outages in South Africa. Starting on 17. November 2003, the first transformer at Lethabo tripped on protection, followed on 23. November 2003 with a similar transformer tripping at Matimba. In the year 2004, another four transformer outages were reported from the grid operator in total. All failed transformers were inspected and it has been revealed, that the reason was thermal damage. This correlates with increased dissolved gasses in the transformer. The affected transformers are checked regularly about dissolved gasses and an unusual rapidly increase of the gasses were recognised after the solar event in 2003. The investigations show a high relation between the occurred GIC, the measured dissolved gasses and the transformer failures. Although the GIC levels in mid-latitude regions were expected to be low, the design of the transformers appears to be susceptible to GIC. [28]

Further GIC events on power grid. Since knowing about the storm weather events in the past and the possible destructive impacts on human technology, power network operators in different countries have considered the GIC phenomena more in their risk assessment. The study of [29] listed previously reported problems in the power network grid in the period from 1989 up to 2006, which are associated with geomagnetic disturbances. Table 2-1 listed some of the events from [29]. The report reaches from abnormal noise of the transformer or heavy buzz sounds up to measured transformer neutral currents, tripping of capacitor banks and voltage swings, which all coincide with high geomagnetic disturbances.

Table 2-2 Selection of previous power network problems adopted from [29].

Date	Time UT	Location	Country	Description
13.03.1989	22:19	Willmar	USA	Voltage swings
13.03.1989	07:43	Nemiskau	Canada	Shutdown of static compensators, static var compensator damaged
24.03.1991	03:43	Pleasant Valley	USA	GIC observed greater than 66 A
24.03.1991	21:34	Rauma	Finland	200 A for 1 min
06.11.2001	01:52	Dunedin	New Zealand	Transformer tripped, damage to insulation
09.11.2004	18:49	Ling'ao	China	55.8 A

Phone cables. On 4th August 1972, a hugely enhanced solar wind compressed the magnetosphere and caused the outage of the coaxial cable system in Iowa, United States. The shutdown of the 250 km long cable section was triggered by higher current amplitudes detection of both converters at the end of the line. Usually, the impact of solar activity causes high fluctuations of the geomagnetic field and therefore geomagnetic disturbances. Uniquely in this event, the disturbances were not primarily from field fluctuations, but resulted even more from the distortion of the magnetosphere. During this solar event, the boundary of the magnetosphere on the sun side was decreased from approximately 10 to 4 earth radii. [12]

2.4 GIC Effects on Power Transformers and Human Infrastructure

Power transformers are essential in modern AC voltage transmission systems. To minimise the transportation loss between far distances of energy producers and consumers, it is advantageous to transform the energy from low-voltage to the high-voltage level. Therefore, the energy from the power generator is transformed to the medium-, high- or extra-high-voltage level of transmission and distribution systems and transformed back again to the medium- or low-voltage level of customers and consumers. The different voltage levels are classified in four main categories as stated below.

- extra-high-voltage or transmission level with line voltages from 230 kV, 400 kV up to 750 kV
- high-voltage or subtransmission level with line voltage of 110 kV
- medium-voltage or distribution level with line voltages between 6 kV to 30 kV
- low-voltage level with line voltages from 0.4 kV up to 1 kV.

Each of the voltage levels are coupled with a transformer, and therefore the transformer can be divided into various usages, for instance generator step-up for linking the substation with the transmission network with unit ratings up to 1 300 MVA (3-phases) or 700 MVA (1-phase), system-interconnecting transformer (network transformer) with nearly the same unit rating or distribution transformers. [30]

2.4.1 General on Transformers

2.4.1.1 Magnetic Field and Magnetic Circuit

The material property for the magnetic field is denoted by the relative permeability μ_r . Together with the magnetic permeability of the vacuum μ_0 , the relation between the magnetic field \mathbf{B} and the magnetic field strength \mathbf{H} is denoted in equation (2-1) as follows. (In general for this section, field vectors are marked in bold.)

$$\mathbf{B} = \mu_r \mu_0 \cdot \mathbf{H} = \mu \mathbf{H} \quad (2-1)$$

\mathbf{B}	magnetic field, $[T = \frac{Vs}{m^2}]$
\mathbf{H}	magnetic field strength, $[\frac{A}{m}]$
μ	magnetic permeability, $[\frac{Vs}{Am}]$
μ_r	relative magnetic permeability
μ_0	magnetic permeability of the free-space, $\mu_0 = 4\pi 10^{-7} \frac{Vs}{Am}$

Integrate the magnetic field strength \mathbf{H} along a closed loop c with segments \mathbf{l} and considering the number of turns N_T (for example turns of a winding on a transformer limb), this is obtained in equation (2-2) by Ampere's law, which also describes the electric current density \mathbf{J} through a cross-section $\mathbf{\Gamma}$. The law is generally valid for homogeneous and inhomogeneous fields.

$$\Theta = \oint_{\partial\Gamma} \mathbf{H} \cdot d\mathbf{s} = \sum_c I = N_T \cdot I = \int_{\Gamma} \mathbf{J} \cdot d\mathbf{\Gamma} \quad (2-2)$$

Θ	magnetomotive force, [A]
I	electric current, [A]
N_T	number of turns
\mathbf{J}	electric current density, $[\frac{A}{m^2}]$

The magnetic flux Φ is defined in equation (2-3) by the integration of the magnetic field \mathbf{B} through a given cross-section Γ . Therefore, the magnetic field \mathbf{B} can be interpreted as the magnetic flux density.

$$\Phi = \int_{\Gamma} \mathbf{B} \cdot d\mathbf{\Gamma} \quad (2-3)$$

Φ magnetic flux, [Wb = Vs]

To conclude with the most relevant formulations to describe the magnetic circuit, Faraday's law of induction is obtained in equation (2-4) with the electromotive force U_{emf} .

$$U_{emf} = -N_T \frac{d\Phi}{dt} \quad (2-4)$$

U_{emf} electromotive force, [V]

Inspired by Ohm's law for electric circuits, the same can be applied to the magnetic circuits given in formulas (2-5) and (2-6).

$$\Phi = BA = \mu HA = \mu \frac{N_T I}{l} A = \mu \frac{A}{l} \Theta = \frac{1}{R_m} \Theta = \Lambda \Theta \quad (2-5)$$

$$\Theta = R_m \cdot \Phi \quad (2-6)$$

A cross-section, [m^2]
 l path length, [m]
 R_m reluctance, [$\frac{A}{Vs}$]
 Λ permeance, [$\frac{Vs}{A}$]

Duality between electric and magnetic circuits. The equivalent circuit between electric and magnetic is given in [31]. With the formulated duality, the frequency independent interlink between the magnetic reluctance and the electric inductivity can be calculated. Assuming an ideal (without stray flux) transformer with two windings – meaning the sum of magnetic fluxes and induced voltages are zero and moreover the magnetomotive forces are equal - following transformation link (2-7) can be given

$$\begin{aligned} u &\leftrightarrow \frac{d\Phi}{dt} \\ i &\leftrightarrow \Theta \end{aligned} \quad (2-7)$$

leading to expressions (2-8) and (2-9) for primary and secondary side.

$$u_1 : u_2 = j\omega\Phi_1 : j\omega\Phi_2 \quad (2-8)$$

$$i_1 : i_2 = \Theta_1 : \Theta_2 \quad (2-9)$$

Dividing both upper equations obtained to formula (2-10)

$$\frac{u_1}{i_1} : \frac{u_2}{i_2} = \frac{j\omega\Phi_1}{\Theta_1} : \frac{j\omega\Phi_2}{\Theta_2} \quad (2-10)$$

Require an inductive electrical element, the left side of equation (2-10) can be modified to the below expression (2-11)

$$j\omega L_1 : j\omega L_2 = \frac{j\omega\Phi_1}{\Theta_1} : \frac{j\omega\Phi_2}{\Theta_2} \quad (2-11)$$

L inductance, $\left[\frac{Vs}{A} = H\right]$

and applying (2-6) to (2-11), the frequency independent duality can be stated like formula (2-12)

$$L_1 : L_2 = \frac{\Phi_1}{\Theta_1} : \frac{\Phi_2}{\Theta_2} = \frac{1}{R_{m1}} = \frac{1}{R_{m2}} \quad (2-12)$$

Taking considerations of the number of turns N_T , equation (2-12) and the general formulation of the inductance for a conductor loop $N_T \cdot \Phi = L \cdot i$ obtain to the general relation (2-13).

$$R_{m_n} = \frac{\Theta_n}{\Phi_n} = \frac{N_T \cdot i_n}{L_n \cdot i_n} = \frac{N_T^2}{L_n} \quad (2-13)$$

2.4.1.2 Principle of Transformers

The functionality of a transformer is briefly outlined for a simple single-phase two-winding transformer. Basically the transformer consists of a magnetic circuit with an iron core (ferromagnetic material, high magnetic permeability) and a minimum of two electrically isolated windings (primary and secondary winding). The iron core provides the flow of the time-varying magnetic flux Φ and therefore the magnetic coupling between the two windings. The magnetic flux is driven by the magnetising current I_m . From the time-varying voltage source \underline{U}_1 , the current \underline{I}_1 generates a flux in the primary winding and the alternating flux Φ induces a voltage \underline{U}_2 in the secondary winding. The magnetic circuit is illustrated in Figure 2-5. [30]

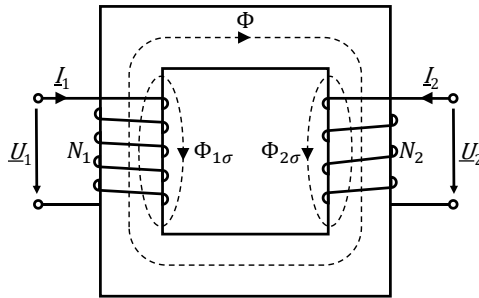


Figure 2-5 Principal construction of a single-phase two-winding transformer.

For a realistic transformer, leakage fluxes exist for both windings $\Phi_{1\sigma}$ and $\Phi_{2\sigma}$ respectively, which close in the air or in the mantle of the transformer and represents transformation losses. Hysteresis losses from constantly magnetic dipole-orientation changing can be minimised by utilising soft-magnetic materials for the iron core. Additionally, losses in the magnetic circuit occur from eddy currents of the flux. This is reduced by using thin, isolated iron sheets. Both, the eddy currents and hysteresis losses are summarised to iron losses or no-load losses and are independent on the load current, but are dependent on the voltage by $P_{Fe} \sim B^2 \sim U^2$ [32]. Considerations of the winding copper loss P_{Cu} finalize the equivalent circuit of the transformer shown in Figure 2-6. The superscript ' refers quantities from the secondary to the primary side of the transformer converted by the well-known turns ratio $t. r.$ for ideal transformers. Normally, the primary winding is the high-voltage (HV) side and the secondary winding the low-voltage (LV) side; otherwise the ratio will turn. [30]

$$t. r. = \frac{N_1}{N_2} \tag{2-14}$$

$t. r.$ turns ratio
 N_1, N_2 primary and secondary nominal number of turns

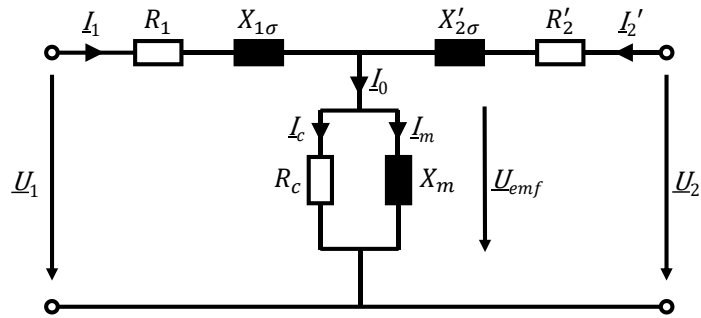


Figure 2-6 Equivalent circuit of the transformer.

$\underline{U}_1, \underline{U}'_2$ primary and secondary voltages, [V]
 \underline{U}_{emf} electromotive force, [V]
 $\underline{I}_1, \underline{I}'_2$ primary and secondary currents, [A]
 \underline{I}_0 no-load current, [A]
 \underline{I}_c core-loss current, [A]
 \underline{I}_m magnetising current, [A]
 R_1, R'_2 primary and secondary winding resistances, [Ω]
 R_c core-loss resistance, [Ω]
 X_1, X'_2 primary and secondary winding leakage reactances, [Ω]
 X_m magnetising reactance, [Ω]

2.4.1.3 Types of Transformers

Important for the susceptibility of the transformer to the saturation effects caused by GIC is the configuration between the winding and core of a transformer. The transformer can be classified into two principal types, as shown in Figure 2-7.

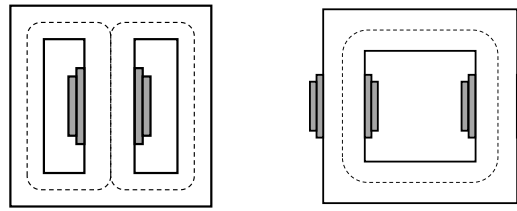


Figure 2-7 Basic single-phase transformer types with the shell-type on the left and core-type on the right side.

The shell-type transformer on the left in Figure 2-7 is characterised by one wound limb (both voltage levels) in the middle and two unwound limbs which offer, coupled with the yoke, the magnetic flux-returning path and providing a better magnetic shielding. Because of the two returning paths for each phase, the magnetic flux splits at the yokes with half returning path on both sides and therefore reducing the design high. Core type transformers on the right in Figure 2-7 are more common in the power industry. In contrast to the shell-type, each limb of the core-type transformer covers half of the high and low voltage level windings. [33]

For the three-phase power network system, the single-phase units can also be combined with a three-phase transformer bank. This is (mostly) due to the fact of reducing transformer dimensions and weight for the purpose of transportation. Other reasons such as the handling of substitution units in the event of failures also justify the higher initial cost of transformer banks.

With the considerable economic advantage of lower production cost, a three-phase transformer is preferred instead of three single-phase units. Figure 2-8 illustrates the various transformer types. One difference to the two three-phase core-types is the existence of a separate flux-return path. Generally, the core fluxes have, as well as the phase voltages, a phase difference of 120° and therefore cancel to zero. For the 5-limb core-type, the two unwound limbs offer an alternative return path for the magnetic flux and reduce the yokes depths. [33]

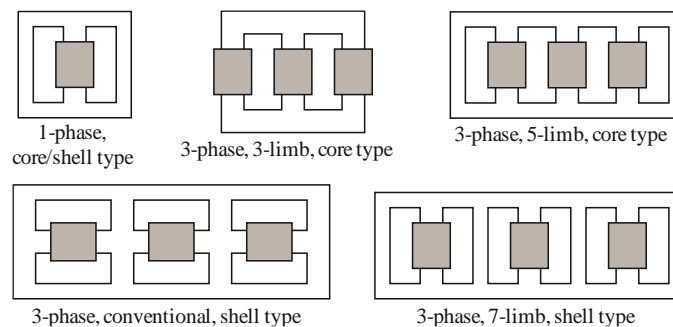


Figure 2-8 Different types of transformer for the three-phase system. The single-phase type is connected to a three-phase transformer bank.

Autotransformer. The exception for an autotransformer compared to the other transformers is that the autotransformer has a section of common HV and LV winding. This means that there is not only a magnetic but also an electric connection between the windings. The galvanic connection between the interconnected systems has the disadvantage of the missing isolation between the primary and secondary winding.

But the most benefit of the autotransformer is due to the common winding and therefore economic advantage compared to other transformers with the same rated power. If the primary and secondary voltages show no great differences, than the current difference, which flows through the common winding, is small too and therefore a lower cost of material. On this property, the

application fields are mostly for compensating voltage fluctuations or coupling of high- and extra-high-voltage levels [32]. The vector group of three-phase autotransformers are restricted to star-star winding connection with a common neutral point. A directly grounded neutral point means therefore, that both voltage levels are grounded. [33]

2.4.1.4 Vector Group

Next, considerations of the connections between the windings of a three-phase system are outlined in Figure 2-9. Basically they can be summarised to three different forms which define the transformers vector group. The most common ones are star ↔ y and delta ↔ d connection, but also an interconnected star ↔ z connection is possible by subdividing the transformer windings into halves. The vector group of the high (primary) voltage is capitalised, those of the low (secondary) voltage is uncapitalised. Combinations between the various vector groups have consequences on for example neutral point treatment of the transformer, turn ratio, phase shifting between high- and low-voltage, or transmission of harmonics. An additional letter N or n indicates, whether the star point of a y- or z-connection is available. Besides the identification letters, an index *k* describes the multiple of 30° that the low voltage is delayed to the high voltage vector, which has to be equal for parallel operation of transformers. According to the vector group, the voltage turn ratio will be changed by a factor of 1, $\sqrt{3}$ or $1/\sqrt{3}$. [30]

Various aspects such as operation conditions, neutral point treatment, etc. can determine which vector group is used for a transformer. Star connection is to preferred for high- and extra-high-voltages because the isolation of the windings can thus be reduced by a factor of $\sqrt{3}$. Another characteristic of a star connection is that the residual current cannot be transformed to the other voltage side: however, for a delta connection, the residual currents can flow in the windings and therefore be transformed to the other voltage level. A direct-grounded neutral point is very common in high-, extra-high- and low-voltage systems using the benefit of minimal voltage increase in the faultless phases in terms of single-phase faults. [30]

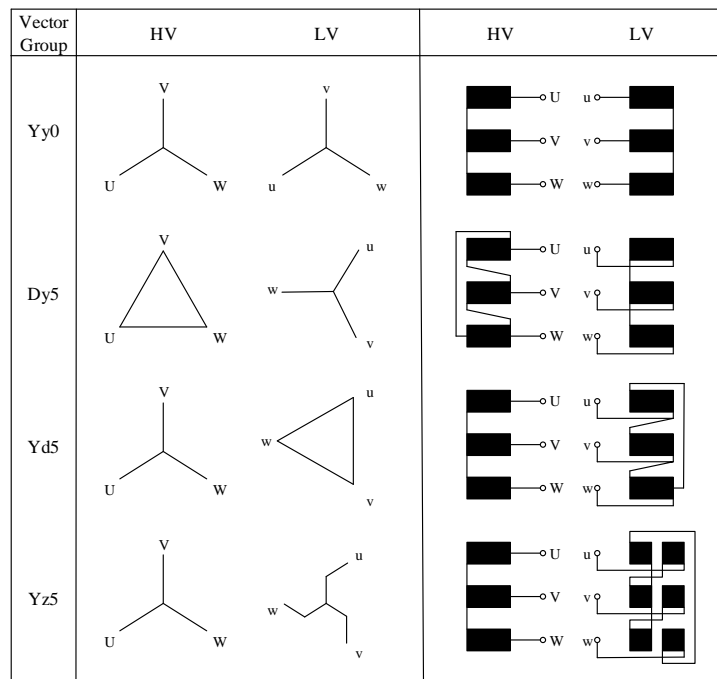


Figure 2-9 Common vector group of transformers.

2.4.1.5 Magnetisation Characteristic and Half-Cycle Saturation

Ferromagnetic materials are essential in modern technologies such as for the magnetic circuit of transformers. The property of the ferromagnetism is the existing magnetic domains⁴ in the material. The magnetic domains are small regions where the atomic magnetic fields are oriented in the same direction, but differ for each region. An outside magnetic field causes an orientation of the magnetic domains in the same direction, and the aligned regions expand to neighbouring areas with the other direction. This will increase the magnetic flux significantly. According to the external magnetic field, the orientation of the magnetic domains will be strong or weak. If all magnetic domains are oriented by the external field, a further increase causes saturation effects, which occur for iron between $B = 1.5 \dots 1.7 \text{ T}$, and result in nonlinearity between the magnetic flux Φ and magnetising current I_m [32]. [34]

Especially in power energy technology, it is important to minimise the losses of the magnetic circuit magnetisation. Therefore, ferromagnetic materials with high permeability μ_r are used with characteristically soft magnetic materials for low magnetic coercivity H_c and remanence B_r . Both indicate a small hysteresis and therefore reduce magnetic loss. For simplicity the hysteresis can be drawn by their middle pathway, which indicates the magnetisation characteristic, with the proportionality of $B \sim \Phi$ and $H \sim \theta, I$, as illustrated in Figure 2-10. Plotted on the ordinate is the magnetic flux Φ and on the abscissa the magnetising current I_m . The magnetisation characteristic has two sections: one is the linear range from zero to the knee point and the other is called the saturated range. The crossover between the two curves defines the knee point. [34]

Normal conditions of transformer operation are shown in the left-hand picture in Figure 2-10. Therefore, the AC magnetic flux operates only in the linear range of the magnetisation characteristic, where the maxima peak values are close to the knee point and do not overtop the knee point at any time. Following the amplitude of the flux to the linear magnetisation characteristic, the magnetising current can be reproduced on the ordinate. Because of the sharp rise behaviour of the curve in the linear range, which indicate by soft magnetic materials with high permeability, the magnetising current is small compared to the load current. The exciting current is about 0.5 % of the rated load current if unsaturated [35].

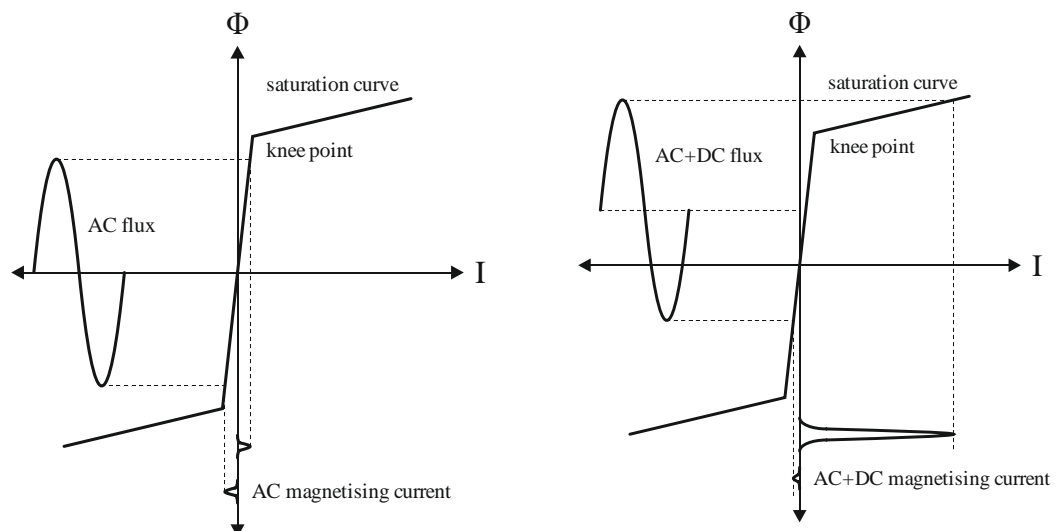


Figure 2-10 Simplified magnetisation characteristic. The left picture corresponds to normal operation with only the AC flux in the linear range, and the right one demonstrate positive half-cycle saturation by AC+DC flux.

⁴ Pierre-Ernest Weiss

Half-cycle Saturation

An occurrence of an additional DC component on the transformer windings caused a superimposed AC+DC flux density in the magnetic core. If the peak of the flux exceeds the knee point of the magnetisation characteristic for any part of the cycle (positive or negative), the core is saturated. This is known as half-cycle saturation, because the DC flux component offsets the AC flux either in the positive or negative way, and only the amplitude of one half-cycle saturates the core. When saturated, the magnetic core provides a higher reluctance to the magnetomotive force and therefore a smaller increase of the magnetic flux. In accordance with that, the magnetising current significantly increased like a pulse with high amplitude. The magnetising current pulse consists of DC, fundamental and harmonic components [36]. If the induced DC voltage divided by the DC reluctance path equals the magnetising current, the increase of DC flux density stops to a steady state. [15]. Due to the higher magnetising current, the reactive power consumption rises rapidly. [37].

The half-cycle saturation will be illustrated on the right picture in Figure 2-10. The AC magnetic flux has an additional positive DC component and the total magnetic flux will therefore be postponed. Due to the offset, a part of the positive half-cycle of the magnetic flux overtops the knee point into the saturation area. Following again the peak amplitude of the magnetic flux to the magnetisation characteristic and draw the magnetising current, hence resulting in higher magnitudes for positive half-cycle compared to the normal operation.

Modern transformers are designed to minimise the losses and noise. Due to that, the magnetic circuit required high magnetic permeability, which can be accomplished by grain-oriented steel usage. This iron core offers high permeance for the flux path; in consequence, small currents are sufficient for nominal flux density of the transformer. According to minor magnetisation currents, a higher saturation-susceptibility to small DC currents exist. [38]

Investigations on a large single-phase transformer with neutral DC exposure of 6 A, 12 A and 40 A shows that the respective magnitude peaks of the magnetising current are 5 %, 11 % and 47 % of the full load current [37]. Calculations on a 250 MVA single-phase core-type autotransformer regarding DC/GIC injections indicates magnetising current pulse reaches values of 16 %, 25 % and 34 % of the full load root mean square (RMS) current for a DC level in each phase of 10 A, 15 A and 20 A. Moreover, it is pointed out that the average duration of the pulse is between 1/10th to 1/12th of the cycle. [15]

2.4.1.6 DC Sensitivity of Transformer Types

The DC flux and susceptibility of transformers depends on three main components [37]:

- the magnitude of the DC,
- the number of turns of the winding where the DC flows and
- the permeance of the path for DC flux.

The various transformer types offer different magnetic reluctances for the flux path in the magnetic circuit. Generally, the shell form offers an alternative return path for the flux in the core and therefore has higher permeance and requires lower magnetisation currents to excite the transformer. Hence, small symmetric DC currents in all transformer phases have a large influence on the DC flux. In contrast, for example a three-phase three-leg core transformer is relatively insensitive to DC offset because of the higher DC reluctance path. The DC magnetic flux path begins from one yoke, runs to the tank cover and walls, and finally closes via the other yoke; this represents a very high reluctance and low permeability [37]. [8], [38]

A simplified overview of the transformer type sensitivities to DC currents is given in Table 2-3 from [39]. The paper analysed the obtainable DC flux area outside the wound limb of the magnetic

core and defined this as the DC sensitivity of transformers. The per unit (p.u.) area for the DC flux return characterises the sensitivity, so higher p.u. values mean higher susceptibility. [8]

Table 2-3 DC sensitivity in per unit of different transformer types. Source [39].

Phases	Form	Per unit area available for DC flux return
Single-phase	Core or shell	1
Three-phase, seven-leg	Shell	0.67
Three-phase, conventional	Shell	0.5
Three-phase, five-leg	Core	0.24 – 0.33
Three-phase, three-leg	Core	0

It is believed in [8] that the type of transformer is one of the reasons, why the transmission grid in Finland has not experienced such high GIC compared to other high-latitude countries for example Sweden or Norway. Finland uses mainly a five-leg core-type transformer which tends to be not as susceptible to GIC as single-phase units.

2.4.2 Consequences of DC/GIC Saturation Effects on Transformers

2.4.2.1 Mechanical Vibration, Noise

Depending on the induction, transformer noises are results of the magnetostriction in the iron core, which causes the ferromagnetic materials changing their lengths. Due to the 50 Hz nominal field, this means double in the mechanical vibrations and noises with a frequency of 100 Hz and even multiples of the 50 Hz base frequency– even harmonics. [32]

In the presence of a further DC component in the field (or in the current), the resulting vibrations not only involve even harmonics, but in addition forces with the 50 Hz line frequency and odd multiple of the line frequency occur. This can be explained by looking at the signal characteristic of the magnetic flux and magnetising current with an additional DC component in Figure 2-10 on the right subplot. The signal characteristic is not half-wave symmetric by applying the Fourier transform on the signal it is obtained, that even and odd harmonics of the 50 Hz line frequency are present in the frequency spectrum. Due to the increase of harmonics, the mechanical vibrations increase and the sound power of the transformer rises sharply. Hence, the first evidence of DC components in the magnetic circuit can be determined by spectral analysis of the transformer noise and the presence of certain harmonics. [38]

Sound investigations on a single-phase with return limb and a three-phase three-limb transformer with rated power of 134 MVA and 100 MVA are performed in [38], [40]. It demonstrates that a small symmetrical DC current injection in the neutral point of the single-phase transformer causes a rapid rise in audible noise and no-load sound pressure level too. For the three-phase three-limb transformer, the injected current was made asymmetric. This is mainly caused by the effect of non-symmetric magnetisation of the core (half-cycle saturation) and occurrence of higher harmonics in the frequency spectrum. In case of DC injection as high as the excitation current, the measured sound pressure level increase for the single-phase transformer is about 14 dB(A) for a flux density of 1.4 T, and about 22 dB(A) for a flux density of 1.561 T for the three-phase three-limb transformer. Moreover, the investigations pointed out, that the noise level is higher for lower AC core flux.

Due to the demand for low-noise, modern power transformers design-requirements are refined. This can be achieved by the usage of core steels with high grades of magnetic orientation and low magnetostriction and/or reducing the flux density [41]. Installation of sound insulation around

transformers can be a preventive measure against noise. Due to the limited space in substations and cost-intensive construction, this case could be an exception.

2.4.2.2 Thermal Losses and Overheating

The occurrence of higher magnetisation current leads to increased leakage flux outside the core. The consequences are eddy current losses in the winding and structural parts like tank walls, tie plates, yoke clamps, etc. Hot spot temperatures can occur locally in the winding and structural steel parts of the transformer. [35], [37]

Reported by [42], a measured rapid rise in temperature from 60°C to 175°C within 10 minutes during a GIC event on a 350 MVA transformer. If the transformer exposure to GIC is long (over hours or days) and cumulative, the likelihood of transformer lifetime reduction and insulation aging rise, which may lead to transformer failure.

The work of [37] presents temperature calculations in windings and tie-plates of a single-phase core transformer. The computations consider a DC injection of 20 A, 30 A, and 50 A for each phase over 30 minutes while fully loaded. After 5 minutes, the temperature reaches approximately the final value ranging from 6°C to 12°C higher than without DC occurrence. Same calculations are performed for tie-plants resulting in temperature increase between 10°C up to 30°C within 20 minutes.

In [43], thermal investigations are performed on the tie bar of a single-phase power transformer and demonstrate possible significant heating points of structural parts. The approach of a simplified temperature model was evaluated by measurements in the axial middle and the top end of the tie bar. The DC steps from 10 A/phase up to 50 A/phase are injected in the transformer during no-load operation. Measured steady-state temperature values for the tie bars and tank oil from the paper are outlined in Table 2-4 for each DC level. Differences between measurement and simulation results revealed a 10°C maxima and the duration to reach the steady-state level was between 30 minutes to 50 minutes.

Table 2-4 Measured temperatures during DC injections in a no-load operating single-phase transformer. Source [43].

DC A/phase	Tie bar (axial centre) °C	Tie bar (top) °C	Tank oil (top) °C
0	28.0	28.0	28.0
10	73.0	59.6	29.0
20	102.5	82.4	31.0
30	114.2	95.9	35.0
40	121.3	105.4	39.0
50	126.7	109.7	40.0

Further calculations of the temperature behaviour on structural parts and windings of power transformer are given in [44]. The already cited transformer failure in section 2.3 due to overheating, is also discussed in [37]. One statement of the paper is, that some old design shell transformers are more susceptible to half-cycle saturation and therefore higher eddy currents in the windings can occur, which cause locally thermal hot spots. The old winding concept was designed for leakage fluxes under normal operations. However, newer transformer design from manufactures minimise the hazard of circulating currents in the winding. Moreover, it is mentioned that the overheating of transformers has other primary sources than the impact of GIC, because the typical signature of the GIC and short duration time is insufficient for thermal damage of winding or structural parts of the power transformers.

Hot-spot temperatures are evaluated in the IEEE guidelines [15] and temperature limits are worked out as listed in Table 2-5. The limits are recommended for the transformer specification under a specific GIC signature, to estimate the loss of life and prevent gas bubbles in the oil.

Table 2-5 Temperature limits of transformer components for GIC exposure, recommended by IEEE transformer guideline. Source [15].

Component	GIC	
	Base	Pulse
Cellulose insulation	140 °C	180 °C
Structural parts	160 °C	200 °C

2.4.2.3 Harmonics

A brief exposition of Fourier series and harmonics [45], [46] follows. Generally, each periodic function $f(t)$ can be decomposed into the sum of trigonometrical functions with fundamental frequency and integer multiples of the fundamental, described by the well-known Fourier series - equation (2-15). The first coefficient a_0 represents the DC component.

$$f(t) = \frac{a_0}{2} + \sum_{n=1}^{\infty} (a_n \cos(n \cdot \omega_1 t) + b_n \sin(n \cdot \omega_1 t)) \quad (2-15)$$

a_0	DC Fourier coefficient
a_n, b_n	Fourier coefficients, $a, b \in \mathbb{R}$
ω_1	fundamental frequency, $\omega_1 = 2\pi f_1$
n	ordinal number of the harmonic components

If the shape of the positive and negative half-wave are equal besides the sign $f(t) = -f(t + T/2)$ with T as period, the corresponding spectrum contains only odd harmonic orders. For stationary case in power engineering, voltages and currents generally accomplish the agreement. Otherwise, to reproduce the original shape, harmonics between the integer multiples are required. A classification of the harmonics is stated below.

- **Fundamental.** Rated line frequencies in power supply are 16 2/3 Hz, 50 Hz or 60 Hz.
- **Harmonics.** Integer multiples of the fundamental frequency.
- **Interharmonics.** Frequencies between the integer multiples of the fundamental frequency.
- **Subharmonics.** Frequencies below the main frequency.

The fundamental and each single harmonic in the three-phase system can be described by symmetrical components. Assuming symmetrical relations, means that the signal shape of all three phases are the same and the fundamental phase shift between them equals 120°, the distinctive is follows with k as an integer value.

- **⁰Zero sequence** with harmonic order $\nu = 3k$ ($\nu = 3, 6, 9, \dots$)
- **¹Positive sequence** with harmonic order $\nu = 3k + 1$ ($\nu = 4, 7, 10, \dots$)
- **²Negative sequence** with harmonic order $\nu = 3k - 1$ ($\nu = 5, 8, 11, \dots$)

Besides the fundamental, normally only odd harmonic exist where the magnitude of harmonics decrease with increasing order. Depending on the vector group and neutral point treatment of the transformer, the zero sequence could be transferred into other grid levels.

Non-linear characteristics of electrical utilities, like power electronics or the magnetising curve of transformers, cause currents in the system, that deviate from a pure sinus wave. Those non-sinusoidal currents produce corresponding voltage harmonics on the network impedance and therefore distort the ideal line voltage. Due to the non-linearity of the magnetising curve of ferromagnetic materials, even and odd harmonics occur during half-cycle saturation caused by the distorted transformer magnetising current. The harmonic magnitudes increase approximately linear with the DC amplitudes where both (even and odd) harmonics exist in the spectrum [36]. It is significantly for current harmonics caused by GIC that the waveform of each phase is similar in shape and therefore approximately equally distorted. [35]

It is observed in [37], that the types of transformer have different characteristics in harmonic magnitude propagation. For a three-phase three-limb transformer, the magnitudes of harmonics decrease with increasing order. Instead, the harmonic amplitudes are more uniform for single-phase transformers, meaning higher content of higher harmonics than for the three-limb transformer. [37]

2.4.2.4 *Undesired Tripping*

The main claim in protection technology is the selective, secure and fast detection of fault conditions and the disconnection of the electric equipment from the power network. Undesired tripping of protection relays is one of the greatest hazard during GMD events, which may affect power equipment like shunt capacitor banks, filter banks, static reactive power (var) compensators and transformers. One crucial criterion of the tripping is that the settings of the protection relay are not designed for the harmonic characteristic caused by transformer half-cycle saturation, which leads to false operation of protection relays. It is outlined in [47] that during half-cycle saturation, the protection relays could only handle about half of the desired current, which lead to false operation.

Another important topic in transformer protection is the correct differentiation between Inrush currents, caused by transformer switching, and fault conditions. The Inrush currents are characterised on the second order of harmonic with an abate DC component superimposed, which decrease to normal condition within the range of several seconds, depending on the size of transformers. Triggered by a threshold of the second harmonic, the protection relay of the transformer is blocked during that time. Harmonics from transformer half-cycle saturation could lead to misoperation of the protection relay.

Furthermore, the zero sequence currents can cause misoperation of neutral overcurrent relays, because of “erroneously” detection of large neutral currents. [35].

The undesired tripping of the protection relays caused by harmonics was the (common) initial point of system voltage instabilities reported previously in subchapter 2.3. If, for instance, a power generator protection relay trips, this means a loss of power generation and simultaneously the line frequency will rise and the load flow will change in the network. A change of the load flow will cause higher utilisation on other power utilities like power transformers and under adverse switching conditions, the additional burden to the power transformer will reach overloading conditions and will also disconnect from the power grid. In the worst-case, this can lead to chain reaction of protection tripping to other power utilities, which may result in a blackout.

It is recommended in [35], [37], [48], [49] to review the sensitivity of the harmonic settings of the relays. But increasing the harmonic peak values of the relays, for example during high geomagnetic disturbances, to lower harmonic sensitivity, the system protection will decrease.

2.4.2.5 Reactive Power Consumption and System Voltage Instability

The magnetising current component is in phase with the flux and therefore both lag the voltage of 90° . This behaviour is notable like a reactive load to the power system and therefore leading to a reactive power consumption. Investigations on a large single-phase power transformer point out the nearly linear relations between DC and var consumption, for example 7 % of rated MVA with 50 A/phase [50].

The additional reactive power demand causes a decrease in system voltage and therefore problems in voltage stability. This may lead in the worst case to voltage collapse, which is one of the most redoubtable and dangerous impact of strong GMD events.

First load-flow calculations are performed in the 1980s to estimate the voltage drop and reactive power flow changes in the power transmission during geomagnetic storms [51]. In the paper it is pointed out, that the real power flow can change during strong geomagnetic disturbances, especially at regions with high latitude.

2.4.3 GIC Effects on other Power Systems Utilities

Instrument transformers. Generally, the transformer principle is also used in the measurement technology like for instrument transformer. Instrument transformers are used in high-voltage engineering to decrease the voltages and currents to a more manageable level. The advantage of measuring lower voltages or currents are in a more favourable measurement equipment design. An additional benefit of instrument transformers is the electricall isolation between the measuring object and equipment. The utilisation of instrument transformer can be characterised into measuring and protection purpose of the power grid. *Voltage transformers* are basically secondary no-load operating transformers for the purpose to transform the primary (high) voltage to a more practically (lower) one, preferably at 100 V. For an ideal transformer, the measured voltage magnitude is proportional to the primary one, depending on the winding relation, and the two voltages are in phase. *Current transformers* are basically secondary short-circuit operating transformer to transform the primary (high) system current to a lower measureable level, preferably between 1 A to 5 A. [52]

Regarding the same principal construction of instrument transformers to power transformers, they may also be driven into saturation during GIC events. In the case of incorrect operation of measurement equipment, this can lead to misbehaviour of protection and control units. Consequences of incorrect measurements in the case of instrument transformer saturation are, for instance, misoperation of current differential protection relays due to an unbalanced current equilibrium. It is assumed, that DC offset saturation from GIC alone is unlikely, but protection engineers should take into account the presence of GIC and simultaneously fault operation conditions of the network. [49]

Shunt reactors. The purpose of shunt reactors is compensating capacitive reactive power and voltage control of long and low-loaded transmission lines. The construction of shunt reactors is similar to transformers, but the crucial difference is the core design. The core limb can be designed as several separate packages with air-gaps (ceramic plates) [53] between or straightforwardly as an air-core reactor. Due to the air-gaps and hence a higher reluctance, thermal investigations [43] revealed a significant lower sensibility to DC than normal power transformer. Air-core reactors have no ferromagnetic core and do not saturate by DC. [49]

Capacitor banks. In contrast to shunt reactors, capacitor banks compensate inductive reactive power, mostly occuring under full-load conditions. During half-cycle saturation, the increased harmonic currents through the capacitors rise the RMS-current and may stress the component up to tripping of the banks. [49]

Overhead line conductors. Investigations of conventional conductors, for example aluminium core steel reinforced (ACSR) and high-temperature low-sag (HTLS) conductors are performed due to DC stress and temperature. It has been proven, that for AC operating currents of 1 200 A with additional DC exposure of 52 A the temperature rise for all tested conductors were about 8°C. The line sag for conventional conductors was increased between 0.09 to 0.12 m for a 300 m ruling span compared to HTLS types. [49]

Generators. Typically, the second order harmonic (negative sequence) is expected to be low. If the 2nd harmonic rise due to DC occurrence, this can lead to generator heating [48], [54].

2.4.4 GIC Effects on Pipelines

Corrosion impact is one of the major concerns for gas and oil pipelines. The electrochemical process causes a drift of cations from the metallic pipelines to the soil. For unprotected buried pipelines this means a great exposure to corrosion. Corrective action, besides well-coated pipelines, is cathodic protection systems, which mitigate the loss of cations. This measure provides a negative pipeline potential compared to the surrounding soil of approximately - 850 mV, depending on material and soil properties. The pipe-to-soil voltage causes an equilibrium between the current flow from the system to the material and the loss of cations to the soil. [55]

In the presence of the varying GMD, positive and negative GIC cycles impact the pipelines and protection systems. In the presence of GIC, the pipe-to-soil voltage may increase to a level exceeding the protection system level, causing higher corrosion in case of failure insulation. A more serious consequence of GIC events is the incorrect measurement of the pipe-to-soil voltage and consequently unreliable protecting operation. Recommended measures against GIC impact on pipelines are continuous electrical system groundings and mitigate voltage fluctuations. [56]

2.5 GIC Mitigation Techniques

Knowing the transformer is exposed to higher DC transformer neutral current, several mitigation approaches are suggested in the literature and from transformer manufactories. Some of them develop additional equipment to mitigate DC flow in the transformer or suppress the symptoms of DC. Other suggestions concern the TSOs operation strategy or use GMD forecasting to estimate the GIC impact in the power grid. Generally, the mitigation techniques can be divided into two main categories, which are discussed in detail subsequent:

- passive or active electrical components (GIC blocking devices) which can be installed in the network,
- operational strategies to minimise the GIC impact on the power system.

The work of [42] focuses on DC blocking devices and their effectiveness to protect the power system. It points out in the paper, that blocking devices are more reliable than operational modifications because blocking devices are permanently installed in the system. In contrast, human switching operations may be limited by transmission overload or switching state and therefore reduce effectiveness and flexible modification changes for GIC mitigation. Moreover, operational actions may not reach the desirable GIC reduction to TSOs for safe power control. On the contrary, recommendations in [35] emphasise GIC monitoring system in conjunctions with operational guidelines, determined by GIC power grid susceptibility.

2.5.1 GIC Blocking and Mitigation Devices

The conceptual design for blocking devices in the transformer neutral requires, of course the DC blocking of the power grid, but also should for the flow of nominal AC currents (normal operation and fault current). Active DC blocking devices operate when the threshold of GIC level is exceeded and turn to normal operation manually or automated after GMD events. The design must also deal with AC faults (most common in the transmission grid are single-phase earth faults) with high AC amplitudes during a short time. Whether capacitor or resistor, both components are installed in the transformer neutral in parallel to the spark gap and fast-operating switching. The spark gap protects the blocking device against over-voltage and the bypass circuit provides a path in case of ac fault condition. An automated turn back to normal GIC blocking operation after the fault should be implemented in the conception. [57]

Installation of the blocking devices in the neutral of an autotransformer will not have the same effect as for the other transformer types. Due to the winding construction of these transformers, the DC will only be blocked in the common winding, but still flowing in the series winding and therefore the blocking device will be relatively ineffective for autotransformer. [57]

Another consequence of blocking devices is that on the one hand, they admittedly protect the power grid components close to the application point, but on the other hand, they cause a higher GIC flow in other parts of the network. This will concentrate and increase the GIC levels in those areas, if there is no wide spread utilisation. Implementation of DC blocking devices in all substations will be cost intensive and may not be expedient. Repercussions of placing the blocking devices to any specific power grid point can be performed by network simulation and will support the decision of network operators, in which network point it makes sense to install blocking devices or not. [58]

2.5.1.1 Passive Measures

Passive measures to less GIC sensitivity can be performed by transformer design, using an increased core cross-section, but this will have various disadvantages like greater transformer size, rise in noise and cost increase [40]. Hence, other approaches are outlined and discussed.

Series capacitor in-line. One possible approach to block DC currents in the system are capacitors in the network in each conductor phase. Series transmission line capacitors are already highly used in the Western Electricity Coordinating Council (North America) for reactance compensation. It is reported, that for those power system networks, the GIC is reduced by only a maximum of 22 % in total. Implementation of capacitors only against GIC will change the system configuration and besides that, this will be an ineffective economical decision [48] for TSOs, because the components in the lines are costly in design due to AC high voltage withstand and rating currents. [57]

Series capacitor in transformer neutral. This approach was developed in the early solar impact studies to protect only a few highly endangered transformers in the power grid. Assumed in that approach was a locally (and not wide-ranging) phenomenon of GIC. Installing capacitors in all transformer networks will again cause impedance changing for safety relays and possible resonance effects in the power grid. This strategy must be carefully examined for its repercussions. Some design considerations are recommended in [48] like withstand of DC voltages or fault conditions. [57]

Resistor in transformer neutral. A global installation of a resistor in the neutral points will reduce the GIC level for certain transformers in the network. This approach would also be more reliable and less cost-intensive due to design compared to installation point in the lines. However, a resistor in the transformer neutral changes the neutral point treatment of the network too. Investigations on a simple transmission line (both endings are grounded by transformers) indicate

for a 2.5 Ω neutral point resistor a GIC reduction of 90 % for short line lengths, the percentage decreases to 55 % for longer line lengths above 400 km. [57]

2.5.1.2 Active Measures

Alternative blocking technique. Another approach for GIC blocking in the neutral, unlike the traditional methods, is given in [59]. The idea is to provide a still solidly neutral AC grounding with a simultaneous DC disconnection by fast semiconductor switching in the grounding when transformer half-cycle saturation occurs. They suggest a switching frequency range of the blocking device of 1.2 kHz and a duty cycle of 0.25 based on a 60 Hz power frequency system. The fast switching frequency ensures that there is no increase of neutral voltage and hence no change in system operation, but a too low switching frequency may have negative effects on the fault detection system. In case of fault detection, the device is bypassed within 1.5 ms. Duty cycles determine the time for neutral connection to ground for each switching cycle. Therefore, the duty cycle only suppresses, and does not completely prevent, GIC flowing in the grid.

DC compensation winding. This method uses additional windings in the core of the transformer to inject the same DC ampere-turns as produced from GIC, but in the opposite direction. The two DC fluxes of the impressed DC source and GIC cancel each other in the magnetic circuit, which results in no direct magnetisation of the core and hence impresses the half-cycle saturation. This approach of countermeasures suppresses the symptoms of DC magnetisation, but does not prevent the DC flow in transformer or transmission lines. One of the challenges for the controlled DC injection is the accurate measurement of the DC magnetisation. [40], [48]

2.5.2 Operational Risk Management

Another subject to GIC mitigation technique is to perform risk assessment under GMD influence and work out operational strategies to reduce the impact. Therefore, various GIC scenarios are simulated on the power network to find endangered points in the network. Since they are localised in the model, strategies are prepared to minimise the GIC stress for the transmission assets. This can involve another network switching state (if possible), activate blocking devices or reduce power load flow in risky transmission segments. Investigations on GIC risk management pointed out, that only DC monitoring systems are insufficient for countermeasures GIC risk management. Two reasons for this are stated: firstly the sudden occurrence of high GIC flow and therefore inadequate lead time and secondly, when a GMD event occurs for a long period with no significant high GIC values, but (unnecessary) preventive GIC measures are already initiated.

Consequently, it is suggested for an efficient GIC risk management, also including GMD forecasting besides the DC monitoring system. Three main properties on the monitoring system are worked out in [60], namely data of the geomagnetic disturbance indices, measurements of the DC in transmission lines / transformer neutrals and the power system total harmonic distortion / reactive power flow. [61]

Protection guidelines. To reduce the stress level of power system utilities during serious GMD events, protection guidelines are worked out in [48], [60] and are discussed in detail in [35]. Generally, the recommendations can be differentiated into equipment and system protection guidelines. Several main subjects of the guidelines [23], [35] are summarised and outlined below:

- Ensure that neutral blocking devices are ready for use (if available)
- Adjust relay settings according to harmonics, over-voltage and over-current limits to prevent false trips (for example 2nd harmonic filter)
- Switch to a more safer network state
 - More evenly spreading generation
 - Reduce transmission rated capacity
 - Reducing loadings of sensitive transformers
 - Return transmission lines from maintenance work
 - Redispatch
- Providing more free reactive power control to be more resistant to transformer saturation effects
- Lower system voltage set points against over-voltage damages (rise of I^2R losses)
- Reduce switching operations to avoid instability (harmonic resonance)
- Choose appropriate transformer types (future arrangements)

Some of the guidelines are in conflict with system protection and secure system operation; hence a careful evaluation of the measures has to be done by TSO. It has been pointed out in [23], that overprotection of system utilities especially causes most of the power grid problems.

Space weather forecasting system. The forecasting system of space weather involves the impact of GIC on the power transmission system. Requirements of the forecast are worked out and the specifications classified in different timescales for GIC events, stated from a year ahead to hourly near real-time ahead. Besides the timescales, evaluation of the consequences of higher reactive power consumption in the power grid during GMD is performed. This evaluation covers generator transformers and customer equipment. The benchmarked results of the screening and the GIC impact is then communicated with the grid operator. A combination of the forecasting data with further DC transformer measurement systems completes the operational GIC risk monitoring system. [61]

Algorithm development for an automated geomagnetic storm detection is presented in [62]. For the forecasting the work uses data of the solar wind, measured at the Advanced Composition Explorer satellite (operates by NASA) at the Sun-Earth Lagrange point 1, in conjunction with the geomagnetic observations on the ground. Put simply, the first step of the automated storm detection software is the CME shock detection from the satellite, considering solar wind speed, proton density, ram pressure and proton flux as parameters for storm conditions. If these parameters fulfil the stormy criteria, a warning will be set which indicate a possible storm arriving within the next 30 minutes. Consequently, the second step includes the combination of the CME data with a wavelet analysis method [63] of the magnetic observatory data. After this approach confirms storm conditions, an alert is set, meaning storm occurrence within the next 24 hours. Other similar GMD warning systems are developed by [64], which offer a more complex approach.

2.6 International GIC Research and Working Groups

Based on GIC events on the human infrastructure in the past, research of GMD was primarily performed by geophysics. Due to the fact that GIC also occur on power transmission grids and can lead to network operational problems and blackouts, the GMD phenomena comes to the fore for engineers and TSOs all over the world. First studies of this topic are done in Northern America and Scandinavia because of the potential higher risk of GIC and after time, GIC research becomes present in other countries too. Besides those investigations, working groups are created in countries and energy communities to enhance the GIC research field. This is also leading to an IEEE standard for GIC capability of transformers in the power transmission grid.

A selection of GIC studies is given below:

- Northern America [14], [42], [49], [65]
- Norway [8], [66],
- Sweden [27],
- Finland [8], [10], [67],
- United Kingdom [58], [61],
- Spain [68],
- Russia [69],
- South Africa [28], [70],
- China [71], [72],
- Australia [29], [73]

2.6.1 NERC

Determined by the power system blackout at Hydro-Québec and due to the report [74] of the US Department of Energy, grid operator concerns about the impact of GIC are emphasised, especially in North America. The North American Electric Reliability Corporation (NERC) is an international regulatory authority for the United States, Canada and a small part of Mexico with the mission to risk reduction and assure reliability and security of the grid. In 2010, they decided to force a task force for geomagnetic disturbance study with the goal to bundle the GMD knowledge. NERC is one of the first to consider GMD seriously in the power industry; hence they have a huge knowledge about analysing, monitoring, protecting and managing GIC. [49]

2.6.2 EURISGIC

In the year 2011, the community research and development information service from the European Commission starts the EURISGIC-project with the topic “European Risk from Geomagnetically Induced Currents”. One subject of the research deals with a European GIC real-time prototype forecast system in power grids, combining data of solar storm and Earth’s magnetosphere observations. Another topic is investigation of worst-case scenarios [75] based on historical magnetic data from 1996-2008. During the observation time, the maximum GIC values indicate more than a hundred amperes for Nordic countries because of the stronger geomagnetic variations and small ground conductivities. Compared to the northern countries, maximum GIC values in Central and South Europe are expected to be about 3 to 5 times less [75]. Most relevant for this thesis is the work of the conductivity structure in the European lithosphere [76] the 1D-layered earth conductivities in which are used later on to calculate the geoelectric field. [77]

2.6.3 IEEE Guide

Since 2015, a new IEEE guide (IEEE C57.163-2015) for the capability of power transformer under geomagnetic disturbances was established. It specifies the transformer performance and parameters to minimise the impacts of GIC. The intent is to evaluate the GIC susceptibility to thermal response, additional increasing reactive power consumption and current harmonics to give recommendations to transformer requirements and design. In order to achieve the transformer specification, a GIC signature profile is introduced. Fundamental to the signature are base currents with lower magnitude but longer duration time and the other way around with short, intensive GIC pulses. Depending on the location and structure of the power grid, the GIC signature can be customised to the estimated GMD events. Applying the signature profile to transformer field investigations, the temperature limits (see Table 2-5), according to the transformer components, are recommended to mitigate negative impacts. [15]

The IEEE standard also recommends an evaluation process of transformer susceptibility on GIC effects in the power grid. Two subjects are necessary for the evaluation, namely the transformer design [78] and the expected GIC exposure in the grid. The transformer classification ranges from A for no susceptible to D for highly susceptible transformer design. Typical for classification A is a transformer with a HV delta winding connection. Three-phase three-limb core-type transformers are classified as B, other core-type transformers than B are C (T-beam, near-core flitch-plates or tie-rods). The last classification D considers core-types (steel bolts through core limbs) or shell-form. Besides the design, the exposed GIC level to a transformer is defined as high, medium, and low. The conjunction of the two classifications results in following total transformer susceptibility given in Table 2-6. The categorisation in the table gives information about what may be concerned by industry; so for category IV and III magnetic and thermal evaluation, category II only magnetic modelling and for category I no further action is suggested. [15]

Table 2-6 Categorisation of transformer total susceptibility to design and GIC exposure. Low, medium and high refer to the GIC exposure per phase. Source [15].

Classification / GIC Susceptible	Low	Medium	High
	$GIC \leq 15 A$	$15 A \leq GIC \leq 75 A$	$GIC \geq 75 A$
No (A)	I	I	I
Least (B)	I	II	III
Medium (C)	II	III	III
Highly (D)	II	IV	IV

2.6.4 CIGRE Working Group

The international council on large electric systems (CIGRE) is a non-profit association with experts in the field of electrical power generation, transmission and distribution. The goal is to collaborate with experts all over the world to discuss future developments and transfer knowledge. In the year 2013, a new CIGRE working group WG C4.32 was established with the focus to characterise the types of geomagnetic storms, identify the magnetic disturbance sensitivity to grid orientation or consider actually solar storm warning systems. [79]

2.7 Summary

Relevant literature for this thesis on space weather and the relation between geomagnetic disturbances and impacts on human infrastructure has been presented. It has been outlined, the coherence between coronal mass ejections, solar wind and geomagnetic disturbances. Investigations on the solar cycle give periods of approximately 11 years of higher likelihood for stronger GMD events. Although Austria is a mid-latitude country with lower geomagnetic field variations compared to regions closer to the magnetic poles, due to the particular earth structure with Alps and valleys, it is assumed a higher risk potential to significant GIC values.

In the context of the subject of the thesis, DC effects on the high voltage power transmission system have been especially under investigation. The most relevant issues of power transformers for the thesis like transformer magnetic circuits, types and vector groups have been reviewed. According to current flow's requirement for a closed loop, this can only be satisfied with a grounding connection of the transformer. The high- and extra-high-voltage level provides such a loop because of the star-connected windings and direct-grounded neutral point of power transformers. Although the medium- and low-voltage level (may) operates with the same vector group and neutral point treatment, the short line-lengths and higher line resistances suppress GIC effects to negligible values.

Furthermore, the most danger on transformer during GIC is quoted as the half-cycle saturation. Studies of various transformer types show, that the most sensitive ones are single-phase and shell-form transformers. Saturation effects cause nonlinear transformer conditions, results in an abnormal rise of magnetising current and therefore reactive power demand, which may lead (in the worst case) to transformer damage or system voltage instability. Besides the risk of high reactive power consumption, even and odd harmonics occur during half-cycle saturation and are assumed to be more hazardous to power systems, because of misoperation and tripping of relays. Recommendations are given to review the relay settings regarding harmonic thresholds. In addition, increasing noise levels of (even) minor DC components or temperature rise of structural steel parts in transformers caused by eddy currents are significant for GIC. The consequences of GIC on other power system utilities like instrument transformers, shunt reactors, capacitor banks or overhead line conductors are stated, as in addition corrosion effects on pipelines.

Several mitigation techniques are developed since the knowledge of GIC impacts on man-made technologies. It is outlined the strengths and weakness of each mitigation strategy, which can be categorised into passive and/or active measures and operational risk management. TSOs have to evaluate which strategy is more practicable for their grid and provides continuing grid security and protection. It seems a good and appropriate approach for a safe power grid operation, applying a mixture of blocking/mitigation devices to sensitive and endangered points in the grid.

Several working groups at an international level are currently active in GIC investigations in power transmission systems.

3 GEOMAGNETIC FIELD MEASUREMENTS AND ACTIVITY INDICES

This chapter deals with the measurement of the three-dimensional geomagnetic field and outlines the geomagnetic indices K , K_S , K_p , a_p , A_p and Dst . Additionally, the K_p index for one year is analysed in detail.

3.1.1 Magnetic Field Data

Several distributed geomagnetic observatories around the world measure the terrestrial magnetic flux density by magnetometers. From that recordings, the geomagnetic field can be derived. The Austrian meteorological institute ZAMG provides data of the geomagnetic field from the Conrad Observatory station, which are used for this research. The Conrad Observatory is member of the International Association of Geomagnetism and Aeronomy (IAGA) with the IAGA code WIC and monitor continuously and in real-time the geomagnetic field variations. The geographic coordinate of the Austrian observatory is 47.93°N and 15.862°E , so it is located southwest of Vienna at an altitude of about 1 000 m. [80]

The geomagnetic field are recorded in the three-dimensional coordinates

- x ... northward direction,
- y ... eastward direction and
- z ... vertically downward direction

with the data interval of one second. This sample interval is much higher compared to the normal 1 min sample rate which is more common for geomagnetism.

The geomagnetic data are available for the same observation time as for the later on transformer neutral current field measurements. According to the spatial extension of Austria and its location as a mid-latitude country, the measurement from that one geomagnetic observatory is assumed to be representative for the whole investigated area, for Austria.

3.1.2 Geomagnetic Indices

A geomagnetic disturbance has different characteristics like the duration or field amplitude changes. For the same GMD event, the amplitudes of field variations within a specific period differ between observatories close to the magnetic poles and for equatorial stations. Therefore, standard algorithms were developed in the past to describe the phenomena at different magnetic observatories and bring them to standardised indices, which are established today in space science.

The observation of the surrounding interplanetary medium or the magnetosphere has a long history. Whether the research is done by looking through a telescope, by graphing swings from a compass needle or by modern magnetometers in observatories, they are all using geomagnetic indices to interpret the data and variations in the magnetic field. [81]

For geophysics, the source of the terrestrial magnetic field variations is classified into two parts:

- *internal* sources leading to the earthly variations and
- *external* sources that results in transient variations.

Furthermore, the transient variations have different origins like the regular ones, which correspond to daily occurrence of fluctuations during certain periods at specific locations and tends to be from ionosphere movements. In contrast, the irregular variations concur to arbitrary,

suddenly occurred field variations and decrease after time. Best example for irregular variations are disturbances of the geomagnetic field caused by solar flares. [81]

The IAGA officially recognised a list of various geomagnetic indices to characterise the geomagnetic field variations, also called the geomagnetic activity. The most common one, which are used in this work, are outlined in the subsequent section

3.1.2.1 *K Index*

The *K* index characterise the local geomagnetic activity within a 3 h time interval ranging from 0 to 9 for UT. For each period, the maximum variation amplitude of the horizontal (northward and eastward) magnetic field components - relative to quiet days - defines the disturbance. In other words: the index describes irregular variations caused by solar particle radiation within a 3 h interval, after eliminating the regular daily magnetic variation. It should be noticed, that the computation of the regular daily variations is not a clear process in geomagnetism, it is more a subjective procedure. [5], [81]–[84]

Table 3-1 classifies the quasi-logarithmic *K* scale to the disturbance variation range *R*. The characteristic range *R* describes the 3 dimensional components of the magnetic field. Suppose that the vector has a fixed origin point, the end-point of the vector is drawn during a 3 h time-period. Enclosing a rectangular box around the drawn curve, the edges of the box is the range volume (highest and lowest field deviation) and the longest edge defines *K*, with each station has their unique limits. [83], [84]

Table 3-1 Relation between the quasi-logarithmic scale *K* according to the disturbance variation range *R* in the most disturbed magnetic component adopted from [83], [84].

<i>K</i>	0	1	2	3	4	5	6	7	8	9										
<i>R</i>	..	5	..	10	..	20	..	40	..	70	..	120	..	200	..	330	..	500	..	γ

3.1.2.2 *K_s Index*

As mentioned, the local *K* values are characteristic for each observatory and therefore the seasonal amplitudes of disturbances depend on geographical and geomagnetic latitudes. A conversion table was introduced by Bartels [85] to adjust the *K* index and make them comparable between observatories, which led to the standardised *K_s* index. The index is derived from 13 selected observatories, which are locally distributed in north and south latitudes throughout the subauroral zone. The *K_s* values are more precisely than the *K* values, because the intervals between two indices are divided by three. For example, the range between 3.5 to 4.5 is divided equally into thirds, which denoted for the *K_s* indices 3-, 3o and 3+. [83]

3.1.2.3 *K_p Index*

Based on the *K_s* indices, the average value of all selected observatories is calculated and yields to the global and well-known *K_p* index, which is used in the thesis to describe the geomagnetic activity. The index is an accepted planetary indicator to characterise the geomagnetic storm magnitude and is calculated for a 3 h time interval. [5], [82]

A classification of the geomagnetic activity is given in Table 3-2. The *K_p* indices below 4- correspond to weak geomagnetic activity, moderate activity defines values between 4- to 6+ and parameters higher than 6+ indicates to strong geomagnetic activity. [80]

Table 3-2 The 3 h planetary K_p index, the equivalent a_p , and the classification of the weak, moderate and strong geomagnetic activity.

K_p	0o	0+	1-	1o	1+	2-	2o	2+	3-	3o	3+	weak
a_p	0	2	3	4	5	6	7	9	12	15	18	
K_p			4-	4o	4+	5-	5o	5+	6-	6o	6+	moderate
a_p			22	27	32	39	48	56	67	80	94	
K_p			7-	7o	7+	8-	8o	8+	9-	9o		strong
a_p			111	132	154	179	207	236	300	400		

In the following analyses, the K_p index in the year 2017 is under examination, in order to give an overview of the geomagnetic activity during a one year observation. Therefore, the time series of the activity index are plotted in the upper part of Figure 3-1 and scaled into sections of weak (blue), moderate (green) and strong (red) geomagnetic activity, as defined previously in Table 3-2. The indices between each section are differentiated by the brightness level of the basic colour. This gives an overview on what time in the year higher and lower K_p -values occur. It can be seen that there are four days in the one-year observation, where strong geomagnetic activity occurs.

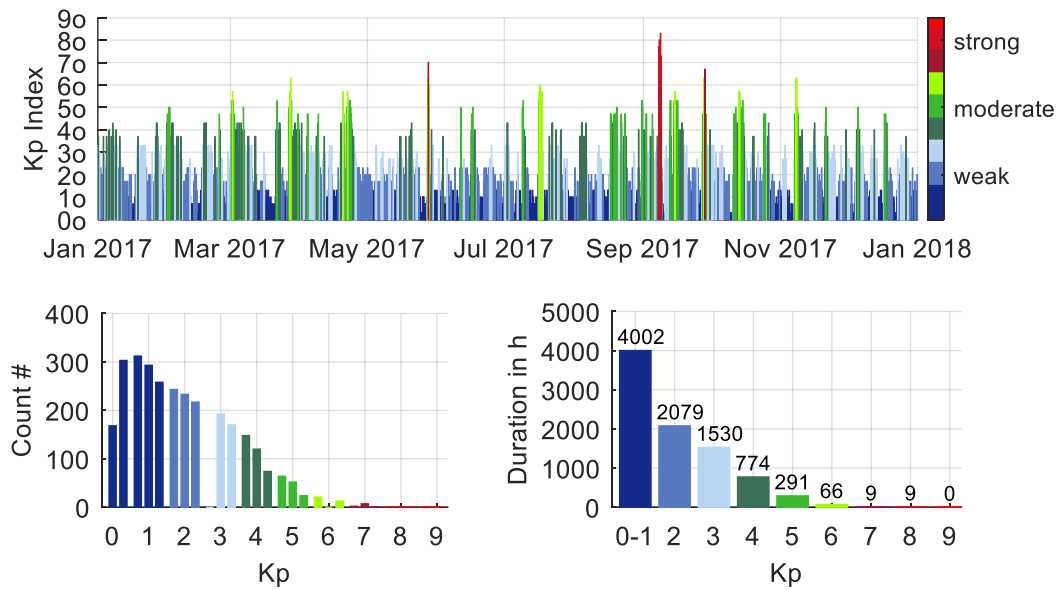


Figure 3-1 Observation on the 3 h global K_p index in the year 2017 with the geomagnetic activity classification weak (blue), moderate (green) and strong (red). The left bottom plot indicates the statistical frequency of each K_p value, the right bottom plot outlines the duration time.

A frequency distribution based on each index-value is outlined in the left bottom plot in Figure 3-1. It can be derived from the subplot that about 86 % are weak, 13 % are moderate and less than 1 % are strong geomagnetic activities of the observed period in the year 2017.

In addition, the duration of each index level is outlined in the right bottom subplot. The focus of interest is the duration of strong and high moderate K_p -indices, which statistically leads to increased geoelectric fields and hence results in higher GIC in the power transmission grid. It is displayed that the risk of higher GIC exposure in the year 2017 are in total 84 h, specifically 18 h are identified to significant strong geomagnetic activity.

3.1.2.4 a_p and A_p Index

The a_p and A_p indices are related to the K_p index and also characterise the intensity of the geomagnetic activity. Since the K_p index is non-linear, an arithmetic mean value calculation over hours, days or months is not meaningful. For a linear scale, the a_p index can be derived from the K_p as listed in Table 3-2, which value is also defined for a 3 h time period. The A_p index is the average mean value of all 3 h indices during a day.

3.1.2.5 Dst Index

The hourly disturbance storm time (Dst) index describes the magnetic disturbances caused by the ring current. It has observed that the variations from the horizontal magnetic field H during a geomagnetic storm can be considered as a uniform magnetic field, axially symmetric to the magnetic dipole axis. This implies magnetic variation independence of local time and longitude. The magnetic field of the ring current decreases the intensity of the earth main field [2]. By enhancing the ring current from solar particles, most major storm onsets cause a sudden decrease of the geomagnetic field measured on earth surface, which indicates negative Dst values. [7], [81], [86]

The actual parameters are from four different substations, nearly equally distributed at longitude. Three are in the north and one is in the south, but all observatories are all located within the 18° to 35° north or south latitudes. [7], [81], [86]

3.2 Summary

In this chapter, the geomagnetic field measurements from the ZAMG and their 3-dimensional components northward (x), eastward (y) and vertically downward (z) are presented. The fields are sampled every second and it is assumed, that the one measurement close to Vienna is representative for the investigated area (Austria) in this thesis.

Several geomagnetic indices are outlined in the thesis. The most relevant one for this work is the K_p index, which represents the geomagnetic activity for a 3 h period on the scale from 0 to 9. Investigations of the K_p index for the year 2017 revealed that most of the time, exactly 86 %, the geomagnetic activity is between 0 to 3+, which means weak activity. For 13 % of the observation time, the index is between 4- to 6+ and therefore moderate. Crucial for geomagnetically induced currents are strong geomagnetic activities, which are indicated by K_p values higher than 6+. Those strong activities occur on less than 1 % in the year 2017, or in other words over 18 h. During that time, the risk of high GIC occurrence in the grid significantly increases.

4 FIELD MEASUREMENTS OF TRANSFORMER NEUTRAL CURRENTS

This chapter covers the field measurements in the transformer neutral that are performed in Austria. It defines the measurement requirements and outlines the main components of the applied measurement unit. The system is designed for adaptable installation and working as a standalone DC monitoring system, providing real-time web application. Further it quotes the locations of the field installation points in the Austrian transmission grid.

4.1 General on DC Monitoring System

Literature research on the specific subject GIC or DC measurement systems in the transformer neutral revealed various systems with different properties and specifications, especially in northern countries with higher GIC. Based on the research, principal configuration and settings can be derived from that which are necessary and practicable for DC recordings in Austria. For the thesis, following definition for an appropriate measurement unit and DC monitoring system is formulated:

“A long-time, mobile and standalone DC monitoring system for outdoor installation with automated data acquisition / storage / update and remote access.”

First investigations of the currents in the transformer neutral are performed with a power network analyser device, which are utilised for the later on selected measurement equipment and measurement system design. The recordings indicate, that the DC component is very low compared to the 50 Hz component of the signal, which claims an appropriate and accurate DC measuring concept. This concept must consider that most of the observed time the DC level is very low, until higher GMD events occur, where the DC may increase to significantly higher amplitudes. Both magnitude levels should be measured sufficiently accurate in the presence of AC components. Based on the literature research, the expected frequency spectrum for GIC is between 0.01 mHz up to 1 Hz (see subchapter 2.2). So the frequency range of interest is from DC up to 1 Hz; all other AC components higher than the range should be filtered from the current. Additionally, the measurement system should also withstand high neutral currents in case of power grid faults. Due to the installation point in the substation close to the transformer, investigations to possible electric and magnetic field influence to the measurement components from transformer and overhead lines have to be performed.

The measured DC values should be observed continuously over years for evaluating the GIC impact in Austria. For such a long observation time, long-time stability of measurement components, temperature coefficients and other environmental impacts should be considered for design and complete the requirements of the measurement system.

A mobile design of the measurement system was chosen due to a flexible and easy installation in the transformer neutral via mobile earthing equipment. Therefore, assembling and disassembling of the system to any arbitrary installation point in the network can be quickly performed and will decrease human resources. The need of human resources is always cost intensive and should be minimised if possible, therefore a standalone version was also an important criteria. Standalone means, that only power supply is needed for the system to start data acquisition automatically and provide the data with no further support of employees.

For previous DC measurements, data loggers with a limited storage capacity were used for recordings [1]. Due to the small memory space, data has to be saved manually in a weekly manner from the data logger and only after erasing, a new recording could be started. This time consuming process may be acceptable for short-time observation, but not for recordings over months and years. Therefore, an automated concept has to be developed for data storage and providing.

The definition of the positive direction of the DC current is necessary for later on GIC simulation analysis. Since the DC in the transformer can flow in any direction, from the soil through the transformer to the transmission system or the other way around, following definition for positive DC flow is given for this thesis:

In this work, the DC direction in the transformer neutral is defined positive, when the DC flows from the transmission grid through the transformer neutral into the ground.

4.2 Measurement Unit

The central parts of the measurement unit include the current probe, low-pass filter and processor unit. Those main components should be selected and constructed to fulfil the DC monitoring system definition. Following requirements and criteria to the measurement unit are derived as follows:

- Ability to measure DC or very low frequency components up to 0.5 Hz in the range from ± 1 mA up to ± 20 A
 - most of the time, the magnitude is below 1 A
- Filter for undesired signal components
 - Normal operation: up to 10 A (AC), 50 Hz
 - Fault conditions: ~ 50 kA (AC) for 1 s
 - Harmonics
 - 16.7 Hz railway system frequency
- Sample rate f_s of 1 s
- Immunity against electric and magnetic fields
- Compensation of ambient temperature fluctuations
- Immunity against ambient weather conditions

4.2.1 Current Probe

One of the most relevant components of the measurement system is the current probe. The accurate DC recording over a wide measurement range with simultaneous AC in the transformer neutral is one of the most challenging task. Besides the electrical criteria, one mechanical limitation was to measure the transformer neutral current on a cable with 25 mm diameter from mobile earthing equipment. Two different types of current probes with acceptable accuracy and mechanical specifications were under consideration.

The first type of current probe using hall sensor with 1 mA resolution, offers a current range up to 30 A, a broad frequency range from DC to 100 kHz and a BNC connector. Advantage of this type was the flexible jaw, so the current probe could simple enclose the mobile earthing cable, which makes it easier to handle. This model was used for first measurements [1], but it turned out that it had disadvantages in the DC offset calibration. If an overcurrent occurs during measurement, the saturation effects of the current probe will lead to a new, arbitrary DC offset

level. An offset recalibration could only be performed manually on the equipment which makes it not applicable for long-time observation.

The second current probe is a high precision, closed loop current transducer with zero flux detector and a primary current range up to $\pm 60 A$ and a secondary current of $\pm 100 mA$. It uses a serial interface for data communication and DC power supply via the port interface. A major advantage for the long-time measurement was the automated DC compensation, compared to the first current probe. On the contrary, the cable feedthrough is disadvantageous due to the mechanical construction of a not adjustable diameter. Nevertheless, this current probe was selected as the most appropriate one for the DC monitoring system.

4.2.2 Signal Filter

The transformer neutral current exists of both DC and AC signal components. Higher frequency components, which are outside of the desired frequency range, can be filtered with either an analogue or digital filter; both can be applied for the measurement design. On the basis of the previous work [1], which uses analogue filter technologies, the same filter design was chosen. The analogue filter can be separated into active and passive filter designs.

Characteristic for passive filter is the usage of only passive components such as resistors, capacitors and inductor. Depending on the combination of the components, the frequency-dependent impedance can be designed to filter low or high frequency signals. The advantage of passive filters is for example the lower noise performance and no need of external voltage supply. One of the disadvantage is that the output voltage is not linear and changes with the load, which has to be considered for measurements. [87]

Since the development of operational amplifier (opamp), the passive filter design has been more replaced by so-called active filter which uses both, opamps and passive electrical components. Benefit of active filter design are a higher acceptable load of the output with a more linear output voltage and simple construction for low frequency utilisation due to the costly construction of inductors for that frequency range. On the contra side, voltage supply is necessary for the opamp and thermal noise should be take into account. [87]

At the beginning of transformer neutral current measurements in Austria [1] a passive filter design was chosen because of the simple realisation and the non-linearity output voltage was corrected by a factor. Since the general update of the measurement system, the filter design was edited to a more appropriate active filter design.

4.2.2.1 Active Low-Pass Filter

A briefly overview of filter design is outlined, taken from [88]. Assuming ideally conditions, frequency components of the signal, which are below the cut-off frequency f_c , passes undamped the input to the output, whereas higher frequency signals are damped. The general transfer function (4-1), gain response (4-2) and phase response (4-3) of a low-pass filter are quoted as

$$A(s_n) = \frac{A_o}{\prod_i (1 + a_i s_n + b_i s_n^2)} \quad (4-1)$$

$$|A|^2 = \frac{A_0^2}{\prod_i [1 + (a_i^2 - 2b_i)\omega_n^2 + b_i^2\omega_n^4]} \quad (4-2)$$

$$\varphi = - \sum_i \arctan \frac{a_i \omega_n}{1 - b_i \omega_n^2} \quad (4-3)$$

$A(s_n)$	transfer function
A_0	passband gain at DC
$ A $	magnitude of the gain response
φ	phase shift
a_i, b_i	filter coefficient (positive, real)
s_n	normalised complex frequency variable
ω_n	normalised angular frequency

with the filter coefficient a_i and b_i to define the behaviour of the frequency listed in for example [88] for each partial filter stage i . For odd filter order, the coefficient b_1 is set to zero. The normalised complex frequency variable s_n is defined in formula (4-4) as

$$s_n = \frac{s}{\omega_c} = \frac{j\omega + \zeta}{\omega_c} \quad (4-4)$$

$$s_n = j \frac{\omega}{\omega_c} = j \frac{f}{f_c} = j\omega_n \quad \dots \text{for } \zeta = 0$$

s	complex frequency variable
ω_c	cut-off angular frequency
f_c	cut-off frequency
ζ	damping constant

and for pure sinus waves, the damping constant ζ becomes zero.

The order m of the low-pass filter is given by the highest potency of s_n in formula (4-1) and describes the gain-asymptote-characteristic of the frequency response for $f \gg f_c$, i.e. $\omega_n \gg 1$ by $-m \cdot 20 \text{ dB/decade}$. Higher filter orders can be built by using series-cascade filter design with first and/or second filter order segments. The cut-off frequency f_c defines the frequency, where the signal damping is $\frac{1}{\sqrt{2}} \approx -3 \text{ dB}$ compared to the signal range of $f \ll f_c$. Cascading filters with the same cut-off frequency (critical damping), the -3 dB condition changes by higher filter orders, which can be corrected as outlined in formula (4-5).

$$f_{c(-3dB)} = f_c \cdot \sqrt{2^{\frac{1}{m}} - 1} \quad (4-5)$$

$f_{c(-3dB)}$	cut-off frequency for -3 dB condition
m	filter order

The quality factor Q_i describes the propensity to filter instability for each partial filter stage (higher values meaning higher instability) and can be calculated by formula (4-6).

$$Q_i = \frac{\sqrt{b_i}}{a_i} \quad (4-6)$$

Q_i	quality factor
-------	----------------

As already mentioned, the behaviour of the frequency response is defined by the filter coefficients, quoted in Table 4-1, and can be differentiated by their characteristics as follows.

- *Critical* low-pass filter design defines partial filter stages in series with the same cut-off frequency and have the smoothest transition from passband to stopband with an aperiodic step response.
- *Bessel* low-pass filter design linearise the phase response, meaning constant group delay over a wide frequency range, but has a smooth behaviour from passband to stopband and a minimal overshoot for step response.
- *Butterworth* low-pass filter design characterise a long horizontal (flatness) amplitude-frequency-response before the cut-off frequency and a sharply decrease afterwards causing a medium overshoot for step-response.
- *Tschebyscheff* low-pass filter design characterise ripples in the passband, but damping effects are significant higher after the cut-off frequency than the Butterworth design and therefore have the highest overshoot for step response.

Table 4-1 Filter coefficients for critical, Bessel, Butterworth and Tschebyscheff (0.5 dB ripple) filter design of a second order low-pass filter. Source [88].

Filter Design	a_i	b_i	Q_i
Critical	1.2872	0.4142	0.50
Bessel	1.3617	0.618	0.58
Butterworth	1.4142	1.000	0.71
Tschebyscheff	1.3614	1.3827	0.86

4.2.2.2 Sallen-Key Design

A common design for active low-pass with higher filter order is a cascade topology of decoupled amplifiers and partial filter stages with the internal gain α_i . Each filter stage topology can be designed as shown in Figure 4-1 by a Sallen-Key filter design, using formula (4-1) and the filter coefficient in Table 4-1 to calculate the transfer function for the Sallen-Key topology given in (4-7) with the cut-off frequency for second order low-pass filter in (4-8).

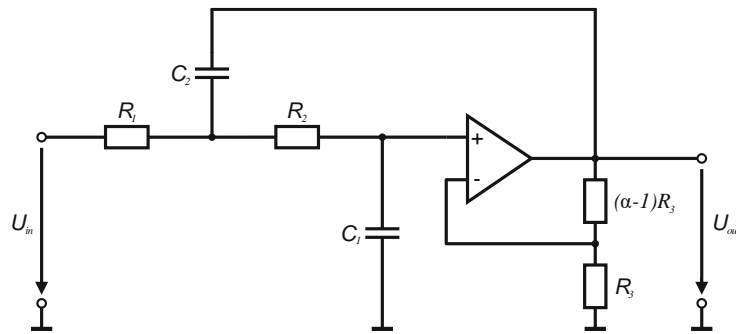


Figure 4-1 Sallen-Key design for an active low-pass filter second order. Picture adopted from [88].

$$A(s_n) = \frac{\alpha}{1 + \omega_c [C_1(R_1 + R_2) + (1 - \alpha)R_1C_1]s_n + \omega_c^2 R_1R_2C_1C_2s_n^2} \quad (4-7)$$

$$f_c = \frac{1}{2\pi\sqrt{R_1 R_2 C_1 C_2}} \quad (4-8)$$

α internal gain

For the measurement system it is not required to amplify the signal, so the internal gain is set to $\alpha = 1$. Then $(\alpha - 1)R_3 = 0$ in Figure 4-1 means, that the opamp operates like a unity-gain (voltage follower). The Sallen-Key transfer function (4-7) for $\alpha = 1$ is quoted in (4-9) as

$$A(s_n) = \frac{1}{1 + \omega_c C_1 (R_1 + R_2) s_n + \omega_c^2 R_1 R_2 C_1 C_2 s_n^2} \quad (4-9)$$

and by comparison of coefficients from (4-1) with (4-9) leading to formula (4-10) and (4-11)

$$A_0 = 1 \quad (4-10)$$

$$R_{1,2} = \frac{a_1 C_2 \mp \sqrt{a_1^2 C_2^2 - 4b_1 C_1 C_2}}{4\pi f_c C_1 C_2} \quad (4-11)$$

with the condition for real values given in (4-12).

$$\frac{C_2}{C_1} \geq \frac{4b_1}{a_1^2} \quad (4-12)$$

Considerations of the filter coefficients conclude, that the Tschebyscheff-design is not appropriate due to the ripple in the passband frequency range. It is assumed, that the critical design is sufficient for the application. Applying the filter coefficient for critical design, this yields to $C_2 \approx C_1$. Therefore, the capacitors can be defined as $C = C_1 = C_2$ and inserted into expression (4-11) results to same values for the resistors $R_1 \approx R_2$.

For the special case $C = C_1 = C_2$ and $R = R_1 = R_2$, the resistor R can be calculated given by C with formula (4-13) for critical filter design $\alpha = A_0 = 1$.

$$RC = \frac{a_1}{2 \cdot \omega_c} = \frac{\sqrt{b_1}}{\omega_c} \quad (4-13)$$

The filter design for this work can be derived from the properties of GIC and measurement requirements described in subchapter 4.2. Frequency components above the cut-off frequency, should be sufficiently damped, which consequently leads to a second order filter a damping characteristic of $-40 \frac{dB}{decade}$. Since GIC are very low frequency currents, with a frequency range below 1 Hz, the low-pass cut-off frequency is defined in this work at $f_{c(-3dB)} = 0.5 \text{ Hz}$. It is outlined in subchapter 5.2.3, that in fact the most significant GIC frequencies are below 1 mHz. The calculated low-pass filter parameters for that cut-off frequency are $C = 33 \mu F$ and $R = 6 \text{ 200 } \Omega$. The chosen filter characteristic is appropriate to measure GIC frequencies without damping effects, but damps frequencies higher the cut-off frequency, for example the 16.7 Hz

railway system frequency with -53 dB or the 50 Hz power network system frequency with -72 dB, which also fulfils the defined measurement requirements.

4.2.3 Processor Unit and Data Logger

The processor unit offers both, a BNC and a serial connector to link either the first or second current probe discussed previously. The measured and filtered signal is sampled by using a high precision 16-Bit analog-to-digital converter (ADC), which communicates with the processor unit via I²C transfer protocol. The transferred data from the ADC are saved by the processor unit, which acts as a data logger too. The processor unit saves the data with a sample rate of $f_s = 1 \text{ Hz}$ and therefore the Nyquist – Shannon sampling theorem, as outlined in subchapter 5.1.1.1, is satisfied.

For each day, a new data file will be generated with a header including name of substation, geodetic latitude and longitude, transformer name, voltage level, measuring point and data sample rate. Additionally implemented on the processor unit is a temperature sensor to measure the ambient temperature. The measured DC and temperature data are stored in UTC (Universal Coordinated Time) time-format.

The processor unit is programmed to start measurement automatically, when power supply is connected to the system, which also fulfils the formulated standalone criteria in subchapter 4.1. Besides that, also remote access and automated data transfer without using the IT infrastructure of the grid operator defines the standalone system, which is accomplished by the processor unit using a GSM module. The module provides connection to the Internet and due to that connection, password-protected remote access can be established to adjust measurement settings. A vpn-tunnel is used to send new data once per day to the server, so the measured data are saved twice and there is no need of manually data downloading.

4.2.4 Investigations on External Impacts on the Measurement Unit

External impacts like magnetic fields or ambient temperature have to be considered and possible negative influences to the measurement unit in laboratory have to be studied.

Magnetic field. The installation point of the measurement system is in the transformer neutral and therefore close to the power transformer, bus bar, overhead lines and cables. Magnetic field measurements in that area revealed magnetic fields of 5 μT and more [1]. Therefore, a test setup was created to reproduce the magnetic fields in field installation points. The whole measurement system was exposed to a 3-dimensionally field up to 20 μT (50 Hz), which is much higher than the magnetic field measurement in the substation. No impacts of the external magnetic field to the measurement equipment are recognised; neither for very low DC, relevant measurement deviations could be determined.

Temperature dependency. Ambient temperature investigations on the current probe with flexible jaw and the closed-loop current transducer are performed. Both current probes and the whole measurement system are cooled down and afterwards slowly warm up to ambient temperature with simultaneously measuring a constant DC test current. While the closed-loop current transducer measures a constant DC value, the current probe with flexible jaw shows a measured temperature coefficient of 6 $\text{mA}/^\circ\text{C}$ [1]. This means a high temperature dependency of the current probe with flexible jaw which is inappropriate for an accurate long time measurement over years with seasonal temperature variations, although the whole measurement system is integrated in a polyester case with radiator and temperature regulation. Therefore, the closed-loop current transducer is to be preferred and applied for long-time measurements.

4.2.5 Installation Point in the Field

The measurement field installation at one substation can be seen in Figure 4-2 on the left side. Bypassing the existing solidly grounding with a mobile earthing equipment and subsequent decoupling the fixed installed ones ensures, that the transformer neutral current flows only along the flexible cable through the measurement system. The measurement system is integrated in a polyester case to protect it against environmental influences like rain, wind or direct sunlight. The right picture in Figure 4-2 presents the main components for the measurement system like current probe, processor unit / data logger or GSM module to provide Internet connection. Besides that, other components are necessary for a reliable operation of the measurement system like temperature regulation or automatic circuit breaker for human protection. The green line indicates the cable of the mobile earthing equipment through the polyester case and current probe.

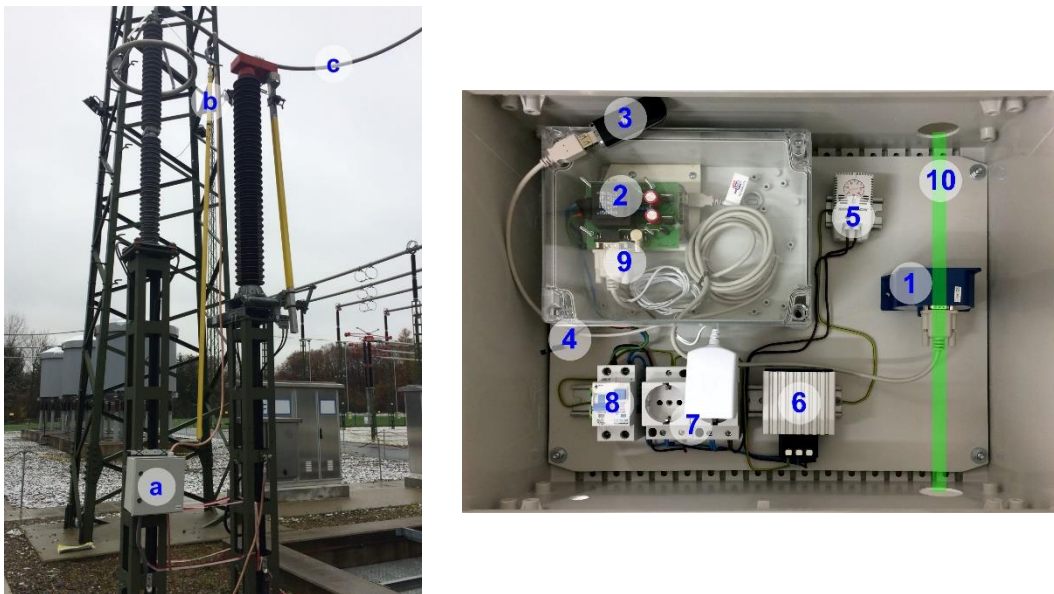


Figure 4-2 Field installation of the measurement system. Left picture shows the installation point in the substation and the right-hand side illustrates the inside of the measurement box. For details, see text below and Table 4-2. Pictures adopted from [89].

The left picture in Figure 4-2 shows the installation point in substation. The transformer neutral (c) is directly grounded via the flexible mobile earthing equipment (b), which cable goes through the measurement box (a). The right picture shows the main components of the measurement box, which are outlined in Table 4-2.

Table 4-2 List of the components which are used for DC field measurements.

1) Current probe	6) Radiator
2) Processor unit / data logger	7) Voltage supply
3) GSM module	8) Automatic circuit breaker
4) Temperature sensor	9) Data linkage cable
5) Temperature regulator	10) Earthing cable

4.3 Communication

The DC monitoring system contains three main subsystems: the *measurement unit* (represents one transformer neutral current recording), a *server* for data storage and a *web browser* to visualise the data (only for private persons). Therefore, a reliable and secure communication between the subsystems is mandatory. Concepts based on utilising the IT infrastructure of the TSO for data transfer were quickly rejected due to safety and security issues. Hence, another way was developed with a mobile broadband internet using server-client technology for data communication and therefore no usage of the system operator IT infrastructure.

The whole monitoring system is constructed as a client-server configuration, where the clients are the measurement systems in each substation and the server is a separate processor unit and data storage device. The connection between client and server is created via vpn-tunnel, which connection is tested every 5 minutes. If the connection is broken down, the client processor unit reconnects automatically to the server. Via a separate tunnel, the clients broadcast the actual data to the server for additional web application. Besides the data storage application, the server provides a web application to visualise the actual measurements of the clients for a web browser, including the transformer neutral current and temperature of each substation. An overview of the whole measurement process and monitoring system is given in Figure 4-3.

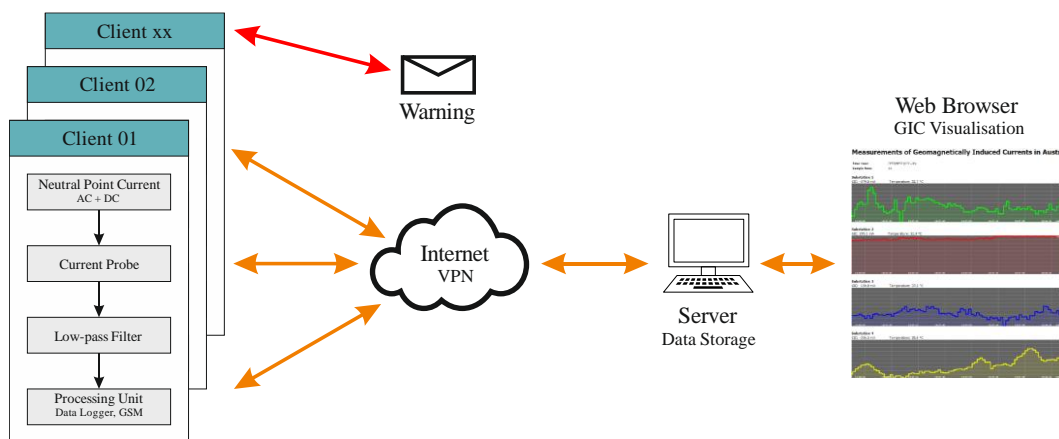


Figure 4-3 Schematic of the DC monitoring system and client-server configuration. Each client represents a measurement unit (point) in the transformer neutral, which communicates via vpn-tunnel to the data server. Actual GIC measurements are visualised over a web application.

Warning system. An additional warning system is implemented in each measurement unit, if higher GIC values occur in the transformer neutral. This is achieved by predefined GIC threshold for each client and by overtopping the limit, a warning mail is sent via GSM module to the TSO. The alert can be used for operational risk management discussed in subchapter 2.5.2.

4.4 Location of Installed Measurement Units in the Austrian Transmission System

Measurements of the transformer neutral currents are performed at five different locations in the Austrian transmission grid, four measurements are installed in the 400 kV, two are installed in the 220 kV voltage system level (the installation point of one client changed during observation time – described later on). The intention of the chosen measurement points was a geographically distribution as widely as possible. The measurement areas should take into account both - the valleys and mountainy regions of Austria and it should be installed into neutral points where significant DC magnitudes are expected.

The selected installation points are listed in Table 4-3 and visualised in the transmission system grid map of Austria in Figure 4-4. Each measurement system is assigned to a unique client number and the geographic location of the installation point in Austria is outlined with additional information of the geological structure. The rated voltage and power of the observed transformer are also quoted in the table with the voltage level of the measurement installation point denoted in bold. The client #01 and #04 are installed in the same substation, but at different voltage levels and power transformers. Due to the different starting points of measurement system developing and upgrading, the observation times varies for each client. The first measurement system was installed on April 2016, and subsequent other clients are added to the monitoring system. Since the end of August 2017, all six clients simultaneously measuring the transformer neutral currents in Austria. The location of the measurement system only changed for client #02; this is why two installation points are outlined. After an observation time of about one and a half year, the installation point was changed from #02a to another transformer neutral #02b. The total timescale of the observation time for each client is outlined in the Appendix A in Figure 8-1.

Table 4-3 List of transformer neutral measurement points in Austria and observation period.

Client	Installation Point		Transformer		Observation Period	
	Geographic Location	Geological	Rated Voltage in kV	Rated Power in MVA	Start	End
-	-	-				
#01	North-East	valley	400 /230/30	600/600/150	23.08.2016	present
#02a	South-East	valley	400 /115/30	300/300/100	08.11.2016	12.04.2018
#02b	South	mountainy	230 /110/10	220/220/33	23.04.2018	present
#03	West	mountainy	400 /115/30	200/200/100	10.04.2017	present
#04	North-East	valley	400/ 230 /30	600/600/150	31.08.2017	present
#05	North-West	valley	400 /230/30	550/550/150	11.05.2017	present

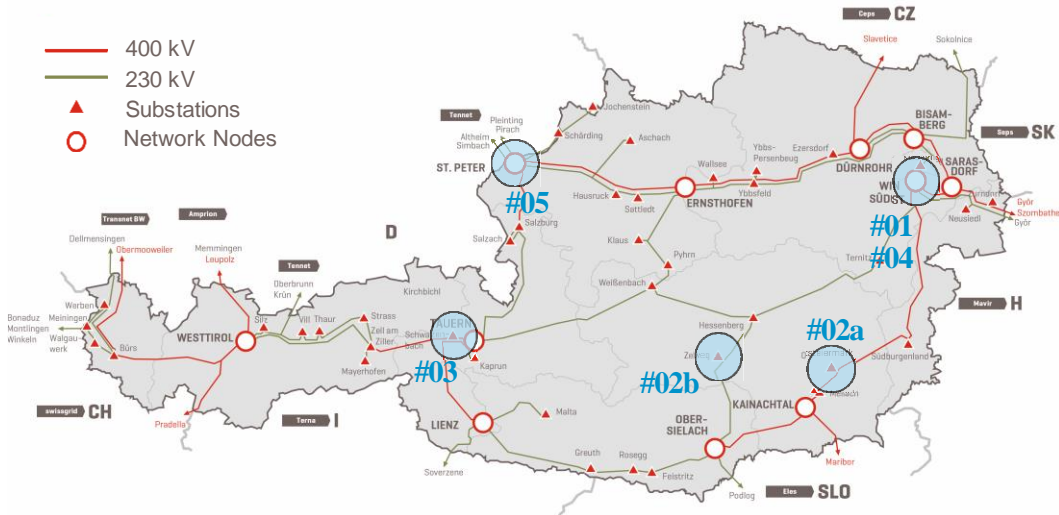


Figure 4-4 Map of the Austrian transmission system and tie lines to neighbouring transmission systems. The measurement points are marked in cyan and are assigned with the client number. Picture adopted from [90].

4.5 Summary

This chapter shows the standalone, mobile and long-time field measurement system in the transformer neutral, which was developed for this thesis. The DC monitoring system requirements were defined and based on that, the measurement components are selected and designed for a reliable recording.

The main components of the measurement unit are the current probe, low-pass filter and a processor unit for automated data acquisition, storage and data updating. It points out that the most sensitive part of the measurement chain is the current probe. Therefore, the focus was on an accurate and precise current probe, which offers a wide measurement range from a few mA to several amperes and an automated zero-flux compensation. To save processing power and storage of the processor unit, an active second order low-pass filter with a cut-off frequency of $f_{c(-3dB)} = 0.5 \text{ Hz}$ was chosen instead of a high-resolution sampling and subsequently digital filter by the processor unit.

Investigations on external impacts on the measurement unit in laboratory show, that no magnetic influence up to $20 \mu\text{T}$ were recognised. Although the temperature dependency of the applied closed-loop current transducer is very low and can be neglected, a more or less constant ambient temperature for the recordings was achieved by heating the measurement box.

The vpn-communication between the clients (DC field measurement units in the transformer neutral) and the server allows automated data uploading and downloading from the server. Additionally, it is presented that the monitoring system has a warning system implemented for higher transformer neutral currents and a web-application for realtime visualisation of the currents of all clients; so the TSO has a complete overview and control of the installed measurement units.

Up to now, five measurement units are installed in the Austrian transmission system, which are geographically distributed in the country. Therefore, they give a good overview on the transformer neutral current distribution in mountainy regions.

5 FIELD MEASUREMENT ANALYSIS

This chapter deals with the basic data analysis methods that are used for studies of the field measurements of the transformer neutral currents and geomagnetic field and finalises with root cause analysis of the measured currents.

5.1 Data Analysis Methods

A brief discourse of the analysis methods which are used for the thesis, based on the fundamentals of digital signal processing and stochastic. The main statements from the signal analysis are taken from [91], [92], for the stochastic methods [93]; both literatures are recommended for further details.

5.1.1 Digital Signal Processing

5.1.1.1 Sampling Theorem

A sampled continuous-time signal is represented by a discrete-time signal based on the sample rate f_s . The Fourier transform of the discrete-time signal are periodically repeated and shifted by multiple integer of f_s , according to the Fourier transform of the continuous-time signal. If the sample rate is too low or the signal is not bandlimited, the periodic spectra in the frequency domain will overlap each other, which means that the originally continuous-time signal could not be reconstructed correctly from the samples. This effect is known as aliasing. For a correct reconstruction, the sample frequency must satisfy the sampling theorem, which is defined by Nyquist – Shannon, as quoted in (5-1).

$$f_s \geq 2 \cdot f_{max} \quad (5-1)$$

f_s	sample frequency, [Hz]
f_{max}	highest frequency component in the signal, [Hz]

The Nyquist – Shannon sampling theorem states, that the sampling frequency f_s must be equal or higher than the double frequency of the highest component f_{max} in the signal.

5.1.1.2 Discrete Fourier-Transformation

The Fourier-Transformation is an essential signal-processing algorithm for spectral analysis of the signal. However, in the case of sampled, discrete signals with finite-length, this work deals only with the discrete Fourier-Transformation (DFT). Following expressions are given from (5-2) to (5-4) for the DFT and the inverse discrete Fourier-Transformation (IDFT). compute the DFT, a fast Fourier-Transformation algorithm (FFT) is used [94]–[96].

$$DFT: X_{[k]} = \sum_{n=0}^{N-1} x_{[n]} \cdot W_N^{kn} \quad (5-2)$$

$$IDFT: x_{[n]} = \frac{1}{N} \sum_{k=0}^{N-1} X_{[k]} \cdot W_N^{-kn} \quad (5-3)$$

$$W_N = e^{-j\frac{2\pi}{N}} \quad (5-4)$$

$X_{\{k\}}$	spectral values
$x_{\{n\}}$	sample values
W_N	basis function
N	number of samples
n	sample index
k	spectral component index

5.1.1.3 Window Function

In digital signal processing, the analysis of a real signal is limited to a finite number of samples during a specific observation time, called window. The window length $N \cdot T_s$ is related to the number of samples N (so-called block length) and the sample interval T_s . Based on that relation, the frequency resolution Δf of the spectrum can be obtained as quoted in (5-5).

$$\Delta f = \frac{1}{N \cdot T_s} = \frac{f_s}{N} \quad (5-5)$$

Δf	frequency resolution, [Hz]
T_s	sample interval, [s]

The DFT computes the spectrum of the periodic continuation of the sequence $x_{[n]}$ of the window, so the DFT implies periodic signals with integer multiples of the signal periods within the window. If the signal of the window is not periodic, the spectrum of the DFT has an uncertainty, because the periodic continuation of the window has a jump discontinuity, which does not exist in the original time-continuous signal. This uncertainty is known as the leakage effect.

To minimise the leakage effect, the sequence is weighted by a window function $w[n]$, which forces a periodic continuation of the window. Commonly window functions are quoted from (5-6) to (5-8)

- Rectangular

$$w[n] = \begin{cases} 1, & 0 \leq n \leq N \\ 0, & \textit{otherwise} \end{cases} \quad (5-6)$$

- Hanning

$$w[n] = \begin{cases} 0.5 - 0.5 \cdot \cos\left(\frac{2\pi n}{M}\right), & 0 \leq n \leq N \\ 0, & \textit{otherwise} \end{cases} \quad (5-7)$$

- Blackman

$$w[n] = \begin{cases} 0.42 - 0.5 \cdot \cos\left(\frac{2\pi n}{M}\right) + 0.08 \cdot \cos\left(\frac{4\pi n}{M}\right), & 0 \leq n \leq N \\ 0, & \textit{otherwise} \end{cases} \quad (5-8)$$

Disadvantageous of the window function is, that besides one main lobe, side lobes occur in the transformed spectrum, which frequencies do not exist in the real time-continuous signal. This should be kept in mind in spectrum analysis.

Generally, for this thesis the usage of a window function is neglected due to the frequency analysis over a long observation time (window length), meaning a good representation of the original time-

continuous signal, and therefore higher frequency resolution. However, applying no window function can also be interpreted as using a rectangular window on the complete analysed time interval as window length.

5.1.2 Stochastic Method

5.1.2.1 Empirical Cumulative Distribution Function

The general distribution function $F(x)$ in formula (5-9) describes the cumulative probability of the data vector x ($x \in \mathbb{R}$). So it defines in other words the probability, that the random variable X is lower or equal x . Properties of the distribution function are, that in case of summation of positive $f(x)$, it is non-decreasing and results in a step function. The empirical cumulative distribution function (ECDF) describes the cumulate likelihood of empirical data for $F(x): \mathbb{R} \rightarrow [0,1]$.

$$F(x) = P(X \leq x) = \sum_{x_i \leq x} f(x_i) \quad (5-9)$$

$F(x)$	distribution function
$P(X \leq x)$	probability of the event
$f(x)$	density function

5.1.2.2 Expectation Value

The expectation value of the data vector x is computed by the sum of the multiplication between the data and their probability – equation (5-10). If the values are equally distributed, the expectation value is equal to the arithmetic mean value.

$$E(X) = \sum_{i=1}^N x_i \cdot P(X = x_i) = \frac{1}{N} \cdot \sum_{i=1}^N x_i = \bar{x} = \mu_x \quad (5-10)$$

$E(X), \mu_x$	expectation value
x_i	data vector
\bar{x}	arithmetic mean value

5.1.2.3 Variance

The variance Var is the mean squared deviation of the data to the expectation value – equation (5-11). Taking the square root of the variance leading to the standard deviation σ .

$$\begin{aligned} Var(X) &= \sum_{i=1}^N (x_i - \mu_x)^2 \cdot P(X = x_i) = E((X - \mu_x)^2) = E(X^2) - E(X)^2 \\ &= \frac{1}{N} \cdot \sum_{i=1}^N (x_i - \bar{x})^2 = \sigma_X^2 \end{aligned} \quad (5-11)$$

$Var(X)$	variance
σ_X	standard deviation

5.1.2.4 Covariance

The covariance Cov is a general form of the variance to describe the deviation between two random variables X and Y as quoted in (5-12), where negative values can be obtained.

$$Cov(X, Y) = E((X - \mu_X)(Y - \mu_Y)) = \sigma_{XY} \quad (5-12)$$

$Cov(X, Y)$ covariance

5.1.2.5 Correlation

A common statistical method for investigating the relation between two data is the correlation method. Characteristically for this method is the auto-correlation function (ACF) and the cross-correlation function (CCF). The outcome of the correlation is the dimensionless coefficient r and describes the relation between both data. The coefficient is limited to +1 and -1 values, where positive values indicate in phase signals and negative values indicate in opposition signals. However, no statistical relation between the signals is given by the value 0. In general, the correlation can be classified as follows.

- weak correlation: $0.0 \leq |r| \leq 0.5$
- medium correlation: $0.5 \leq |r| \leq 0.8$
- strong correlation: $0.8 \leq |r| \leq 1.0$

Cross-correlation function. The CCF coefficient between two random variables X, Y can be computed by the covariance divided by their standard deviations, outlined in (5-13).

$$r_{XY} = \frac{\sigma_{XY}}{\sigma_X \cdot \sigma_Y} \quad (5-13)$$

r_{XY} cross-correlation coefficient

In signal analysis, the principal of the cross-correlation function is to compare the known signal $x(t)$ with the unknown signal $y(t)$. Therefore, the unknown signal $y(t)$ will be shifted by τ , multiplied by the known signal $x(t)$ and afterwards the mean value as shown in equation (5-14) is calculated. The coefficient maximum $r_{xy}(\tau)$ can differ from $\tau = 0$. [96]

$$r_{XY}(\tau) = \lim_{T \rightarrow \infty} \frac{1}{T} \int_0^T x(t) \cdot y(t - \tau) dt = \overline{x(t) \cdot y(t - \tau)} \quad (5-14)$$

τ time-shift

Auto-correlation function. The ACF coefficient between two random variables X, X can be computed by the covariance divided by their standard deviations, outlined in (5-15).

$$r_{XX} = \frac{\sigma_X^2}{\sigma_X \cdot \sigma_X} \quad (5-15)$$

r_{XX} auto-correlation coefficient

In signal analysis, the principal of the auto-correlation function is to compare the signal by itself. Therefore, the signal $x(t)$ will be shifted by τ , multiplied by the signal at the time t and afterwards

the mean value is calculated, as outlined in (5-16). The ACF can be used to find periodic components in a very noisy signal, with the coefficient maximum $r_{xx}(\tau)$ always at $\tau = 0$.

$$r_{xx}(\tau) = \lim_{T \rightarrow \infty} \frac{1}{T} \int_0^T x(t) \cdot x(t - \tau) dt = \overline{x(t) \cdot x(t - \tau)} \quad (5-16)$$

5.1.2.6 Regression Analysis

Regression analysis is used to describe the relation between one or more independent variables to the dependent variable. The simplest regression analysis is the linear regression of two variables X and Y . Therefore, a xy -plot (or scatter plot) can be used to illustrate the data; from those the linear regression fits a linear trend line $R_{Y(X)}$, which is formulated in (5-17)

$$R_{Y(X)} := y = \beta_0 + \beta_1 \cdot x \quad (5-17)$$

$R_{Y(X)}$	linear trend line
β_0	ordinate intersection of the trend line
β_1	gradient of the trend line

with the coefficient β_0 and β_1 computed with formula (5-18) and (5-19).

$$\beta_1 = \frac{\langle \delta_X, \delta_Y \rangle}{\|\delta_X\|^2} = \frac{\sum(x_i - \bar{x}) \cdot (y_i - \bar{y})}{\sum(x_i - \bar{x})^2} \quad (5-18)$$

$$\beta_0 = \bar{y} - \beta_1 \cdot \bar{x} \quad (5-19)$$

In the ideal case, the scatter plot of X and Y perfectly fits on a linear straight line $R_{Y(X)}$, which represents a perfect correlation. If there is no perfect fit, the linear regression tries to find a linear trend line $R_{Y(X)}$ within the scatter plot, where the residual e between the trend line and the points above / below (in vertical direction) in the scatter plot is minimised. In most cases the method of the least squares is used, which is defined to be a minimum, as outlined in (5-20).

$$\sum_{i=1}^N e_i^2 = \sum_{i=1}^N (y_i - (\beta_0 + \beta_1 \cdot x_i))^2 \rightarrow \min \quad (5-20)$$

e residual

Generally, the distribution of the xy -plot to the linear trend line can also be used to indicate the correlation between the data. Furthermore, an increasing gradient β_1 determines a positive correlation, a decreasing slope means a negative correlation and if $\beta_1 = 0$ indicates no linear dependence between the data.

5.2 Analysis of the Measurement

Recordings of the geomagnetic field exist since a long time and therefore data analysing could be performed over the last years. In contrast, data of the DC transformer neutral current measurements in the field of all five clients in Austria are present since September 2017, as outlined in Table 4-3.

During a long-time measurement, missing recording data can occur in consequence of maintenance work in substations and on transformers or necessary switching operations. Additionally, it was observed that “offset” jumps are present in the measurements of client #02. This is due to the current probe without automated offset compensation that is still applied for that client. However, each jump segment is corrected by the segment-mean-value.

Generally, two sample rates of the data are used to analyse the field measurements

- **Raw data**

The raw data are the recorded (original) data with a sample rate of $T_s = 1\text{ s}$.

- **Reduced data**

The reduced data are computed from the raw data by using digital low-pass filter with a cut-off frequency of $f_c = 1\text{ mHz}$ and subsequent, the data are reduced to 1 min samples.

The raw data are used for a detailed analysis of the DC measurements. Based on the raw data, the reduced data are used for faster data processing and saving memory requirement. The cut-off frequency of 1 mHz was chosen based on the assumption in subchapter 2.2, that the relevant frequencies of the GIC are far below mHz .

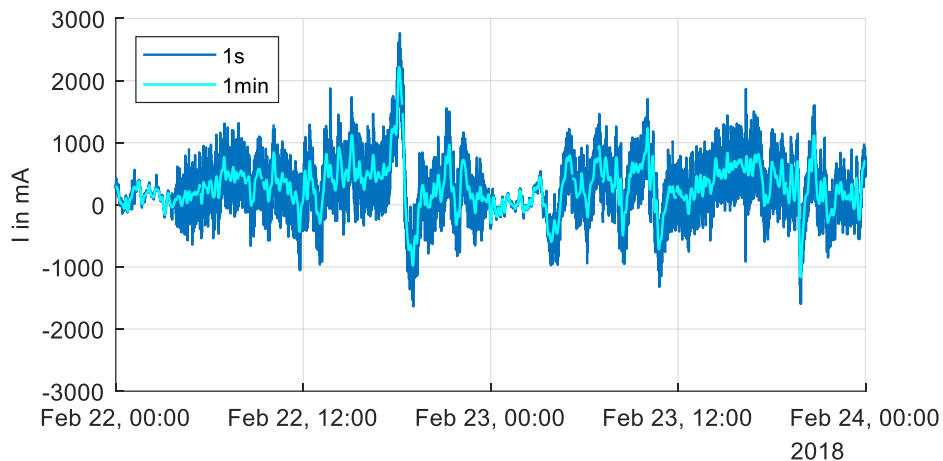


Figure 5-1 Field measurement of client #01 from 22. - 23. February 2018. Blue indicates the raw data with $T_s = 1\text{ s}$ and cyan the reduced data based on digital low-pass filter with $f_c = 1\text{ mHz}$ and down sampling to 1 min values.

An example of the transformer neutral recording for client #01 and a two days observation period from 22. - 23. February 2018 is given in Figure 5-1. (The measurements for the same observation period of the other clients are outlined in the the Appendix A in Figure 8-2.) The figure shows the raw data in blue and the reduced data in cyan.

It can be seen in Figure 5-1, that the DC polarity of the transformer neutral current changes over time, so negative and positive polarity-sequences can occur durring a time intervall from minutes to hours. During the observation time, the DC values vary between positive and negative values

with a magnitude peak value of 2 760 mA. Focussing on the low-pass filtered data and zooming in, it seems that there are periodic, very low frequency components in the signal. Furthermore, overlaying the daily DC currents over a long observation time (weeks or months), a periodic daily pattern can be derived from the recordings. A further observation is, that especially in the morning hours, the high-frequency fluctuations are lower compared to the rest of the day. The high- and low-frequency fluctuations are under investigation in detail later on.

In general, the property of the transformer neutral current observations can be classified into

- DC polarity
- DC peak values
- High-frequency fluctuations: fast-fluctuations in the range of seconds,
 $\Delta t = 1 \text{ s}$
- Low-frequency fluctuations: slow-fluctuations in the range of minutes to hours,
 $\Delta t = \text{minutes} \dots \text{hours}$

5.2.1 Stochastic Analysis of the DC Field Measurements

The ECDF analysis gives information about the distribution and probability of the measured data. For the ECDF investigation, a long-time observation period from October 2017 to March 2018 of all clients was chosen based on the sample rate of every second. If no measurement for one client is available, the recordings of all other clients are cleared for the same time, so a reliable comparison between all clients is ensured. This leads to about 165 recording-days left from the total 182 days of the 6 month.

The ECDF of magnitudes of all measurements, are plotted in the upper part of Figure 5-2. The maxima of the magnitudes are additionally marked in the plot. It can be derived from the figure, that most of the time, the currents are in the range within 1 000 mA, in fact 80 % of the transformer neutral measurements are below 500 mA. Focussing on the higher current magnitudes, which are crucial for transformer saturation, the upper range of the ECDF is zoomed between $99 \% \leq F(|I|) \leq 100 \%$, which illustrates the bottom plot of Figure 5-2.

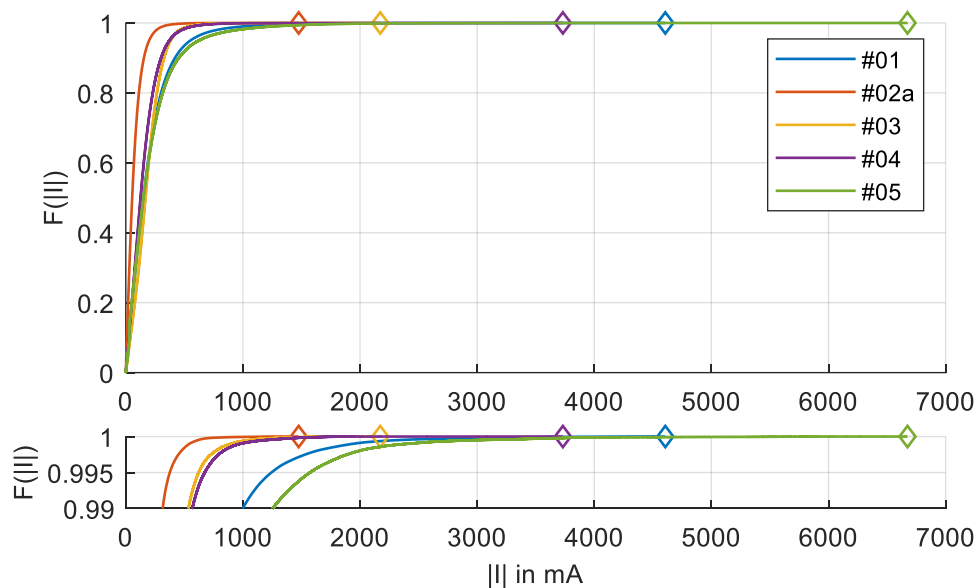


Figure 5-2 Empirical cumulative distribution function (ECDF) of the 1 s sampled measurement magnitudes during the observation time from October 2017 to March 2018. The bottom plot shows the upper range of the ECDF.

A statistical overview for the DC limitations of the raw data ($T_s = 1$ s) are outlined in Table 5-1 in grey. It can be seen from the table, that the probability P_{1A} for values higher than 1 000 mA is generally very low. Client #02a has no higher magnitude than 2 000 mA, and the probability of the same current limitation of client #03 and #04 is more or less zero. Higher currents occur for clients #01 and #05, which also reflects the probability P_{2A} for those currents.

Besides the probability, the duration time t_{Lim} gives information on how long higher currents than the current limitations occur in the transformer neutral during the observation period, which can be computed based on their probability. Magnitudes higher than 1 A occur, for example based on 1 s values, for client #01 more than 39 h, for client #05 over 70 h. Especially magnitudes higher than 2 A occur for approximately 3.5 h and 8 h for client #01 and #05.

Generally, the probabilities and accordingly the duration times are slightly higher for raw data than for the reduced data.

Table 5-1 Probability of current limits and duration times t_{Lim} during the 6 month observation from October 2017 to March 2018. Classification between raw data (1 s) and reduced data (1 min).

Client	$P_{1A}(I \geq 1A)$ in %		$P_{2A}(I \geq 2A)$ in %		t_{1A} in h		t_{2A} in h	
	1 s	1 min	1 s	1 min	1 s	1 min	1 s	1 min
	#01	0.995	0.818	0.087	0.073	39.4	32.4	3.5
#02a	0.006	0.004	-	-	0.2	0.2	-	-
#03	0.062	0.051	0	-	2.5	2.0	0	-
#04	0.092	0.056	0	-	3.7	2.2	0	-
#05	1.779	1.527	0.195	0.154	70.5	60.5	7.7	6.1

Based on the overall observation time of each client t_{obs} within the period from August 2016 to June 2018, the ECDF and probabilities of the reduced data (1 min) are computed. According to that, the duration times $t_{1A} \dots t_{5A}$ for the current limits 1 A ... 5 A are calculated for each client separately. The results are outlined in Table 5-2.

Table 5-2 Duration time t_{Lim} of transformer neutral magnitudes during August 2016 to June 2018 of the reduced data (1 min).

Client	t_{obs} in d	t_{1A} in h	t_{2A} in h	t_{3A} in h	t_{4A} in h	t_{5A} in h
#01	590.6	148.9	14.5	2.4	0.2	-
#02a	495.8	0.6	-	-	-	-
#03	442.3	10.7	-	-	-	-
#04	409.2	7.6	0.1	-	-	-
#05	266.1	78.3	10.0	3.2	0.8	0.3

5.2.2 Auto-Correlation of the DC Field Measurements

Low-frequency fluctuation. Investigations on periodically low-frequency components of the 6 month observation, from October 2017 to March 2018, are performed. Therefore, the data with the original sample rate are digital low-pass filtered and reduced to 1 min values. Applying the ACF algorithm (5-15) on the very low frequency signal to compare the signal with itself. The results of the ACF are illustrated in Figure 5-3 for all clients. The left picture shows the computation for the 6 month observation period with different linear trends for each client:

- **Client #01** and **#02a** has a constant linear trend around $r_{xx} = 0$
- **Client #03** and **#04** has a constant, increasing linear trend
- **Client #05** shows first an increasing trend, after some days the increase stops to a roughly constant level and finally again increases to $\tau = 0$

An increasing or decreasing trend in the ACF plot indicates a positive or negative DC component in the signal. However, noticeable are that all clients have significant peaks at the same time, which daily repeat. Selecting any arbitrary 2 days observations and zoom in to visualise the daily peaks in more detail, which is illustrated in the right picture of Figure 5-3. Besides the high significant peaks with 1 day period, there tend to be additional minor peaks during the day. The same daily pattern can be observed on any chosen section from the ACF plot.

It should be mentioned, that the Figure 5-3 is limited in the ordinate between values of $r_{XX} = -0.2 \dots 0.8$ because of a better resolution of the plot. Not shown in the figure is the trivial case of $\tau = 0$, where the ACF of each client has the value of one. Lower values than $r_{XX} = -0.2$ do not exist for that ACF observation period.

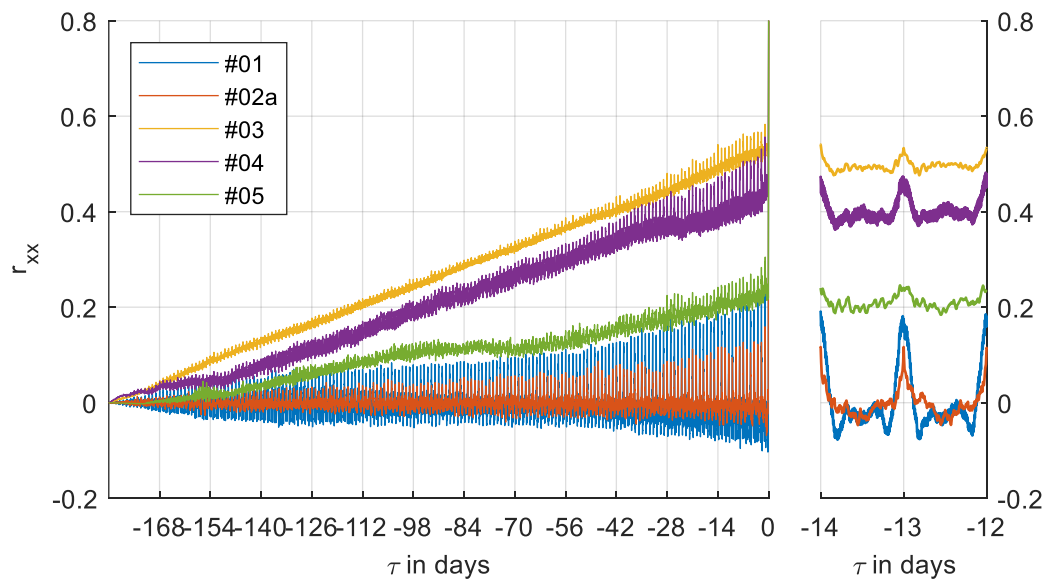


Figure 5-3 Single-sided auto-correlation (ACF) of the low-pass filtered and reduced transformer neutral current (1 min samples) for all clients during the 6 month observation period from October 2017 to March 2018 – left plot. Right picture shows in detail the ACF for any two days.

5.2.3 Fourier Transform of the Measurements

For the spectrum analysis, the investigated frequency range is limited according to the assumption in subchapter 2.2 for relevant GIC frequencies. So the investigated spectrum is within the range of 10^{-5} Hz up to 10^{-1} Hz.

5.2.3.1 Transformer Neutral Currents

The next step is to determine which main frequency components occur in the measured transformer neutral currents, which is signified by the ACF, during the 6 month observation time from October 2017 to March 2018. Applying the FFT on the measurement data with 1 s sample rate, the frequency spectrum is calculated. The relevant parts of the frequency spectrum are outlined in Figure 5-4 for client #01, with the ordinate limitation is set to 100 mA and the frequency range from 10 μ Hz up to 100 mHz. The first investigated frequency range is from 10 μ Hz up to 50 μ Hz (green area) and represents very long-period signals. Derived from the plot, four significant peaks can be identified at the periods 24 h, 12 h, 8 h and 6 h. The other interesting frequency range is from 1 mHz up to 100 mHz (orange area) and therefore covers signal periods between 16.7 min up to 10 s; meaning focussing on the “higher” frequency components. Notable therefore are the peaks of the 15 min, 5 min and 1 min 15 s period of client #01.

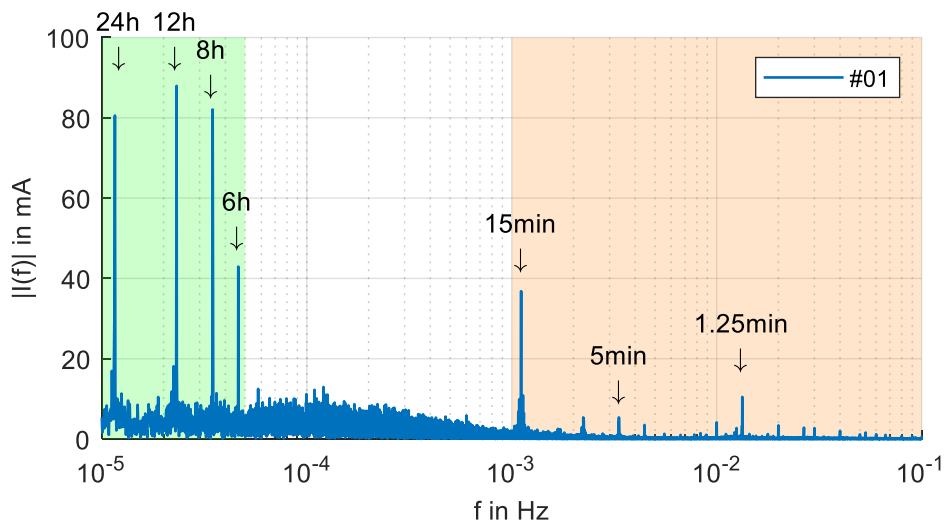


Figure 5-4 Single-sided amplitude spectrum of the measurement of client #01 with 1 s sample rate. Characteristic frequency components in the current are marked in the plots. Observation time from October 2017 to March 2018.

Investigations of the frequency analysis for the above mentioned characteristic periods of all clients are outlined in Table 5-3. The first two rows reflect the absolute magnitudes from the single-sided amplitude spectrum of the DC and 24 h period. Derived from the DC values, client #01 and #02a have a low DC component compared to the 24 h absolute values during observation time, which was also shown in the ACF of Figure 5-3. The zero DC of client #02a is due to the already applied corrective measures for the measurement described at the beginning in subchapter 4.2.5. The subsequent lines in the table refer to relative magnitudes, compared to the 24 h magnitude for each client. It can be seen, that the most relevant frequency components are with the very long periods of hours.

Table 5-3 Characteristic periods with absolute and relative magnitudes from the single-sided amplitude spectrum of all clients during the 6 month observation time from October 2017 to March 2018.

Period	#01	#02a	#03	#04	#05
DC	0.9 mA	1.3 mA	155.9 mA	108.6 mA	140.7 mA
24 h	80.6 mA	22.2 mA	17.9 mA	19.6 mA	37.4 mA
24 h	100.0 %	100.0 %	100.0 %	100.0 %	100.0 %
12 h	109.2 %	49.6 %	132.1 %	158.5 %	63.1 %
8 h	101.9 %	71.5 %	146.0 %	125.7 %	104.3 %
6 h	53.3 %	55.6 %	102.5 %	117.4 %	65.3 %
15 min	45.7 %	3.0 %	18.8 %	136.9 %	13.4 %
7.5 min	4.3 %	6.8 %	7.0 %	39.8 %	2.0 %
5 min	6.7 %	10.3 %	6.4 %	26.8 %	4.7 %
1.25 min	13.0 %	5.8 %	0.6 %	26.6 %	1.6 %

5.2.3.2 Geomagnetic Field

In general, the horizontal geomagnetic field components B_x and B_y have a mean level at 21 000 nT and 1 500 nT. During the observation time in the year 2017, the maximum geomagnetic field variations within minutes were about 15 nT/min for both components. Figure 5-5 outlines the computation results of the spectral analysis for the geomagnetic observation from October 2017 to March 2018 with a 1 s sample rate, where significant frequencies are marked. Four considerable components in the signal, namely the 24 h, 12 h, 8 h and 6 h time period, can be observed from the figure. For the rest of the frequency range, no characteristic peaks are recognised. The green area marks the same frequency range, from 10 μ Hz up to 50 μ Hz, as previously used in Figure 5-4.

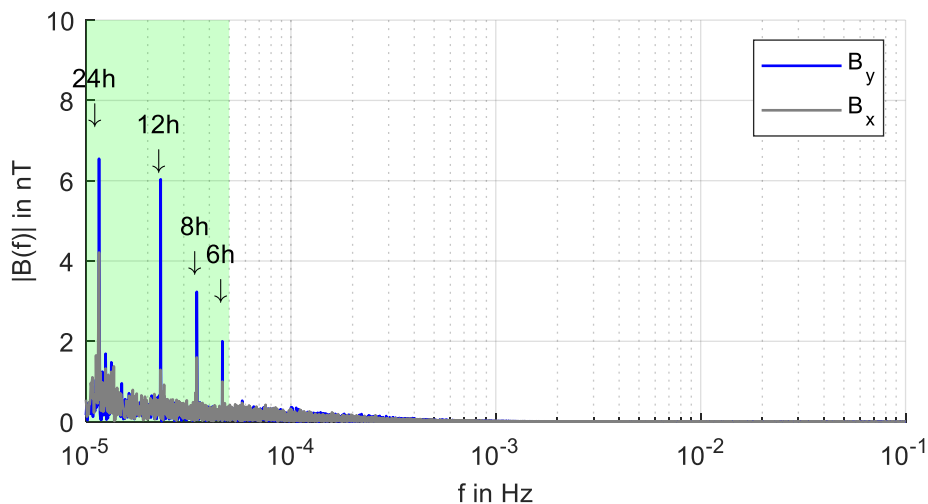


Figure 5-5 Single-sided amplitude spectrum of the horizontal geomagnetic field components during observation from October 2017 to March 2018 with 1 s sample rate. Characteristic frequency components are labelled due to their period.

5.2.3.3 Spectrum Determined by Geomagnetic Activity

In the previous FFT analysis the whole spectrum for a 6 month observation time was computed. This yields to the characteristic long-period signals between 24 h down to 6 h, but all the other frequencies, which may also occur from the geomagnetic field, are reduced to more or less constant noise level. This subchapter considers the frequency spectrum of the transformer neutral current and the geomagnetic field, depending on the geomagnetic activity. The goal is to determine the significant spectrum range of weak and moderate/strong geomagnetic activity besides the already identified long-period components. Therefore, an observation time from 06. – 15. October 2017 with a sample rate of $T_s = 1$ s was chosen. Within this time period, the first five days having a very weak geomagnetic activity, where the K_p index is always in the range below 4-. For the last five days, the activity index was most of the time in the moderate activity range between 4- up to 6+.

The computation of the single-sided spectrum are displayed in Figure 5-6. The upper plot shows the transformer neutral current of client #01 for weak and moderate geomagnetic activities. The plot below refers to the horizontal geomagnetic field B_H for the same weak and moderate days. The horizontal field is chosen because of display clarity reasons.

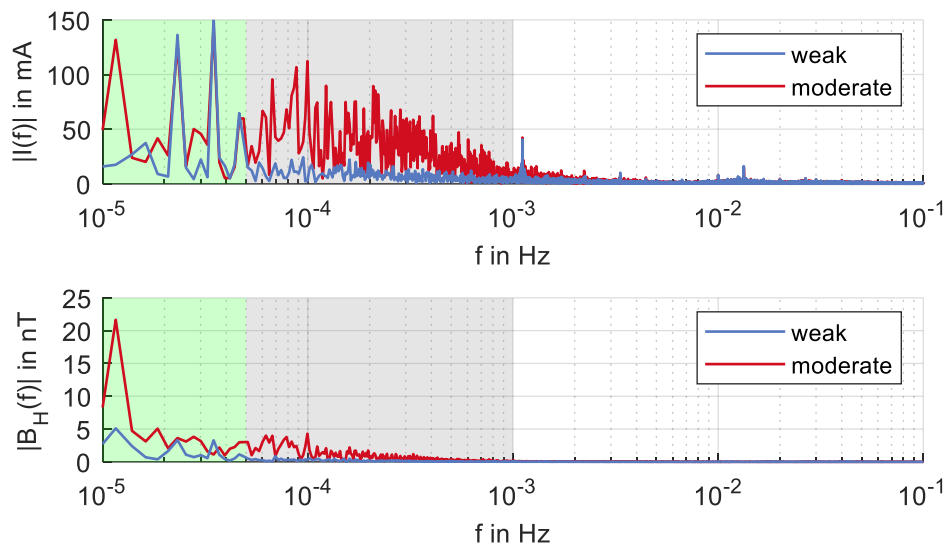


Figure 5-6 Single-sided amplitude spectrum of the 1 s sampled transformer neutral current of client #01 (upper plot) and the horizontal geomagnetic field (bottom plot), determined by the geomagnetic activity. Observation time from 06. – 15. October 2017 with the first five days of weak and the last five days of moderate geomagnetic activity.

Looking on the spectrum of the transformer neutral current in Figure 5-6 (green area), the significant frequencies of the weak days are the same like in Figure 5-4. But the spectrum of the moderate days differs from the weak ones. In this case it is notable, that the frequencies between 50 μ Hz up to 1 mHz (grey area) have been increased compared to the weak days. They are even higher than the already known signals between 24 h down to 6 h periods. The same amplitude-increase within that frequency range could be observed in the horizontal geomagnetic field. This leads to the assumption, that the frequency range between 50 μ Hz up to 1 mHz corresponds to frequencies of higher geomagnetic activities. For frequencies higher than 1 mHz, the amplitudes converge to the same values for weak and moderate days.

5.2.3.4 Conclusion

Based on the frequency analysis of the transformer neutral current and the geomagnetic field, the significant frequency peaks for the 24 h, 12 h, 8 h and 6 h time period can be observed in both. This leads to the conclusion, that especially the very low-frequency components of the currents (may) originate from the geomagnetic field.

The second conclusion of the Fourier transform analysis is, that higher geomagnetic activity seems to cause increased amplitudes within the frequency range from 50 μHz up to 1 mHz in both, the transformer neutral current and the geomagnetic field spectrum.

The higher frequencies above 1 mHz, which emerge only in the transformer neutral measurements, seems to originate from other sources like human impacts. Especially for clients #01 and #04, which are close to Vienna, the spectrum amplitude at, for example, 15 min is conspicuous high and does not exist (or at least not in this extent) in the other clients. Therefore, impacts of centralised telecontrol signals or other (regular) switching operations / clocking of electrical equipment cannot be excluded.

Due to the observations in this analysis, three main frequency ranges in the spectrum can be determined as outlined in Table 5-4.

Table 5-4 Categorisation of the characteristic frequency range from the measurements.

Condition / Source	Frequency Range	Period Range
Weak Geomagnetic Activity	10 μHz ... 50 μHz	27.8 h ... 5.6 h
High Geomagnetic Activity	50 μHz ... 1 mHz	5.6 h ... 16.7 min
Man-made Activity	1 mHz ... 100 mHz	16.7 min ... 10 s

5.3 Root Cause Analysis

5.3.1 Geomagnetic Field Influence

The FFT analysis in the previous subchapter 5.2.3 gives a first indication that the geomagnetic field variation, especially the very low-frequency components, are present in the transformer neutral current too. For visual comparison, the time series of the geomagnetic field of the northward B_x and eastward B_y component and the transformer neutral current, represented by client #01, are displayed in Figure 5-7. The geomagnetic field data are reduced by their mean values to display both components in sufficient resolution in one plot. In the background of the subplot, the 3 h geomagnetic activity index K_p is outlined. For clarity reasons, the values of the K_p indices are hidden and the bar heights are not associated with the ordinate scale; only the colours blue (weak) and green (moderate) as defined in Table 3-2 and Figure 3-1, give information about the index level.

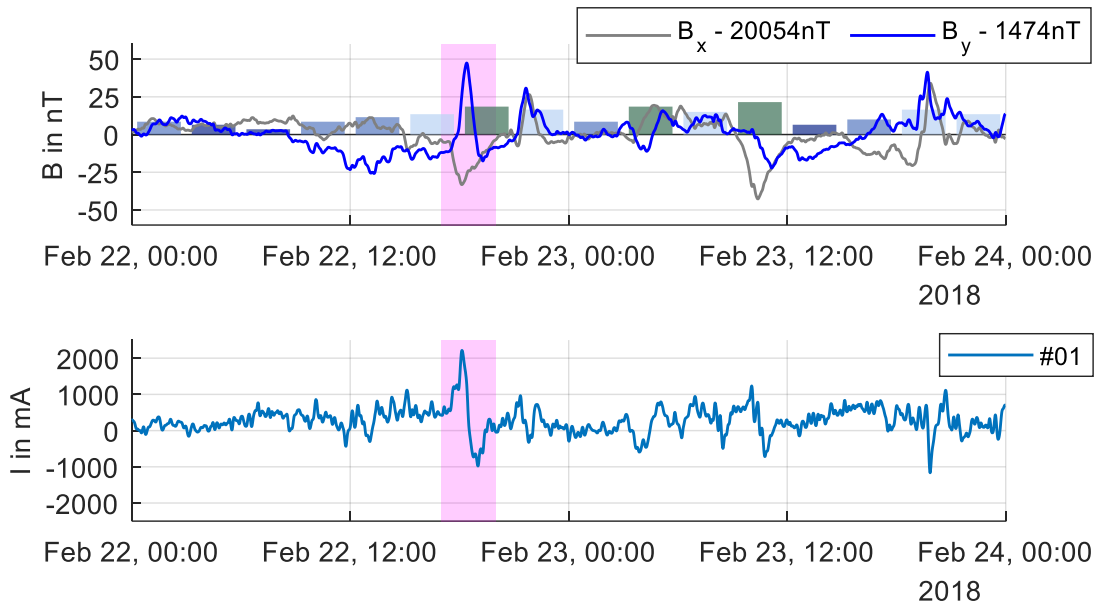


Figure 5-7 Time series of the reduced data (1 min values) of the geomagnetic field and transformer neutral currents during the observation period from 22. – 23. February 2018. Upper plot shows the geomagnetic field components in northward (x) and eastward (y) direction and the lower plot displays the transformer neutral current of client #01. In the background of the upper plot, the colour of the bar plot refers to the geomagnetic activity index K_p .

Comparing the time series of the first day in Figure 5-7 it is conspicuous that both data, the geomagnetic field as well as the transformer neutral current, have no significant low-frequency fluctuations. This is also signified by a weak geomagnetic activity. During the time from 17:00 to 20:00 of the 22. February 2018, which is marked in the figure in magenta, the low-frequency fluctuations of the geomagnetic field sharply increase and decrease after time. These changes are also present in the transformer neutral current, where the current amplitude rises to a positive maximum during observation and subsequent changes to the negative peak. The same visual correlation can be seen during other observation periods, where the geomagnetic activity is higher. Computing the correlation r_{XY} - Table 5-5 - between the geomagnetic field components and measured transformer neutral current of client #01, a mathematical correlation could not be pointed out. The correlation increases by taking the derivation of the data, but is still not that high as first assumed.

Table 5-5 Correlation between the geomagnetic field B_x , B_y and the transformer neutral current of client #01.

r_{XY}	B_x	B_y	$\frac{dB_x}{dt}$	$\frac{dB_y}{dt}$
$I_{\#01}$	-0.23	0.15	-	-
$\frac{dI}{dt}$	-	-	-0.45	-0.44

5.3.2 Human Sources

High-frequency fluctuation. Based on the observations in Figure 5-1, that the high-frequency fluctuations differ on daytime, investigations on the high-frequency components of each client are performed. For this, the raw data with a sample rate of 1 s for a one week observation from 19. to 26. February 2018 is used. On this data, a digitally high-pass filtered with a cut-off frequency of $f_c = 1 \text{ mHz}$ is applied; therefore only higher frequencies occur in the investigated signal. In a next step, the root-mean-square value I_{RMS} , or effective value, for each time interval $\Delta t = 300 \text{ s}$ of the high-pass filtered signal is calculated and plotted in Figure 5-8.

Focussing on the upper plot in Figure 5-8 it can be seen, that the I_{RMS} value significantly differs on time and day. For example on client #01 working days, the I_{RMS} value in the early morning hours is close to zero; than the rest of the day with values about 100 mA. Only on the weekend days, the fluctuation range within seconds in the morning hours is not zero and reaches values close to the rest of the day. The effective-value-pattern of clients #02a and #04 are similar to #01 and differs only in the magnitude in the non-morning hours.

Looking at client #05, the RMS-value also varies during daytimes, especially in the early morning hours the value is also close to zero. But the rest of the daytime, the effective value has no constant level like client #01. It seems more an increasing and decreasing cycle with the peak value around midday.

Another different behaviour shows client #03, where the I_{RMS} -value is more or less at a constant level of about 10 mA.

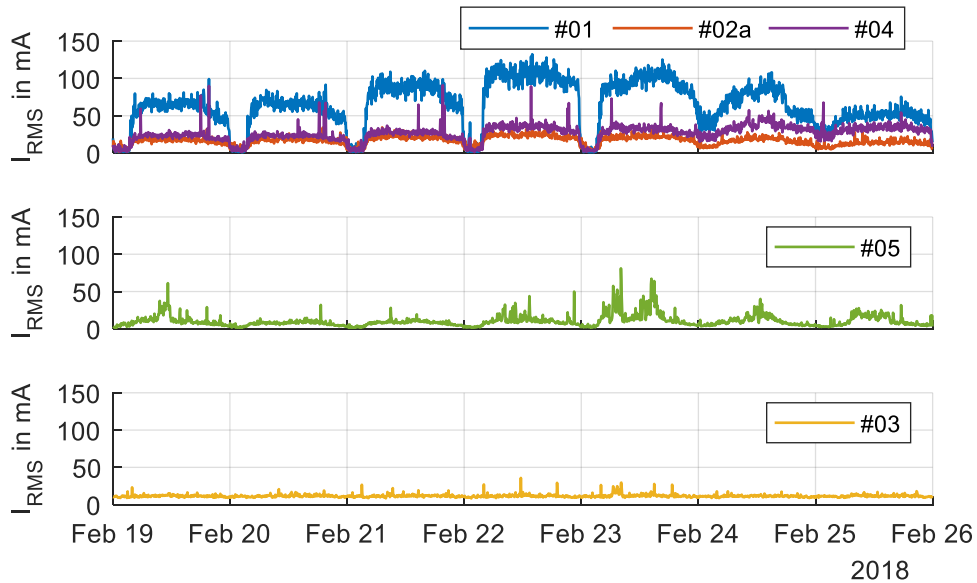


Figure 5-8 RMS-values of the digitally high-pass filtered signal of all clients with $f_c = 1 \text{ mHz}$, based on the original sample rate of 1 s. One week observation time from 19. – 26. February 2018.

Comparing the observations with the location of the measurements in Figure 4-4 it is conspicuous, that the measurements with high RMS-values of the high-pass filtered currents, especially clients #01 and #04 are close to the capital of Austria. Also client #02a has a transmission line which is directly connected to the substation, where client #01 and #04 are installed. It seems that the pattern of the three clients originate from any human source, because of the daily rhythm for working days; and another equally signal path for weekend days or holidays. It turned out, that

the operation time of the public transport system like⁵ underground train system of the town coincides with the rise of RMS-values of the fluctuations. From the time schedule of the underground operator can be seen, that in the early morning hours on working days, there is no operation of the undergrounds between midnight and 05:00 am. On weekend days and holidays, the operation time is 24 hours a day. The underground operation is reflected in the transformer neutral measurements, because they are using a DC supply system, which can also enter the power transmission grid via the direct-grounded transformer neutral. Although the client #02a is more than 150 km of distance of the underground, the DC coupling of the underground operation system can also be measured in this substation.

However, a similar pattern profile is outlined for client #05. While the RMS-values also tend to have minimums in the morning hours, this is not as significant as for the previous discussed clients. Additionally, the early RMS-values did not differ between working days or weekends. But again looking at the geographical location of the substation, with approximately 50 km to Salzburg or 100 km to Munich, it seems, that also the DC public transport system from that towns can enter the power transmission network.

A classification of the RMS-values of client #03 is difficult due to the low and roughly constant fluctuation level.

5.3.3 Photoelectric Effect

A less daily DC offset was observed from the measurements of all clients. As a response to explain the daily offset, considerations of different potentials at the substations caused by the solar radiation of the sun are performed, according to the photoelectric effect [98]: when energetic photons impinge on (metals) matter, this causes an emission of electrons. This effect is used in modern technology like the solar panels. Derived from that theory, there may be similar effects on overhead lines, substation groundings or the soil between two grounding points, which changes the (earth) potentials.

The idea is to focus on sunny and cloudy days during the measurement observation time and afterwards contrast both days with the recordings. Therefore data of the global solar radiation⁶ (GSR) is used, which describes the radiation on a horizontal surface on Earth. The GSR is composed by the sum of direct and diffuse radiation measurements which can be reduced by reflexion on atmosphere, absorption of atmosphere, the Rayleigh- or Mie-diffusion [99]. Clouds generally cause decreasing GSR and therefore low or high GSR values are used to indicate cloudy or sunny days.

Based on the 10 minute GSR sample data between June to September 2017, the daily GSR energy is calculated from an GSR-measurement station close to Vienna. The daily time series are plotted in Figure 5-9 on the left upper picture. For a better overview, the right upper plot shows the GSR in ascending order. It can be seen, that there are days with very low daily GSR (cloudy days) between 1 kWh/m² to 4 kWh/m² and days with high daily GSR (sunny days) up to 8 kWh/m².

For the DC-offset-research, 10 days of the sunniest and cloudiest days during the 3 month observation are taken into account as marked in the upper right. Indicate these extreme days, the daily measurements of client #01 are compared between sunny and cloudy days by calculating their daily mean values, as shown in the bottom plot of Figure 5-9. Marked in the same plot is the area from morning to afternoon hours (in yellow). During that time, the daily mean measurements

⁵ Public timetable of Wiener Linien [97]

⁶ Data from the ZAMG

show no significant differences as they may be expected. The same observation was made by the other clients.

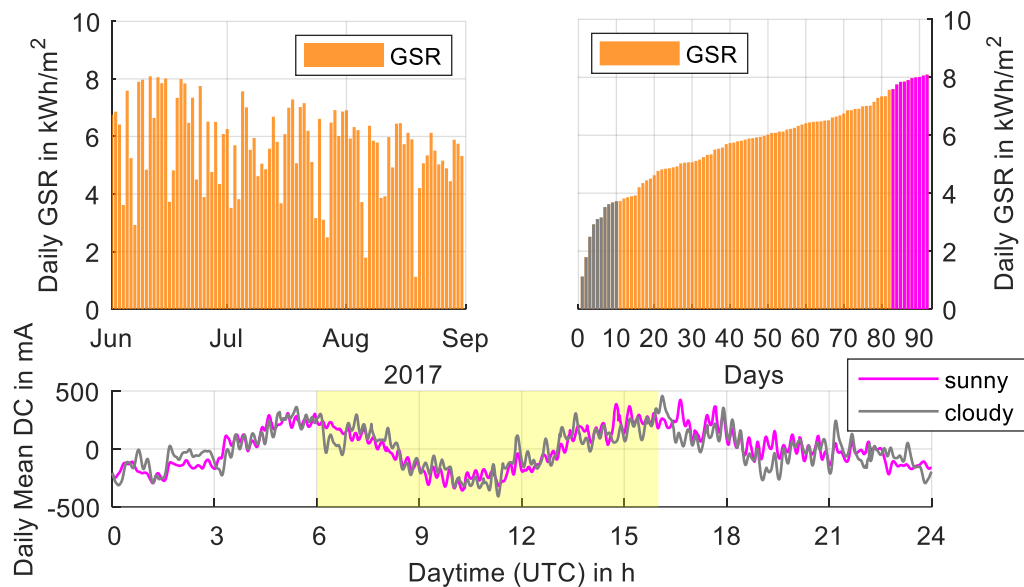


Figure 5-9 Daily mean values of the global solar radiation compared to the DC measurement of client #01. The left upper plot shows the time series and the right upper one the GSR in ascending order. The bottom plot indicates the daily mean values of the 10 sunniest (pink) and cloudiest (grey) days.

5.4 Summary

Based on the transformer neutral current measurement analysis, DC characteristics can be formulated to transformer exposure:

- **Low-frequency fluctuations from geomagnetic activity**
Slow-fluctuations derived in the range of minutes to hours, $\Delta t = \text{minutes} \dots \text{hours}$
 - Normal geomagnetic activity: 10 μHz ... 50 μHz
 - Higher geomagnetic activity: 50 μHz ... 1 mHz
- **High-frequency fluctuations from man-made activity**
Fast-fluctuations derived in the range of seconds, $\Delta t = 1 \text{ s}$
- **Low DC amplitudes**
Like a constant DC offset, which is present most of the time

The short peaks can lead to negative effects on voltage and system stability, the permanent low DC amplitudes have to be considered according to the higher noise level of the transformer. The ECDF plot of all clients in Figure 5-2 indicates, that about 98 % - 99 % of the 6 month recording, the transformer neutral current is below 1 A, meaning that the transformer exposure to DC for that period is not as high and therefore the risk of half-cycle saturation is low. But the key factor is, that there is a potential risk of 39 h for client #01 and respectively 70 h for client #05 left, where higher DC and therefore negative effects on transformers may occur. Especially for clients #01 and #05, the maxima current peak values and durations are higher, compared to the other clients.

The low-frequency components in the transformer neutral current, especially the 24 h, 12 h, 8 h and 6 h periods are significant in the frequency spectrum, daily occur on all clients and seems to be independent on human influence. The same periods are identified in the geomagnetic field spectrum, so it seems to be a “visual” correlation between them, although the cross-correlation coefficient is low. The peaks in the current spectrum between the range of 1 mHz up to 100 mHz may originate from human impacts like periodically telecontrol signals.

In contrast, the high-frequency components can be associated to human technology like the public transport DC operating system. Considering, that some neighbouring railway systems or undergrounds to Austria also operate with DC systems, substations close to those countries or cities may also exposure to those higher fluctuations.

Effects, like the photoelectric effect, on the DC offset from the solar radiation between cloudy and sunny days could not be confirmed by the DC measurements. Other reason for the DC offset could be an electrochemically process between the substations grounding materials, which may cause potential differences and leading to the DC offset.

6 GIC SIMULATION METHOD AND ANALYSIS

6.1 Introduction

One of the first investigations about telluric currents in the earth are done by [100], [101], which describe the relationship between the Earth's magnetic field and telluric currents. Based on the magnetotelluric method, subsequent work on GIC for example [10], [102], [103] are established. To calculate the electromagnetic induction in the earth and the magnetic and electric fields on the surface, two main methods are used for the primary ionospheric and magnetospheric current systems. The fundamental approximations of the magnetic sources are as a

- plane-wave or
- line currents.

Both simplifications can be used to compute in real-time the geoelectric field at the surface by using the earth conductivity structure, but considerations about their approach should be done. The plane-wave method is suggested to be sufficient for GIC analysis for mid-latitude regions such as Central Europe [73], because the field-aligned current system in vertical direction has a lower influence, compared to the horizontal field components. Making the assumption, especially for small countries, that the magnetic field disturbances are uniform across the investigated plane surface; leading further to the plane-wave method. Therefore, a single measurement point of the geomagnetic data from observatory is sufficient to represent the geomagnetic field distribution. For other regions closer to the magnetic poles, the plane-wave is not an appropriate method to represent the geomagnetic field conditions, with the closer concentration of vertical field-aligned currents [67].

Plane-wave method. The plane-wave method is one of the simplest methods to compute the induced currents in the earth. The theory describes a primary electromagnetic field originates from the ionospheric current system, which propagates vertically downward as a plane-wave to the surface. Depending on the earth conductivity structure, the geoelectric field is calculated by multiplying the magnetic fields by the transfer function of the earth. This method is discussed and outlined in detail in the subchapter 6.2.

CIM method. The complex-image method (CIM) with line current approximation is an adequate approach for geoelectric field calculations at higher latitudes. To point out the difference between the plane-wave and the CIM method, the CIM method is briefly introduced, but it is not applied for this research. The line current approach approximates the primary source for the magnetic and electric fields, the auroral electrojet, as an infinity line current above the surface at height of about 100 km. To calculate the magnetic and electric fields at the surface from the line current, the CIM method images the induced currents within the Earth at a complex depth and afterward computes the fields of both line currents.

To determine the primary ionospheric current system, the spherical elementary current system method [104] can be used based on ground geomagnetic observatory data. To represent a more realistic auroral electrojet with a specific width (like a sheet current), multiple line currents are used. A detail explanation of the CIM method used for geoelectric field calculations is given in [67], [105], [106], [106], [107]. [14]

Generally, the GIC simulation technique can be classified into two main steps:

- **Geophysical Model**
The geophysical model deals with the computation of the horizontal geoelectric field from the magnetic source and earth conductivity structure.
- **Power System Model**
The power system model includes the calculation of the currents flowing in the technological systems like power grid or pipelines, driven by the geoelectric field.

A benefit of the classification is, that the two parts can be modelled independently of each other, which makes it simpler to compute and analyse. The independence of both steps is argued in [9] by neglecting the inductive coupling between the Earth and the human technology system. This can be justified due to the very low GIC frequency wide below 1 Hz.

An overview of the principal computation is given in the method flow chart in Figure 6-1. It shows the input parameters, which are necessary for simulation, and visualises the essential computation steps. Data of the magnetic field and the earth conductivity structure are used in the geophysical model to calculate the geoelectric field in frequency domain. Afterwards the third input parameter, the grid model, is necessary to calculate the geomagnetically induced currents driven by the geoelectric field. Outcomes of the simulation model are the GIC, which are distributed over the transmission grid like lines, transformer windings and substation groundings. Firstly, the expected DC exposure to transformer can be estimated with simulations, and secondly, the simulations can be evaluated by the measurements in the transformer neutral. The applied input parameters are discussed in detail in the following subchapters.

However, generally the induced *emf* are generally higher for lines parallel to the latitudes than for longitudes [108].

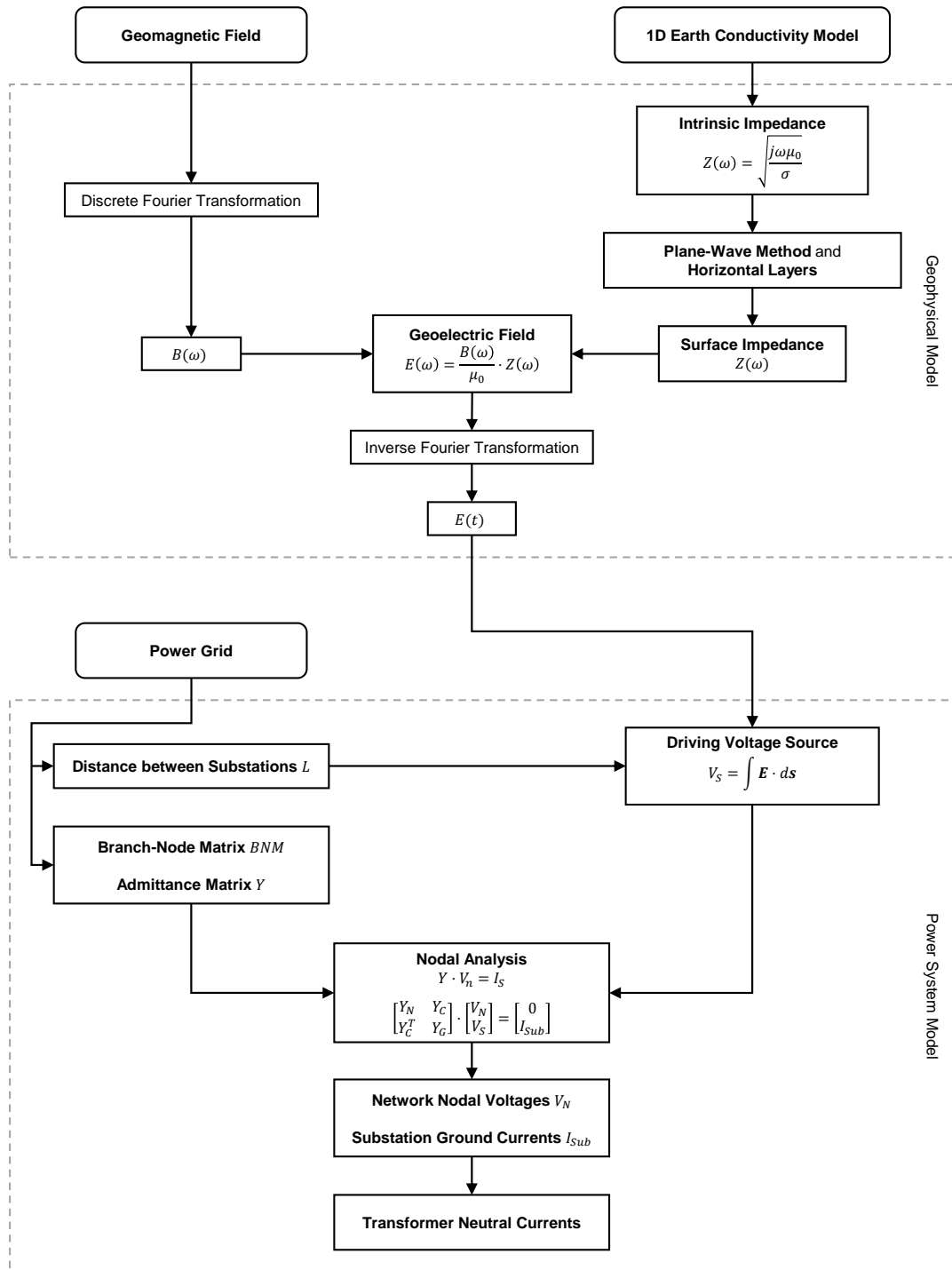


Figure 6-1 Method flow chart of the GIC simulation method.

6.2 Geophysical Model

6.2.1 General on Electromagnetic Fields for Geomagnetic Induction

Basis for GIC modelling and the applied plane-wave method are the Maxwell's equations, material relationships and the assumed boundary conditions for computation. For local geomagnetic induction studies it is reasonable to assume an infinite plane surface as the boundary between two half-spaces. One half-space is the air and the other half-space is the soil. For the following deductions, it is assumed, that the half-space of the earth is homogeneous and isotropic.

A brief review of the common fundamentals in classical electromagnetic theory, especially for geomagnetic induction are outlined in the following lines with the field vectors marked in bold. Starting with the well-known Maxwell's equations in (6-1),

$$\begin{aligned}
 \text{I. } \nabla \times \mathbf{B} &= \mu \mathbf{J} + \mu \varepsilon \frac{\partial \mathbf{E}}{\partial t} \\
 \text{II. } \nabla \times \mathbf{E} &= -\frac{\partial \mathbf{B}}{\partial t} \\
 \text{III. } \nabla \cdot \mathbf{E} &= \frac{\rho}{\varepsilon} \\
 \text{IV. } \nabla \cdot \mathbf{B} &= 0
 \end{aligned} \tag{6-1}$$

\mathbf{B}	magnetic field, $\left[T = \frac{Vs}{m^2}\right]$
\mathbf{E}	electric field, $\left[\frac{V}{m}\right]$
\mathbf{J}	electric current density, $\left[\frac{A}{m^2}\right]$
μ	magnetic permeability, $\left[\frac{Vs}{Am}\right]$
ε	electric permittivity, $\left[\frac{As}{Vm}\right]$
ρ	charge density per unit volume, $\left[\frac{As}{m^3}\right]$

the first expression describes the generalised Ampere's law, following by Faraday's induction law as second, third is the Gauss law and the last outlines the source-free of the magnetic flux density. The Ohm's law is quoted in (6-2)

$$\mathbf{J} = \sigma \mathbf{E} \tag{6-2}$$

σ	conductivity, $\left[\frac{1}{\Omega m}\right]$
----------	---

and constitutional (material) relationships gives (6-3) with scalar quantities if the media is isotropic.

$$\mathbf{D} = \varepsilon_r \varepsilon_0 \mathbf{E} = \varepsilon \mathbf{E} \quad (6-3)$$

$$\mathbf{B} = \mu_r \mu_0 \mathbf{H} = \mu \mathbf{H}$$

\mathbf{H}	magnetic field strength, $\left[\frac{A}{m}\right]$
\mathbf{D}	electric field strength, $\left[\frac{As}{m^2}\right]$
ε_r	relative electric permittivity, $\left[\frac{As}{Vm}\right]$
ε_0	electric permittivity of the free-space, $\varepsilon_0 = 8.85 \cdot 10^{-12} \frac{As}{Vm}$
μ_r	relative magnetic permeability
μ_0	magnetic permeability of the free-space, $\mu_0 = 4\pi \cdot 10^{-7} \frac{Vs}{Am}$

A common practice in geomagnetic induction studies is to simplify Maxwell's equation to the quasi-static field formulations by using following assumptions [9], [103], [109], [110]:

- The media is assumed to be non-magnetic and therefore the relative magnetic permeability is set to $\mu_r \approx 1$
- The sources are outside of the observation area and therefore no free charge carrier exist $\rho = 0$
- The displacement current can be neglected due to the facts, that the electric permittivity is close to the free-space value ε_0 and the frequencies $f < 1 \text{ Hz}$ and conductivities $\sigma > 10^{-5} \frac{1}{\Omega m}$ of geomagnetic induction ensures $|\mathbf{J}| \gg \left| \varepsilon \frac{\partial \mathbf{E}}{\partial t} \right|$

Applying the formulated assumptions on the fundamental equations in (6-1), leading to the quasi-stationary approximation of Maxwell's equations as quoted in (6-4).

$$\begin{aligned} \text{I. } \nabla \times \mathbf{B} &= \mu_0 \sigma \mathbf{E} \\ \text{II. } \nabla \times \mathbf{E} &= -\frac{\partial \mathbf{B}}{\partial t} \\ \text{III. } \nabla \cdot \mathbf{E} &= 0 \\ \text{IV. } \nabla \cdot \mathbf{B} &= 0 \end{aligned} \quad (6-4)$$

Important from the assumptions is, that the divergence of the first equation from (6-4) leading to $\nabla \cdot (\nabla \times \mathbf{B}) = 0$ and therefore $\nabla \cdot \mathbf{J} = 0$, meaning that the current in the earth is solenoidal. Derived from the solenoidal \mathbf{J} and assuming no horizontal variations within the half-space, the boundary condition for the current density are given in (6-5) by applying Gauss' theorem

$$\sigma_1 \mathbf{E}_{1n} = \sigma_2 \mathbf{E}_{2n} \quad (6-5)$$

$\mathbf{E}_{1n}, \mathbf{E}_{2n}$ vertical component of electric field to cross-section, $\left[\frac{V}{m}\right]$

Assuming the conductivity of the air is zero, the vertical electric field component inside the earth is zero too. This means that only horizontal electric field components exist and those tangential components are continuous on boundaries. [9]

Taking the curl of the second expression from (6-4) and additionally using the first expression, gives the diffusion equation (6-6) for the electric field.

$$\begin{aligned}\nabla \times (\nabla \times \mathbf{E}) &= \nabla \times \left(-\frac{\partial \mathbf{B}}{\partial t} \right) \\ \nabla^2 \cdot \mathbf{E} &= \mu_0 \sigma \frac{\partial \mathbf{E}}{\partial t}\end{aligned}\tag{6-6}$$

In contrast to electromagnetic waves, the formula of the electric field describes more a diffusion in the medium than a propagation. The same diffusion formula for the magnetic field (6-7) can be obtained by taking the curl of expression I. in (6-4).

$$\nabla^2 \cdot \mathbf{B} = \mu_0 \sigma \frac{\partial \mathbf{B}}{\partial t}\tag{6-7}$$

At this point, the derivation and solution of the diffusion equations (6-6) and (6-7) are renounced and therefore referred to literature for example [111].

6.2.2 Earth Conductivity Model

6.2.2.1 General

One of the most sensitive parameter for geoelectric field computations, and therefore GIC simulations, is the earth distribution structure and their conductivities. According to the applied earth structure, differences in complexity, accuracy and computation time for geoelectric field calculations occur. Following earth conductivity models can be defined hereafter, as pointed out in [112].

1D-model. This model treats only with conductivity variations in one dimension, the z-direction (vertically downward), whereas the expansion of the horizontal directions goes to infinity and have no conductivity variations, so they are laterally homogeneous. The earth conductivity in the simplest case can be assumed as a homogeneous half-space with the conductivity σ . In this case there is no reflected wave within the earth and the earth impedance can be calculated by formula (6.9). A further expansion for this model is the 1D-layered earth model, where the earth half-space is divided into N layers in z-direction with conductivity σ_n and thickness d_n for each layer n . The characteristic surface impedance can be calculated as already explained by the plane-wave method in subchapter 6.2.2. The 1D-layered earth conductivity model is used for this thesis.

2D-model. A more complex approximation of the earth distribution is the 2D-model, which variations are in z-direction and one of the horizontal component. This is a common method for investigations along coastlines. However, due to the complex earth structure, numerical solution approaches are common for the 2D-model such as finite difference method, finite element method or integral equation method.

3D-model. The most realistic image of the earth conductivity structure gives the 3D-model which considers the inhomogeneous conductivities in all three dimensions. Generally, the 3D-model also requires a numerical method and the same solution approaches as mentioned for the 2D-model. This model provides the highest accuracy with the drawback of higher computation time.

6.2.2.2 EURISGIC Data

For this thesis, the 1D-layered earth conductivity model is applied for the geophysical model. Studies of the European lithosphere and 1D-model are performed by the EURISGIC WP2 project [76], [77]. The published data are results of the deep magnetotelluric sounding measurements, to determine the layers conductivities. Due to the various geological and topographical conditions within a country, Europe was divided into a grid of segments where each block dimension is about $200 \text{ km} \times 200 \text{ km}$. However, larger countries can include several cells where each segment is

numbered to identify the specific earth distribution. Further outlined in the research is a conductance map of Europe for the upper 80 km and 160 km of lithosphere as shown in Figure 6-2. It can be seen from the figure, that especially for Alp regions, the resistivity is higher compared to the rest of Central Europe.

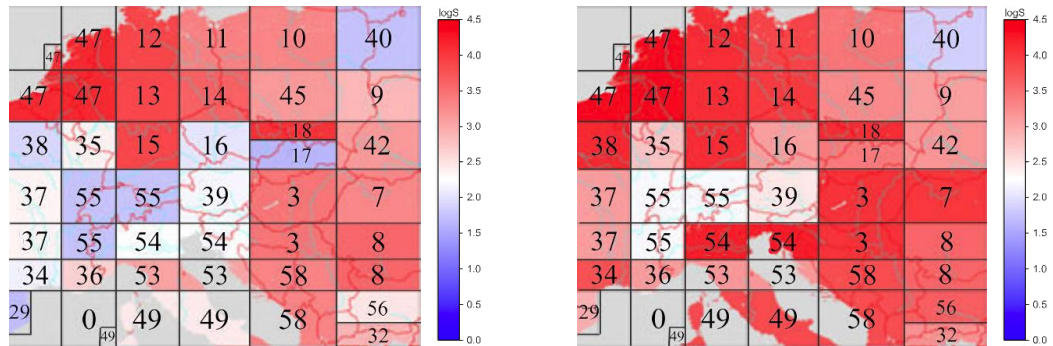


Figure 6-2 Conductance map of Central Europe for the upper 80 km on the left and the upper 160 km on the right. (picture section taken from [76])

Specific for Austria is that the neighbouring cells in the east and south show an abrupt change in the conductivity value; so there is no smooth crossover between the blocks which may cause significant geoelectric boundary conditions. Two cells are characteristic of the earth conductivity structure of Austria referred to [76]:

- **model #39** indicates to mountainous and valleys in the east and
- **model #55** refers to high-Alpine (mountainous) regions for example the Alps in the west.

Both models are applied for this research and the parameters are outlined in (6-1). It can be derived from the table, that the conductivities of model #39 for the upper 100 km are lower than for model #55 (apart from the first 2 km). Noticeable is for the half-space of model #39 and the third layer of model #55, that they show one of the highest resistivity values that occur, compared to the other layers for Europe.

Table 6-1: Parameters of the 1D-layered earth conductivity model from the EURISGIC WP2 project. [76], [113]

Earth layer n	<i>Model #39</i>		<i>Model #55</i>	
	Thickness <i>d</i> in km	Conductivity σ in 1/ Ω m	Thickness <i>d</i> in km	Conductivity σ in 1/ Ω m
1	55	1/1 000	0.9	1/110
2	45	1/300	1.1	1/30
3	half space	1/1 000	150	1/10 000
4	-	-	half space	1/90

6.2.3 Plane-wave Method

Firstly, the geographic coordinates to describe the fields are defined as x for northward, y for eastward and z for vertically downward directions. The ionospheric and magnetospheric sources are assumed as an infinite horizontal current sheet above the earth surface. Originating from that current sheet, a primary electromagnetic field propagates vertically downward as a plane-wave with harmonic time-dependence to the earth's surface. The electromagnetic behaviour of the air is assumed like the free-space conditions μ_0 and ϵ_0 with zero conductivity $\sigma = 0$. The earth's surface lays in the horizontal xy -plane at $z = 0$ with the extension goes to infinity. Further the earth structure below the surface is assumed to have horizontally layers with thickness d and conductivity σ . Each layer is supposed to be linear, homogeneous and isotropic which means a uniform layer conductivity. There are no horizontal variations within the earth layers. [103]

The basic formulation about the plane-wave method and layered earth conditions, especially for magnetotelluric investigations, are formulated by [100], [101]. The following formulations are in frequency domain and deal with the total earth impedance $Z(\omega)$ as function of the angular frequency ω , calculated from the transmitted and reflected waves due to the wave diffusion in the earth. The total earth impedance (also referred as surface impedance) characterise the relation between the magnetic and electric fields with the frequencies obtained from the geomagnetic field observations. After the total earth impedance is computed, the geoelectric field can be derived from the impedance and geomagnetic fields in accordance reordering equation (6.8)

$$Z(\omega) = \frac{E(\omega)}{H(\omega)} \quad (6.8)$$

Z total earth impedance, [Ω]
 ω angular frequency, [Hz]

To get the total earth impedance, the method starts by calculating the impedance $Z_m(\omega)$ of the half-space bottom layer quoted by (6.9).

$$Z_m(\omega) = \sqrt{\frac{j\omega\mu_0}{\sigma_m}} \quad (6.9)$$

Z_m earth impedance of the bottom layer m , [Ω]

After the intrinsic impedance Z_m is calculated from the bottom layer m , the subsequent steps (given in [114]) are formulated using Snell's law to calculate the earth impedance of layers above the bottom layer up to the surface impedance by considering transmitted and reflected waves. Following formulations for layers $n = m, m - 1, \dots, 1$ are quoted therefore from (6.10) to (6.14).

$$Z_n(\omega) = \frac{1 + \alpha_n(\omega)}{1 - \alpha_n(\omega)} \cdot Z_{0n}(\omega) \quad (6.10)$$

$$\alpha_n(\omega) = r_{n+1}(\omega) \cdot e^{-2\gamma_n(\omega)d_n} \quad (6.11)$$

$$r_{n+1}(\omega) = \frac{Z_{n+1}(\omega) - Z_{0n}(\omega)}{Z_{n+1}(\omega) + Z_{0n}(\omega)} \quad (6.12)$$

$$\gamma_n(\omega) = \sqrt{j\omega\mu\sigma_n} \quad (6.13)$$

$$Z_{0n}(\omega) = \sqrt{\frac{j\omega\mu_0}{\sigma_n}} \quad (6.14)$$

Z_n	impedance of layer n , [Ω]
Z_{0n}	intrinsic impedance of layer n , [Ω]
α_n	reflexion coefficient
r_{n+1}	reflexion coefficient
γ_n	propagation constant of layer n
d_n	thickness of layer n , [m]
σ_n	conductivity of layer n , [$\frac{1}{\Omega m}$]

After the surface impedance $Z(\omega)$ is known, reordering formula (6.8) leads to the geoelectric field formulations in northward and eastward direction as quoted in (6.15) - (6.16). Thereafter the electric fields in frequency domain are converted into time series values $E(t)$ using the inverse FFT. The geoelectric fields E_x and E_y are afterwards implemented in the power grid model as the driving sources of GIC.

$$E_x(\omega) = \frac{Z(\omega)}{\mu_0} \cdot B_y(\omega) \quad (6.15)$$

$$E_y(\omega) = -\frac{Z(\omega)}{\mu_0} \cdot B_x(\omega) \quad (6.16)$$

E_x, E_y	northward and eastward geoelectric field, [$\frac{V}{m}$]
B_x, B_y	northward and eastward geomagnetic field, [T]

However, the deepness of the plane-wave penetration δ in the earth depends general on the angular frequency ω , the magnetic permeability μ and the conductivity σ as quoted by formula (6.17). The penetration depth δ represents a decrease of the initial value to $\frac{1}{e} \approx 37\%$. Due to the characteristic properties in geo-electromagnetic induction as described previous, the wave penetrates hundreds of km into the earth.

$$\delta = \sqrt{\frac{2}{\omega\mu\sigma}} \quad (6.17)$$

δ	penetration depth, [m]
----------	------------------------

6.3 Power System Model

6.3.1 Fundamentals in GIC Driving Source Implementation

Many studies were performed during the last years about GIC induction in network systems. Therefore, it is essential to understand the general GIC phenomena and determine the driving source for GIC in the transmission network and how it can be modelled for GIC simulations. [14], [115] pointed out the common misunderstandings of GIC driving sources and implementation in simulation models. Figure 6-3 illustrates the common misinterpretation of GIC and outlines the correct implementation of the driving GIC source in the network.

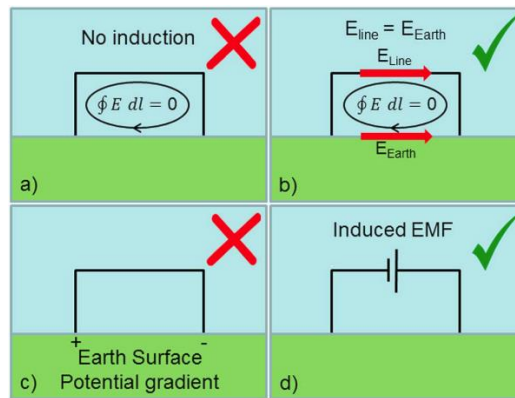


Figure 6-3 Geomagnetic induction in a network and the common misinterpretation of GIC driving source. The incorrect application gives plot (a) and (c), the correct utilisation outlines (b) and (d). Picture taken from [14].

Defined by Faraday's law of induction, any time-varying magnetic field causes an electric field. Applying the law on a conductive closed loop, any change of the magnetic flux will cause an electromotive force that drives a current. For example, a loop is formed by a transmission line, transformer groundings and the Earth's surface. The change of the magnetic flux through this area is too small to induce significant voltage levels that drive the GIC, even if the transmission line is 200 km long with a mean altitude of 30 m, as illustrates Figure 6-3 (a). Instead, the relevant induction area has to be extended from the transmission line downwards into the earth [108], [109], [115]. Now the zero integral between the line and the surface shows, that the electric fields from soil and in the lines have the same direction and magnitude - Figure 6-3 (b). [14]

Another aspect is the correct implementation of the *emf* as a driving source. The induction of the *emf* in the earth leading to the confusion, that the driving source for GIC in the lines can be seen as surface potential gradients between two groundings, as outlines Figure 6-3 (c). The application of surface potentials is only correct for a uniform electric field assumption, but incorrect due to realistic electric fields. However, the current in the soil is purely driven by the induced *emf* and therefore no potential gradients at the surface exist. Due to that, the GIC driving voltage source has to be computed in series with the line - Figure 6-3 (d). [14]

How to implement the geoelectric field in the network model to compute the GIC depends on which approach is chosen on the nature of the geoelectric fields. Realistic fields, originating from the auroral electrojet, are non-uniform and assumed to be zero at infinity. The electrojet is simulated as a time-varying line current at a specific high above the Earth surface, from that the electric field is produced. The electric field is stronger underneath the line current and decreases with distance to the source and can be computed for instance by the complex image method [103],

[106], [107]. The correct way to implement this electric field to GIC modelling is by a voltage source in series with the transmission lines. [13], [116]

Uniform electric fields. In contrast to the realistic field, a uniform electric field characterise other properties and simplifies the GIC modelling. The uniform field is assumed not to be zero at infinity, but the conditions of being free of curl and divergence are both satisfied. Thus the uniform field represents both, an irrotational and a solenoidal field. Satisfying Laplace's equation for a source-free region, the field can be seen as a scalar potential. [116]

In case of the conservative scalar potential, the uniform homogeneous electric field can be modelled as voltage sources in series with transmission lines or between grounding points [116]. Due to the fact of the homogeneous geoelectric field within the investigated area, the voltage difference V_{21} can be computed between two points P_1 and P_2 as given in (6.18) which is well-known in electrical engineering theory.

$$V_{21} = - \int_{P_1}^{P_2} \mathbf{E} \cdot d\mathbf{s} = V_2 - V_1 \quad (6.18)$$

V_{21} voltage between points P_1 and P_2 , [V]
 V_1, V_2 potential of P_1 and P_2 , [V]

According to equation (6.18) the driving voltage source V_S between two grounding points i and j of the substations from the isotropic, homogeneous geoelectric field \mathbf{E} can be formulated as given in (6.19). So the driving source can be simply calculated from the horizontal geoelectric field components E_x, E_y and the corresponding distances L_x, L_y between two substations.

$$V_S = \int_i^j \mathbf{E} \cdot d\mathbf{s} = E_x \cdot L_x + E_y \cdot L_y \quad (6.19)$$

V_S driving voltage source, [V]
 L_x, L_y distance between substations in northward and eastward direction, [km]

6.3.2 Power Network Model

As can be seen from formula (6.19), a major contribution from the network topology to the driving voltage source are distances between the direct-grounded neutral of transformers. Therefore, the investigated power network model primary covers the high and extra-high-voltage transmission grid with the long transmission distances. Due to the neutral point treatment of the medium-voltage level in Austria, which are (commonly) isolated to the ground, they can be neglected for GIC analysis. Another operation mode of the medium-voltage power system is compensated via Petersen coil in the transformer neutral, which provides on the one hand, a high conductance to DC but on the other hand, the distance between two groundings of this voltage level is too low to drive significant GIC. The same argument on distance holds on the low-voltage level, which also uses direct-grounded neutral point treatment. Besides the spatial extension of the low voltage grid, also the line resistances are higher for transmission lines than for the high- and extra-high-voltage level, hence they suppress the GIC currents more.

The overall circuit length of the Austrian TSO is more than 6 800 km and involves the voltage levels of 400 kV with 2 400 km system length, 230 kV with 3 200 km system length and 110 kV with 1200 km system length [117]. For this study, only the transmission system of the 400 kV and 230 kV are considered due to the longer transmission lines in general. It is shown later in

subchapter 6.4.3.2, that the computed currents in the 400 kV transmission system are insignificant effected by the 230 kV transmission system. Therefore, the influence of the 110 kV transmission system to the higher voltage levels is also expected to be insignificant.

Due to the plane-wave method only the end points of the transmission lines are of interest. Thus the map from Figure 4-4 can be simplified to straight lines as shown in Figure 6-4 with the straight forward transmission lines between two substations. The existence of more than one transmission circuits for the same voltage level between two substations is considered in the model. Each substation node connects the 400 kV and/or 230 kV voltage level in the substation neutral, based on the network configuration. It is assumed for the power network model, that each voltage level in the substation is directly grounded via one transformer, so there is only one connection between each voltage level in the substation to the substation neutral. The substation neutral is linked via one grounding resistance (substation earthing system) to the substation grounding.

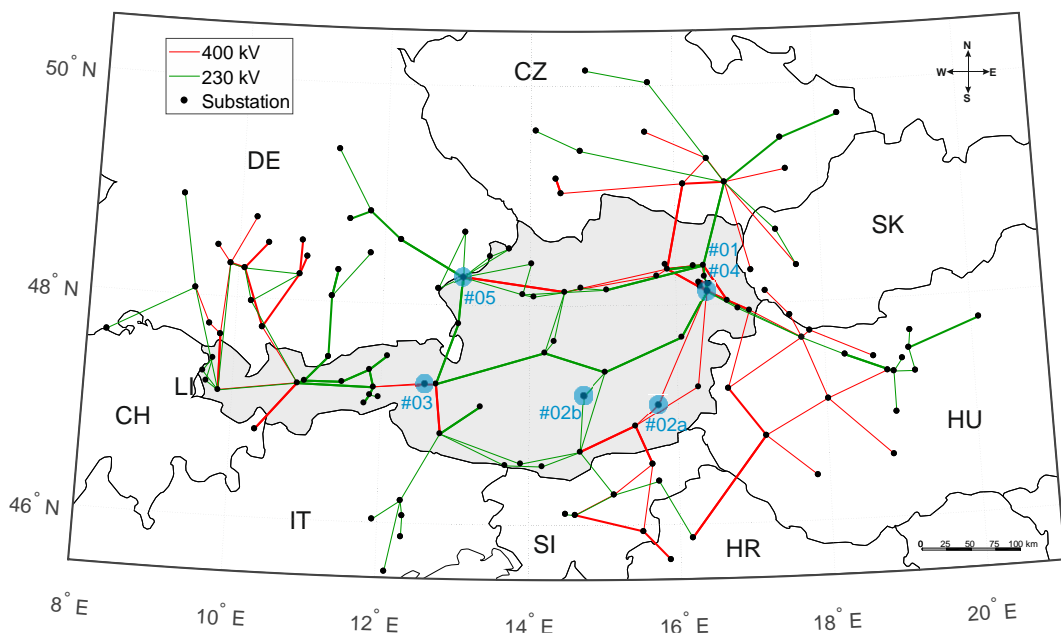


Figure 6-4 Map of the simplified Austrian transmission system grid and tie lines to neighbouring transmission systems. The measurement points and client numbers are marked in cyan.

Figure 6-4 maps the investigated area for this study; the simplified transmission grid of Austria and tie lines of neighbouring countries. The network model has in total 126 # substations, 51 # of those stations are located within Austria. More details about the investigated power grid model are tabulated in Table 6-2. The values of the line resistances, transformer winding resistances and grounding resistances are standardised values, if no specific parameter for the component is given.

Table 6-2 General Parameter of the applied power network model.

	Voltage level	
	400 kV	230 kV
Line resistance R_L	0.02 Ω /km per phase	0.06 Ω /km per phase
Winding resistance R_W	0.2 Ω per phase	0.06 Ω per phase
Grounding resistance R_G	0.2 Ω	

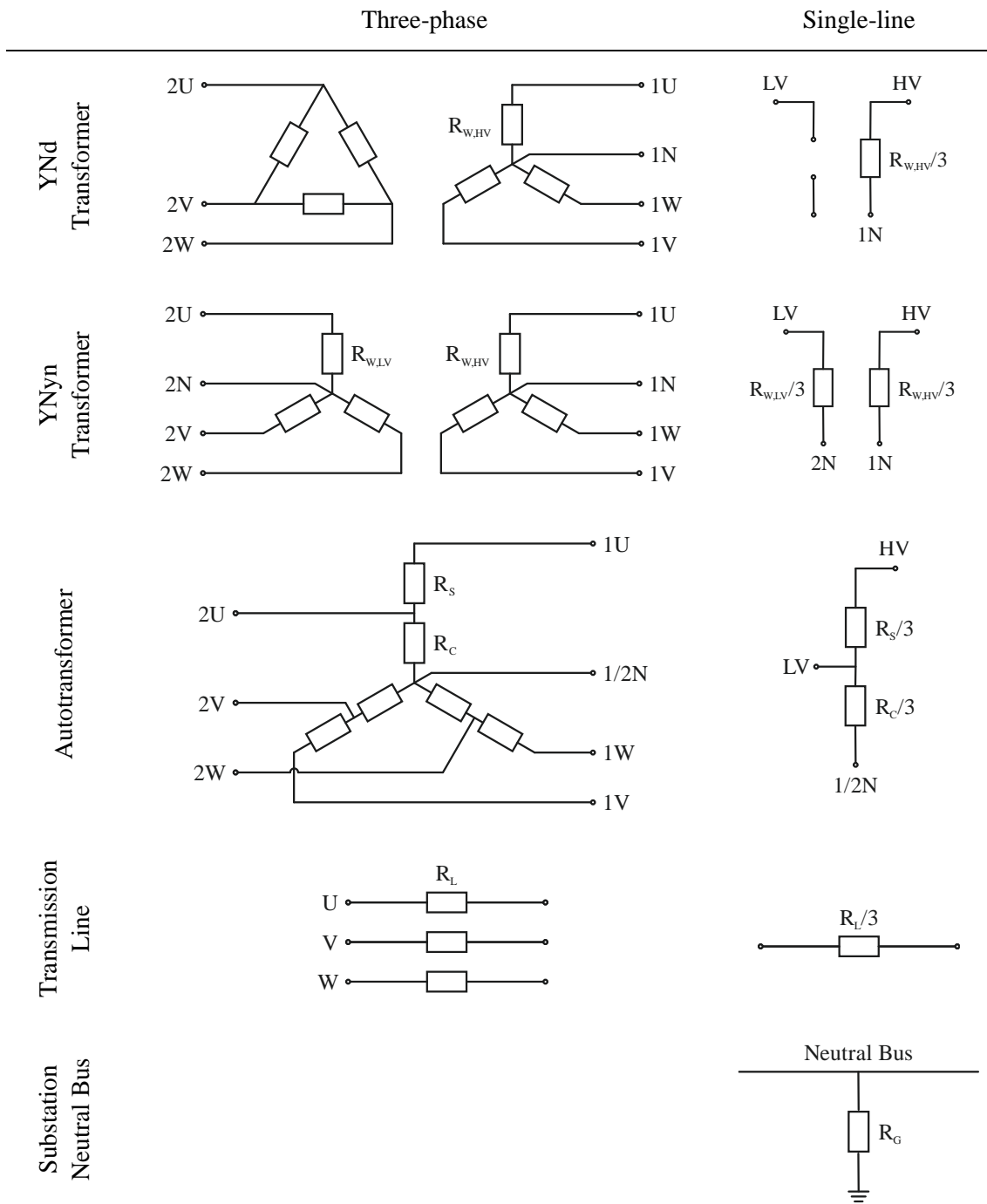
In general, only the resistive values of the power grid network are of importance for GIC studies due to the quasi DC. Relevant resistances are the transmission line R_L , the general transformer winding R_W and the grounding of the substation R_G . The 400 kV and 230 kV line resistances given in Table 6-2 are mean values of the total lines. However, if there are no specific data of the network parameter available, the values outlined in Table 6-2 can be used, which are also recommended in the literature [118], [119]. This study primary uses the real network parameter and for unknown values, the suggested values in the table are applied.

The transformer winding can be connected as delta (d) or star (y) and depends on the neutral point treatment of the voltage level. Due to the fact that the delta-connection has no grounding point, there will be no GIC flow and can therefore be neglected for those investigations. A special transformer type is the autotransformer, which has a common winding R_C for the high- and low-voltage side and a series winding R_S only for the high-voltage side. In the analysed power grid model, there are two autotransformer implemented. All the others are modelled as star-connected configuration on the 400 kV and 230 kV voltage side.

The neutral bus connects the grounding system of the substation with the 400 kV and 230 kV windings of the transformer. Therefore, the grounding resistance R_g is the common path of the different voltage levels' current flow.

Assuming further that the resistances of each three-phase component are totally equal, the power network model can be reduced to a single-phase model [120]. Therefore, the resistance of the transmission lines and transformer windings are divided by three. The DC equivalent and implementation to the single-line power network model of the transformer windings, lines and groundings are listed in Table 6-3.

Table 6-3 Transformer DC equivalent for the simulation model. [121]



6.3.3 Calculation of GIC using Network Theory

Two approaches are common to calculate the network currents from the geoelectric field. One method is called the Lehtinen-Pirjola method [10], [122], which is more common for geophysicist. The other one is the nodal admittance matrix method, which is well-known in electrical engineering. Both approaches are on the basis of network theory and the only differences are in performing the calculation steps and creating the matrices. However, both methods are mathematically identical as pointed out in [120] and can be used for GIC computation. This work focuses on the classical nodal admittance matrix method.

In this work, the driving GIC voltage sources are assumed to be located between the groundings of the substations, which is acceptable according to a uniform geoelectric field. To compute the amplitudes of the driving voltage sources V_S in the network from the horizontal geoelectric field components, the path length between two points are needed as can be seen from equation (6.19). Generally, the distances are calculated between two substations or from one substation to any reference substation. Figure 6-5 shows the schematic of the transmission grid for two different voltage levels (one voltage level in black and the other in grey) with a reference substation r and a second substation i .

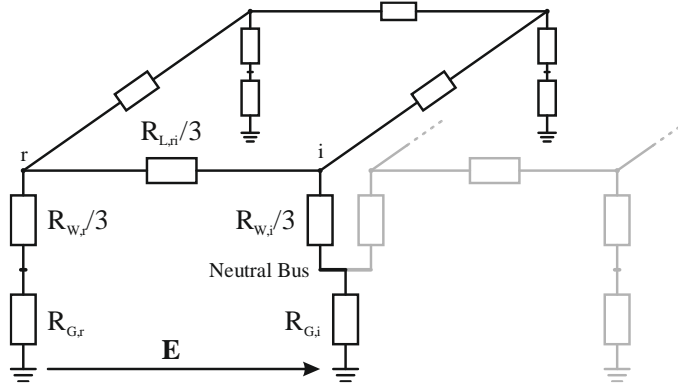


Figure 6-5 Schematic of the power network model⁷ for different voltage levels.

As a first step all nodes N_N and branches N_B in the power grid network are defined. The whole power grid network contains a specific amount of substations N_{Sub} , transformer windings N_{Tra} and lines N_{Lin} . However, a detailed draft of the GIC computation steps for the power system model, based on the calculated geoelectric fields, are subsequently outlined.

1) Distances L_x and L_y

The distances L_x and L_y are calculated in (6.20) - (6.21) from the latitudes and longitudes (in degrees) between the substation i to a reference substation r . Taking into account the Earth geometry, the eastward distance is not easy to compute only from the longitudes, because they converge at the poles and additionally of the non-spherical shape of the Earth, which is more an ellipsoid. The shape characteristics are considered for the distance calculations as formulated in [49], [119], [123].

⁷ Remark: the substation groundings can be represent by different earth potentials, which is only valid for uniform fields

$$L_{x,i} = 111,2 \cdot (lat_i - lat_r) \quad (6.20)$$

$$L_{y,i} = 111,2 \cdot (lon_i - lon_r) \cdot \sin\left(90^\circ - \frac{lat_i + lat_r}{2}\right) \quad (6.21)$$

L_x, L_y	northward and eastward distance with size $N_{Sub} \times 1$, [km]
lat	geographic latitude, [degree]
lon	geographic longitude, [degree]

2) Directed and Weighted Branch-Node Matrix BNM

After the distances are known, the next step is to set up the weighted Branch-Node matrix BNM , which is the directed incidence matrix of the grid multiplied with the diagonal branch admittance matrix. BNM defines the relation between branches and nodes, i.e. the topology of the system. Generally, the incidence matrix consists of zeros and ones; in this case, the BNM matrix is modified by the branch conductance per phase as gives (6-22)

$$BNM = \begin{cases} +\frac{1}{R_b} & \text{sending node} \\ -\frac{1}{R_b} & \text{receiving node} \\ 0 & \text{if branch } b \text{ does not touch node } n \end{cases} \quad (6-22)$$

BNM	weighted branch-node matrix with size $N_B \times N_N$, $\left[\frac{1}{\Omega}\right]$
R_b	resistance of the branch, [Ω]

The structure of the BNM matrix is given in (6-23) and is partitioned according to branch types (lines, transformer windings, groundings). According to this thesis definition, the rows in the BNM_{Tra} matrix are alternating between 400 kV and 230 kV level for each transformer and represent the transformer windings.

$$BNM = \begin{bmatrix} BNM_{Lin} \\ BNM_{Tra} \\ BNM_{Sub} \end{bmatrix} \quad (6-23)$$

BNM_{Lin}	weighted line branch-node matrix with size $N_{Lin} \times N_N$
BNM_{Tra}	weighted transformer branch-node matrix with size $N_{Tra} \times N_N$
BNM_{Sub}	weighted substation branch-node matrix with size $N_{Sub} \times N_N$

3) Admittance Matrix Y

In a next step the admittance matrix Y is computed by using expressions (6.24) - (6.25) [118], with the structure of the admittance matrix outlined in (6.26). The network admittance matrix Y_N with the size $N_{Net} \times N_{Net}$ includes all nodes except the grounding points of the substations. The grounding admittance matrix Y_G includes the earthing systems at the substations. The coupling admittance matrix Y_C connects the neutral bus bar with the grounding point of the substation.

$$Y_{ij} = -\frac{1}{R_{ij}}, \quad i \neq j \quad (6.24)$$

$$Y_{ij} = \sum_{k=1, k \neq i}^N \frac{1}{R_{ik}}, \quad i = j \quad (6.25)$$

$$Y = \begin{bmatrix} Y_N & Y_C \\ Y_C^T & Y_G \end{bmatrix} \quad (6.26)$$

Y	admittance matrix with size $N_N \times N_N$, $\left[\frac{1}{\Omega}\right]$
Y_N	network admittance matrix with size $N_{Net} \times N_{Net}$, $\left[\frac{1}{\Omega}\right]$
Y_C	coupling admittance matrix with size $N_{Net} \times N_{Sub}$, $\left[\frac{1}{\Omega}\right]$
Y_G	grounding admittance matrix with size $N_{Sub} \times N_{Sub}$, $\left[\frac{1}{\Omega}\right]$

4) Network Currents I

After the parameters of the matrices are known, the GIC driving voltage sources V_S for substation i can be computed as quoted in (6-27).

$$V_{S,i} = [L_{x,i} \quad L_{y,i}] \cdot \begin{bmatrix} E_x \\ E_y \end{bmatrix} \quad (6-27)$$

V_S	driving voltage source with size $N_{Sub} \times t$, [V]
E_x, E_y	northward and eastward geoelectric field with size $1 \times t$, $\left[\frac{V}{km}\right]$

In general the whole network can be described using nodal analysis given in (6-28)

$$\begin{bmatrix} 0 \\ I_{Sub} \end{bmatrix} = \begin{bmatrix} Y_N & Y_C \\ Y_C^T & Y_G \end{bmatrix} \cdot \begin{bmatrix} V_N \\ V_S \end{bmatrix} \quad (6-28)$$

V_N	network nodal voltages with size $N_{Net} \times t$, [V]
I_{Sub}	total substation (grounding) currents with size $N_{Sub} \times t$, [A]

with V_S as the calculated input parameters and V_N and I_{Sub} as unknown variables.

After rearranging the first row in equation (6-28), the network nodal voltage V_N can be calculated as described by formula (6-29).

$$V_N = -inv(Y_N) \cdot Y_C \cdot V_S \quad (6-29)$$

If all node voltages are known, the currents of the network can be calculated quoted in (6-30) using the BNM matrix.

$$\begin{bmatrix} I_{Lin} \\ I_{Tra} \\ I_{Sub} \end{bmatrix} = \begin{bmatrix} BNM_{Lin} \\ BNM_{Tra} \\ BNM_{Sub} \end{bmatrix} \cdot \begin{bmatrix} V_N \\ V_S \end{bmatrix} \quad (6-30)$$

I_{Lin} line currents with size $N_{Lin} \times t$, [A]
 I_{Tra} transformer (winding) currents with size $N_{Tra} \times t$, [A]

Inserting equations (6-29) and (6-27) into (6-30), the currents in the network can be directly calculated from the geoelectric field by using the system network matrix C in (6-31).

$$\begin{bmatrix} I_{Lin} \\ I_{Tra} \\ I_{Sub} \end{bmatrix} = \underbrace{\begin{bmatrix} BNM_{Lin} \\ BNM_{Tra} \\ BNM_{Sub} \end{bmatrix} \cdot \begin{bmatrix} -inv(Y_N) \cdot Y_C \cdot V_S \\ 1 \end{bmatrix}}_{[C]} \cdot \begin{bmatrix} L_x & L_y \end{bmatrix} \cdot \begin{bmatrix} E_x \\ E_y \end{bmatrix} \quad (6-31)$$

C system network matrix with size $N_B \times 2$, $\left[\frac{km}{\Omega}\right]$

Note that the line currents and transformer winding currents have to be divided by three to get the per phase currents.

Validation of the power system model. To ensure the correct GIC network computation from the geoelectric field, the simulation method was validated by the test case scenario given in [119]. The calculations from the simulation method perfectly fit according to the results outlined in the paper.

6.4 Application of the Modelling Method on the Austrian Transmission System

6.4.1 Surface Impedance

The surface impedance $Z(\omega)$ is calculated according to equations (6.9) - (6.14) by applying the 1D-layered earth conductivity model #39 and #55 given in Table 6-1, which are representative for the Austrian geological structure. The results of the surface impedance computations are outlined in Figure 6-6 in a Bode diagram, with the magnitude and phase of the surface impedance $Z(\omega)$ presented as function of the frequency.

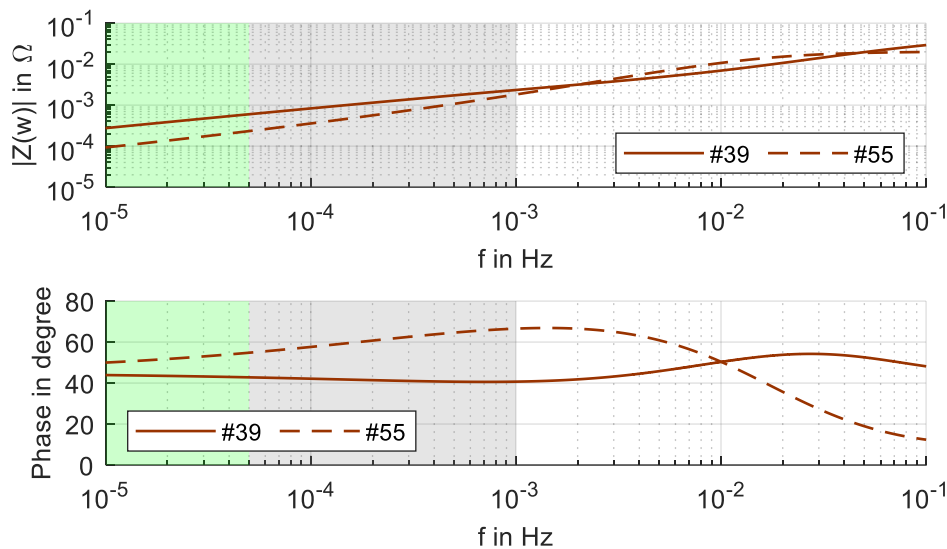


Figure 6-6 Bode diagram of the surface impedance $Z(\omega)$ of the 1D-layered earth conductivity model #39 and #55 and a sample rate of 1 s. Significant frequency ranges of the geomagnetic field are marked (see text below).

From the Fourier analysis of the geomagnetic field and transformer neutral current in subchapter 5.2.3, the same characteristic frequency ranges between 10 μ Hz to 50 μ Hz and 50 μ Hz to 1 mHz are marked in Figure 6-6 with green and grey. Within the relevant frequency ranges, the magnitude of model #39 is greater than for model #55. Notable from the phase plot is, that from 10 μ Hz up to 1 mHz, the phase of model #39 is more or less at a constant level about 40°. According to the same frequency range, the phase of model #55 increases from 50° up to 65°.

6.4.2 Geoelectric Field

Starting by the time-series of the geomagnetic field, the Fourier transform is applied on the data to calculate the geomagnetic field in the frequency domain, as already mentioned in the general method load flow in Figure 6-1. Thereafter, the surface impedance can be calculated using formula (6.8) - (6.14), based on the layer thicknesses and conductivities from the 1D-layered Earth model, and according to the frequency spectrum. After the geomagnetic field and the surface impedance are known in the frequency domain, the geoelectric field can be calculated by applying equations (6.15) - (6.16) and afterwards transformed to the time domain.

Calculations on the geoelectric field are performed on both 1D-layered conductivity models to estimate the differences between them. The observation period between 07. – 08. September 2017,

based on a sample rate of 1 s, was chosen to compare the moderate geomagnetic activity of the first day with the strong activity of the second day. The whole observation time was chosen as the window length for the Fourier transformation.

The results of the computations are outlined in Figure 6-7, where the middle subplot shows the northward E_x and eastward E_y geoelectric field component of model #39, the bottom subplot displays the same components for model #55. Additionally added in the top of the figure is the geomagnetic activity index K_p , which was present during that time.

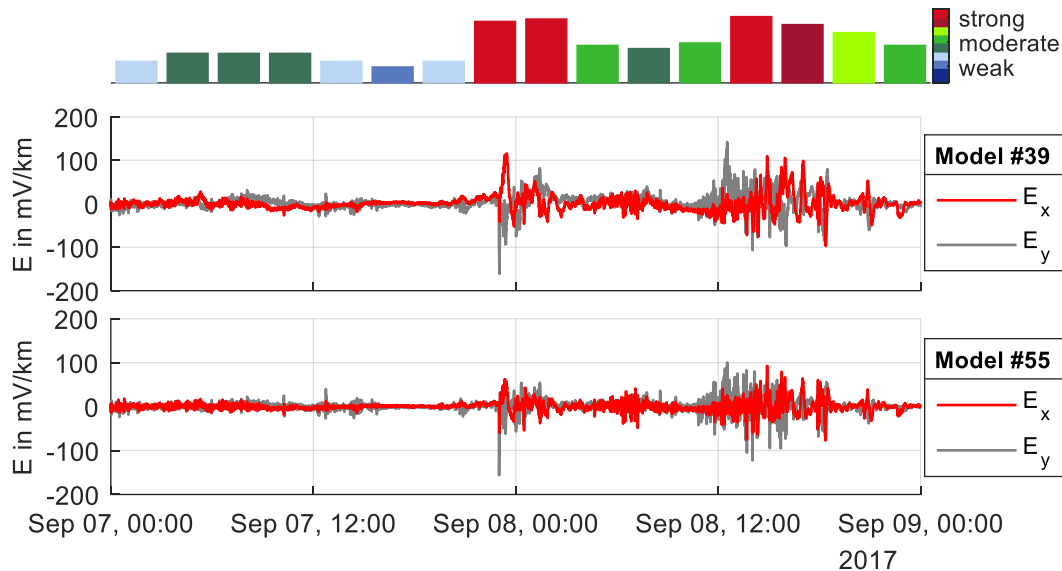


Figure 6-7 Geoelectric field based on conductivity model #39 and #55 from 07. – 08. September 2017 with a sample rate of 1 s.

It can be seen from the plot, that both models have increased electric field components during the strong geomagnetic activities $K_p \geq 7$ - compared to the day of moderate geomagnetic activity. In general, both models tend to have the same geoelectric field pattern, but the amplitudes of model #39 are larger than for model #55.

The dominant frequency range of geomagnetic induction and therefore occurrence of the different surface impedance magnitudes for both models can argue this. Within the relevant frequency range from 10 μ Hz up to 1 mHz, the magnitude of the impedance of model #39 is higher than for model #55. Therefore, the computed geoelectric field from equation (6.8) of model #39 tends to have higher values than for model #55.

Geoelectric field based on geomagnetic activity. In a next step, considerations about the different geomagnetic activities during a day and the resulting geoelectric fields are presented. Based on the geomagnetic activities for 2017, the days are categorised as follows

- weak day: K_p index never exceeds the 3+ threshold
- moderate day: one K_p index is greater than 3+, but less than 7-
- strong day: one K_p index is greater than 6+

Due to this categorisation, 241 days of weak, 124 days of moderate and 4 days of strong geomagnetic activity are observed. After the days are identified, the geoelectric field are allocated to those days. Then, for each categorised day, the lower 10 %- and upper 90 %-quantile for each

time step (1 s) within the 24 h is computed. The envelope curve of the northward and eastward geoelectric field, bounded by the upper and lower quantiles, are plotted in Figure 6-8. So within the envelope curve, there are 80 % of the geoelectric field values. The geoelectric field computations are performed for a 1 s data rate and only the conductivity model #39 is considered for this analysis. (The analysis of model #55 shows approximately the same profile, but generally has lower amplitudes.)

Differences between the weak and moderate days can be determined by the width of the envelope curve: the mean width for weak days is about 10 mV/km and for the moderate days approximately twice. Weak and moderate days show a more or less common daily pattern, where especially the northward geoelectric field component rises in the morning, followed by a decreasing section up to midday and subsequent increases to a constant level.

A completely different picture can be observed by the days with strong geomagnetic days, where the high amplitudes of the field components can occur any time. However, the width of the envelope curve reaches values of approximately 50 mV/km up to 100 mV/km, with the maximum of the magnitude of the geoelectric fields are $E_{x,\max(1s)} \approx 125 \text{ mV/km}$ and $E_{y,\max(1s)} \approx 160 \text{ mV/km}$.

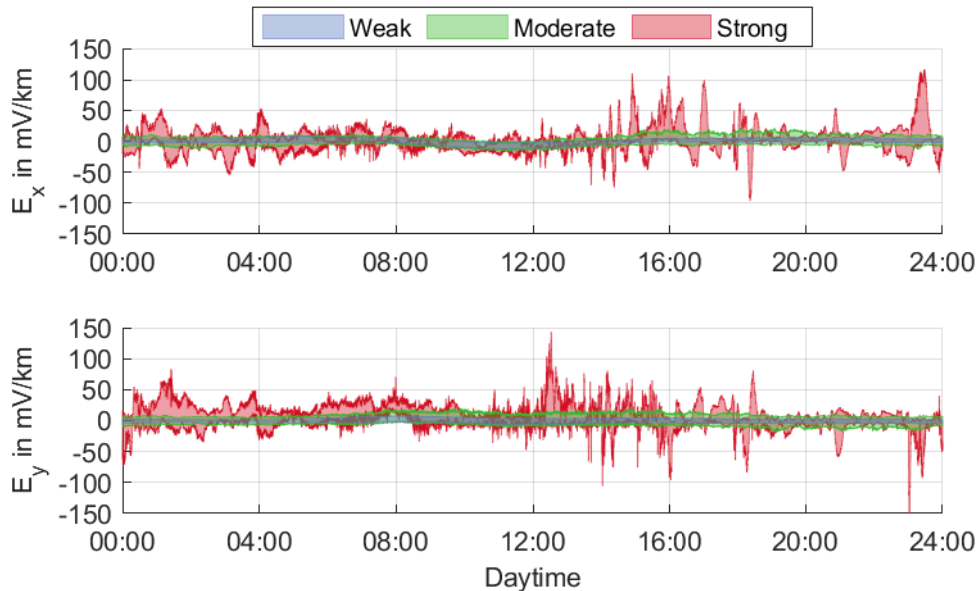


Figure 6-8 Envelope curve of the 10 %-quantile and 90 %-quantile of the geoelectric field (earth model #39) for the categorised days strong, moderate and weak. Observation period was the year 2017 with a sample rate of 1 s.

An overview of the separated horizontal geoelectric field components regarding to the geomagnetic activities is outlined in the Appendix B. It contains the minimum and maximum values, the median value and the 10 %-quantile and 90 %-quantile of each categorised day. The data in the appendix are digital low-pass filtered and down-sampled to 1 min values. The extreme values are $E_{x,\max(1\text{min})} \approx 110 \text{ mV/km}$ and $E_{y,\max(1\text{min})} \approx 100 \text{ mV/km}$ respectively.

In [124], investigations on a 100 year geomagnetic storm scenario are performed. It is outlined a maximum of geoelectric fields from 500 mV/km up to 2 V/km, which depends on the geomagnetic location and predominant earth conductivities. Comparing those values with the modelled geoelectric fields, it seems that the later on calculated GIC can be multiplied by a factor of 5 to 20 to get the currents for a worst-case scenario.

6.4.3 Transformer Neutral Currents of Simulation and Measurements

The comparison between simulations and measurements are categorised into 400 kV and 230 kV voltage level. The observation time is chosen from 07. – 08. September 2017, where the geomagnetic activity for the first day was moderate and for the second day strong. For this analysis, the filtered and reduced data to 1 min sample rate are applied. The transformer neutral currents of each substation are plotted in Figure 6-9 and Figure 6-10, with the measurement marked in bold and with the simulations outlined with thin lines. The linear regression analysis, based on the xy-plot on the right, gives the relation between the measured and simulated currents.

The DC measurements are used to evaluate the GIC simulation method and to determine the appropriate 1D-layered earth conductivity model for Austria. For clarity reasons, only the GIC computation results of model #39 are visualised in this subchapter. The choice of which model is more convenient is based on the correlation r and gradient β_1 of the linear regression analysis.

6.4.3.1 Transformer Neutral Currents of the 400 kV Transmission System

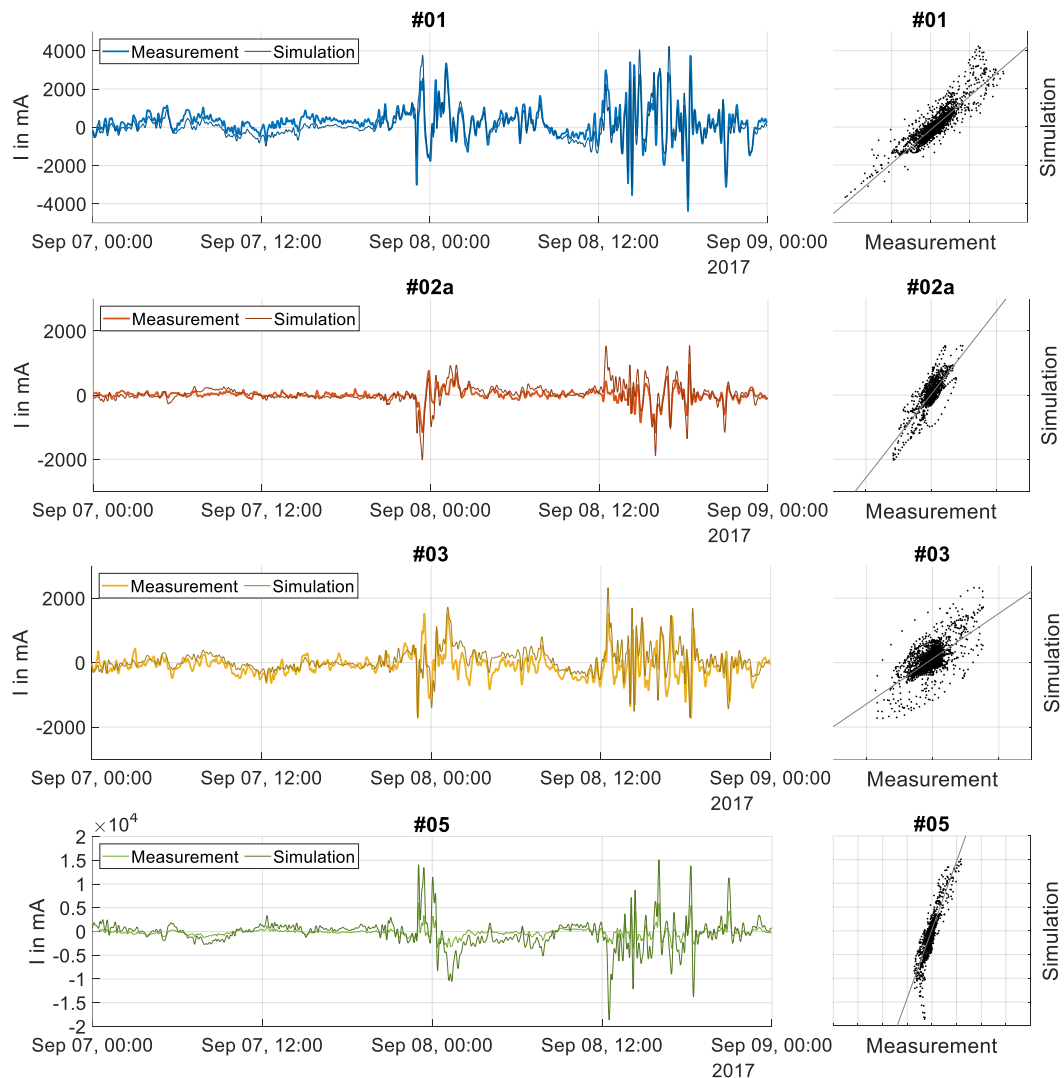


Figure 6-9 400 kV transformer neutral current analysis of 2 days with the scatter plot and linear trend line for regression analysis on the right. Observation time from 07. – 08 September 2017 with digital low-pass filter $f_c = 1 \text{ mHz}$ and reduced data to 1 min samples.

It can be seen from Figure 6-9, that both signals have nearly the same pattern and indicate high correlations during the observed time. Especially for the period of strong geomagnetic activity, the resulting current peaks occur in simulations and measurements.

Correlation coefficient r_{XY} . The correlation coefficient r_{XY} is used for statistical analysis and is outlined in Table 6-5. The first row of each client gives the correlation between the measurement and the simulation as plotted in Figure 6-9. The strong visual link between the signals in the scatter plot can be confirmed by the high correlation coefficients.

Because the computed current is a combination between the northward and eastward geoelectric field, the simulated currents can also be split into the x- and y-component, which reveals the second and third line of each client, referenced as $r_{XY,x}$ and $r_{XY,y}$. Separate the simulated current components and compare it to the measurement ones, gives the impact of each component to the monitored current. It can be seen from the table, that the measurements of client #01, #02a and #03 correlate higher with the northward than with the eastward field component. In contrast, the contribution of the eastward component is significant high for client #05. The northward component of this client can be more or less neglected.

Over- and underestimation coefficient β_1 . It can be seen from Figure 6-9 that the simulated amplitudes can differ from the measured currents. Therefore, a second criteria is introduced to evaluate the simulation model on over- or underestimating the current according to the gradient of the trend line from the linear regression analysis.

A linear trend line (grey line) is applied on the xy-plot in Figure 6-9, based on equation (5-17) from the linear regression analysis. Generally, defining Y for simulation values, X for measurement values and making the assumption of for example positive correlation, which means the coefficient β_1 is within the range $0 \leq \beta_1 \leq \infty$, following categorisation in Table 6-4 can be outlined. For negative correlations, the estimation value has to be applied correspondingly the other way around.

Table 6-4 Estimation of the simulation Y determined by the gradient β_1 on over- or underestimation.

Gradient	Estimation of Simulation
$\beta_1 > 1$	Overestimation
$\beta_1 = 1$	Exact average match
$0 < \beta_1 < 1$	Underestimation
$\beta_1 = 0$	No linear dependence

Both criteria, the correlation coefficient as the over/underestimating coefficient to validate the simulation model are outlined in Table 6-5. It can be derived from the table that the computation of client #01 and #03 is generally underestimated, whereby for client #02a and especially #05 is overestimated. Only for client #05 computes the earth model #55 better results due to the β_1 coefficient, but the correlation of this model is lower compared to model #39. In all other cases, the model #39 has better results.

Table 6-5 400 kV analysis of the simulation and measurement correlation r_{XY} and the over/underestimating coefficient β_1 during observation from 07. – 08 September 2017.

		Model #39		Model #55	
		r_{XY}	β_1	r_{XY}	β_1
#01	r_{XY}	0.89	0.88	0.81	0.44
	$r_{XY,x}$	0.75	-	0.75	-
	$r_{XY,y}$	0.40	-	0.22	-
#02a	r_{XY}	0.79	1.3	0.77	0.67
	$r_{XY,x}$	0.78	-	0.65	-
	$r_{XY,y}$	0.5	-	0.54	-
#03	r_{XY}	0.66	0.70	0.52	0.30
	$r_{XY,x}$	0.75	-	0.68	-
	$r_{XY,y}$	0.34	-	0.22	-
#05	r_{XY}	0.87	2.88	0.79	1.4
	$r_{XY,x}$	-0.07	-	-0.19	-
	$r_{XY,y}$	0.88	-	0.80	-

6.4.3.2 Transformer Neutral Currents of the 230 kV Transmission System

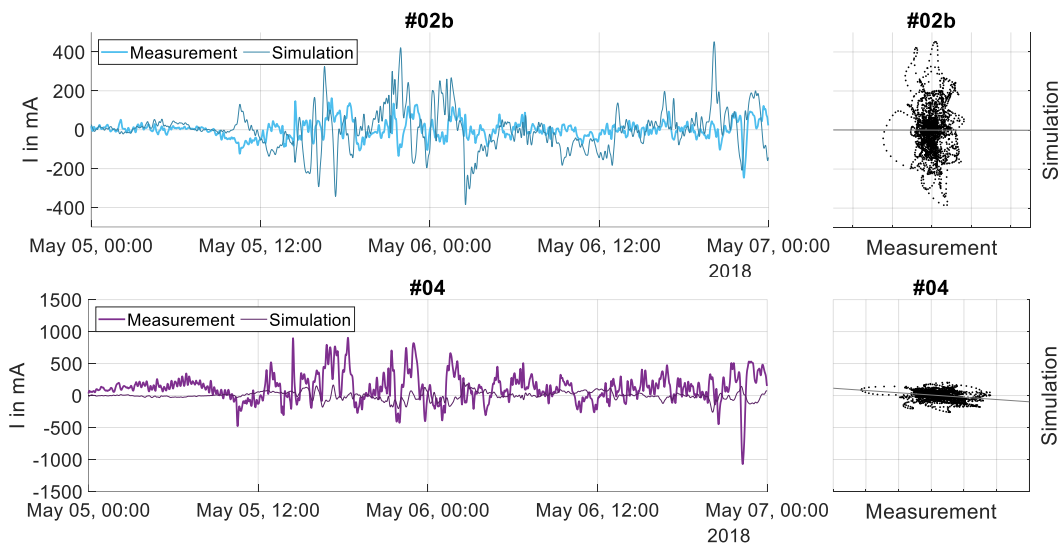


Figure 6-10 230 kV transformer neutral current analysis of 2 days with the scatter plot and linear trend line for regression analysis on the right. Observation time from 05. - 06. May 2018 with digital low-pass filter $f_c = 1 \text{ mHz}$ and reduced data to 1 min samples.

The same analysis as for the 400 kV system currents is performed for the 230 kV system currents. Again a two day observation time with reduced data rate is chosen but for another date, from 05. - 06. May 2018, where both 230 kV measurement data exist. It can be seen from Figure 6-10 and Table 6-6 that a correlation between simulation and measurement cannot be determined, although each separated current component has relative high correlations. The same observation was made by model #55.

Table 6-6 230 kV analysis of the simulation and measurement correlation r_{XY} and the over/underestimating coefficient β_1 during observation from 05. – 06. May 2018.

		Model #39		Model #55	
		r_{XY}	β_1	r_{XY}	β_1
	r_{XY}	0	-0.01	-0.07	-0.08
#02b	$r_{XY,x}$	0.71	-	0.69	-
	$r_{XY,y}$	-0.61	-	-0.64	-
	r_{XY}	-0.25	-0.07	-0.22	-0.03
#04	$r_{XY,x}$	-0.71	-	-0.71	-
	$r_{XY,y}$	0.63	-	0.64	-

6.4.3.3 Decoupling of the Transmission Grid.

For a hypothetical test scenario, the network topology was changed according to the grounding of the transformer in the substations. The modified approach was to delete the neutral bus in each substation, which concludes that the transformer neutral of each voltage level is direct-grounded to a separate substation grounding system. This means a decoupling of the 400 kV and 230 kV power network grid. The results of the test scenario are outlined in Table 6-7 for the 400 kV system and in Table 6-8 for the 230 kV system.

Table 6-7 400 kV analysis of the simulation and measurement correlation r_{XY} and the over/underestimation coefficient β_1 for decoupled network topology, based on earth model #39. Observation from 05. – 06. May 2018.

		Real Network Topology		Decoupled Network Topology	
		r_{XY}	β_1	r_{XY}	β_1
	r_{XY}	0.86	0.88	0.87	0.82
#01	$r_{XY,x}$	0.72	-	0.72	-
	$r_{XY,y}$	0.56	-	0.56	-
	r_{XY}	0.72	0.79	0.86	0.91
#03	$r_{XY,x}$	0.78	-	0.78	-
	$r_{XY,y}$	0.45	-	-0.45	-
	r_{XY}	0.91	4.21	0.91	3.68
#05	$r_{XY,x}$	-0.23	-	-0.23	-
	$r_{XY,y}$	0.92	-	0.92	-

Table 6-8 230 kV analysis of the simulation and measurement correlation r_{XY} and the over/underestimation coefficient β_1 for decoupled network topology, based on earth model #39. Observation from 05. – 06. May 2018.

		Real Network Topology		Decoupled Network Topology	
		r_{XY}	β_1	r_{XY}	β_1
	r_{XY}	0	-0.01	0.63	1.38
#02b	$r_{XY,x}$	0.71	-	0.71	-
	$r_{XY,y}$	-0.61	-	-0.61	-
	r_{XY}	-0.25	-0.07	0.9	0.58
#04	$r_{XY,x}$	-0.71	-	0.71	-
	$r_{XY,y}$	0.63	-	0.63	-

The correlation and linear regression coefficients of the 400 kV client #01 and #05 hardly differ from the previous ones. A slightly positive trend to a higher correlation value can be determined by client #03. But in general, it is obtained that the voltage level decoupling causes no significant changes of the 400 kV transformer neutral currents and therefore no significant influence of the 230 kV system to the 400 kV is detected.

However, the greatest positive effect of decoupling the network topology related to the correlation and linear regression coefficients are observed for the 230 kV clients #02b and #04. In this case, the correlation coefficients, and therefore the linear regression coefficient, significantly increase to higher and reasonable values.

6.4.3.4 Conclusion

Based on the correlation and linear regression coefficient for the 1D-conductivity models #39 and #55 in Table 6-5, the first model seems to be more appropriate than the second one to simulate the currents in the Austrian transmission grid.

The computation of the 400 kV transformer neutral currents yields to high correlation values, compared to the measured ones. However, the correlation between the measured and modelled 230 kV transformer neutral currents is not satisfying.

6.5 GIC Distribution and Sensitivity Analysis

The interesting topic for TSO is the power system model of the simulation and the GIC through the power transmission grid. Investigations in this subchapter cover the GIC distribution in the grid and illustrate the sensitivity of the Austrian transmission grid to northward and eastward geoelectric fields. Moreover, endangered points in the grid are outlined and a system parameter study is performed with respect to the influence of transformer neutral grounding.

6.5.1 GIC Distribution

Based on the geoelectric field study with the strong geomagnetic activity and maximum magnitudes of the field components, the distribution of the GIC in the Austrian power transmission grid is under examination. From the geoelectric field data in Figure 6-7, the field components at 7. September 2017 23:25:00 are chosen from model #39. For that time, the values of the northward and eastward field components are 100 mV/km and -70 mV/km, which are one of the highest geoelectric field amplitudes computed in the year 2017. For those fields, the network currents can be calculated by applying formulas (6.20) - (6-31) and the results are outlined in Figure 6-11. It maps the same simplified network as Figure 6-4, but additionally the DC magnitudes of the Austrian transformer neutral are added. The magnitudes are displayed as circles for each voltage level (red for 400 kV and green for 230 kV) and the diameter refers to the magnitude given in the scale besides the legend.

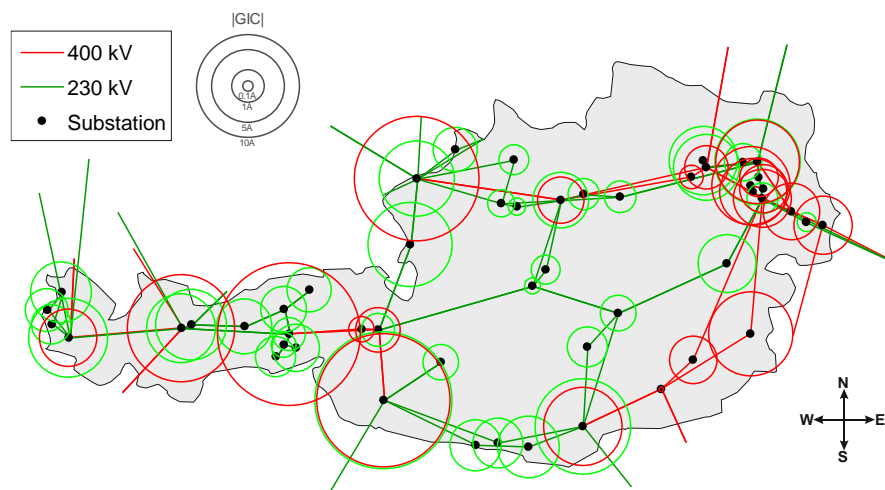


Figure 6-11 Mapping the GIC distribution for $E_x = 100 \text{ mV/km}$ and $E_y = -70 \text{ mV/km}$ in the Austrian transmission grid. The circles refer to the GIC magnitudes for each transformer on the 400 kV and 230 kV voltage level.

It becomes obvious from Figure 6-11 that the GIC in transformer neutral are generally higher for the 400 kV than for the 230 kV transmission system. Reasons for that are the higher conductivities of the 400 kV transmission components compared to the lower voltage level. The range of the magnitudes reaches from a few hundred mA up to ten, twenty ampere.

Additionally, it can be seen that the ends of each voltage-level-subnetwork (stub-lines) tend to have increased magnitudes of the transformer winding currents, than for the inner voltage-level-subnetwork points. This is a result of the network meshing, but depends on the orientation of the connected neighbouring lines and geoelectric field orientation. It is also mentioned in the introduction of this chapter, that lines parallel to the latitude are more sensitive to higher GIC values. Looking on the map in Figure 6-11, there are several substations, which are endpoints of

those parallel lines. So they are highly endangered points in the Austrian transmission grid for stronger GIC impacts, compared to the other substations.

6.5.2 Critical Geoelectric Field Directions

Investigations on the geoelectric field orientation and their influence on the topology of the power grid model are performed. The geoelectric field can be represented in polar coordinates with the horizontal geoelectric field component E_H (respectively the magnitude of E_x and E_y), and the corresponding angle α_E . The polar coordinate counted positive in the mathematically negative direction (clockwise). To be coincide with the geoelectric field directions, the cardinal points are defined as follows:

- Northward $\alpha_E = 0^\circ$
- Eastward $\alpha_E = 90^\circ$
- Southward $\alpha_E = 180^\circ$
- Westward $\alpha_E = 270^\circ$

The idea is to classify the fields by their horizontal component and afterwards analyse the angles, which are related to that magnitudes. For classification of the strength of the field, on the one hand the low-threshold is chosen on the maximum boundaries of the 10 %- and 90 %-quantiles of the moderate northward and eastward geoelectric field in Figure 6-8, on the other hand the upper threshold is set to 80 mV/km, which represents high geoelectric fields for strong geomagnetic activities. So the classification of the horizontal geoelectric field for this investigation is quoted as:

- Low $E_H < 30 \frac{mV}{km}$
- Medium $30 \frac{mV}{km} \geq E_H < 80 \frac{mV}{km}$
- High $E_H \geq 80 \frac{mV}{km}$

The angles of the horizontal geoelectric field in the year 2017 are computed and classified with a bin width of 5° . The figure shows the polar histogram of the field angle distribution, which is scaled to the maximum bin count according to Table 6-9.

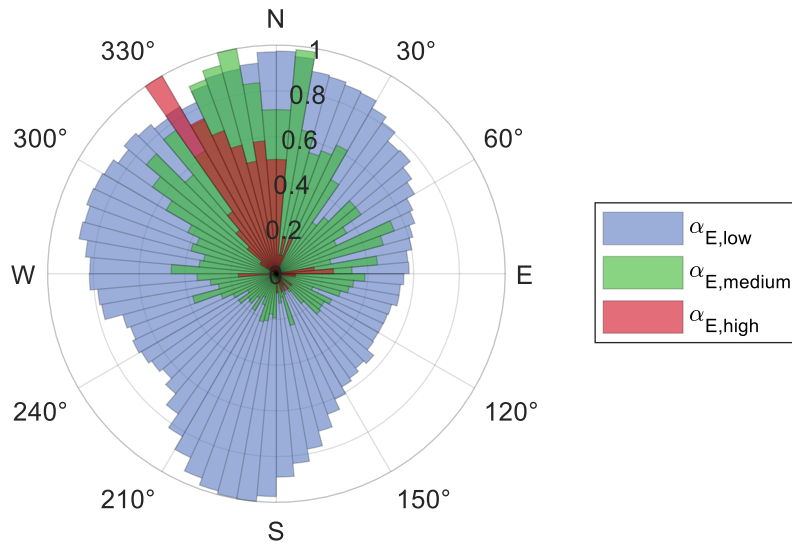


Figure 6-12 Polar histogram in p.u. of the geoelectric field angle α_E during a one year observation in 2017. The angles are classified based on the horizontal geoelectric field amplitudes E_H .

Table 6-9 Bin count of the polar histogram.

Angle of the Geoelectric Field	Total Count	Maximum Bin Count
$\alpha_{E,low}$	518 757 #	9 461 #
$\alpha_{E,medium}$	3 402 #	124 #
$\alpha_{E,high}$	92 #	12 #

It can be derived from Figure 6-12, that the angle of the low magnitudes $\alpha_{E,low}$ characterises a higher tendency to the northward, westward and southward component than to the eastward direction. Considering the angles of a medium field strength $\alpha_{E,medium}$ in green, the field orientation tends to be northward, respectively northwestward directed. A similar pattern is observed for the directions of high horizontal geoelectric fields $\alpha_{E,high}$ in red, which indicate a northwest orientation.

In addition, a seasonal dependency of the field directions was investigated. Therefore, data for the polar histogram were classified into seasons and each polar histogram was computed separately. The plots are outlined in the Appendix C in Figure 8-5 and it is observed, that no significant seasonal dependency can be determined.

Critical geoelectric field directions for substations. After the evaluation of the different magnitude strengths and field directions, the next step is to determine the substations dependency on the geoelectric field orientation. Therefore a synthetic electric field is rotated stepwise from $\alpha_E = 0^\circ \dots 360^\circ$ with a magnitude of $E_H = 100 \text{ mV/km}$. Based on that field rotation, the transformer neutral currents are calculated. For the polar histogram analysis, only substations are selected, where DC monitoring system are installed. The current amplitudes in amperes are plotted in Figure 6-13 using the polar histogram with the same bin width as in Figure 6-12. The currents of client #05 are scaled by a factor of 0.5 due to better graphical representation.

⁸ In principle, a rotation from $\alpha_E = 0^\circ \dots 90^\circ$ is sufficient for complete analysis.

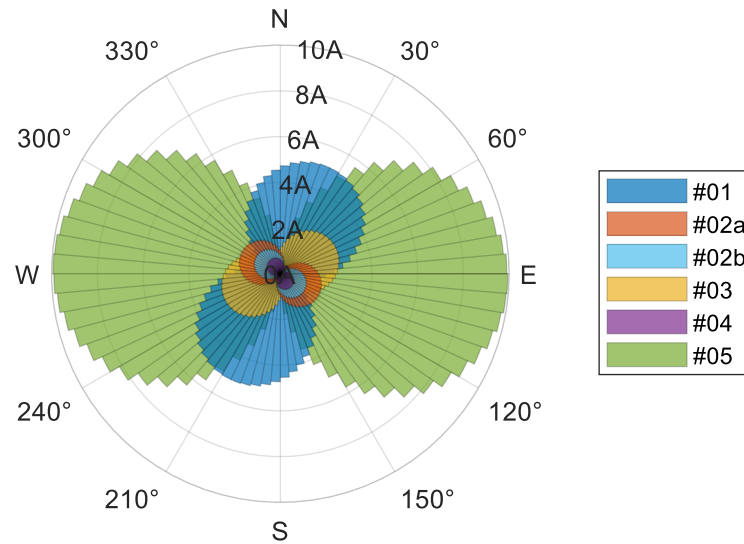


Figure 6-13 Polar histogram of the simulated currents⁹ from the measurement points based on a rotating geoelectric field for $\alpha_E = 0^\circ \dots 360^\circ$ and a magnitude of $E_H = 100 \text{ mV/km}$.

It can be seen from Figure 6-12 that most of the clients have different dependencies of the field direction in the GIC magnitudes. It becomes obvious from the plot, that the eastward and westward field orientation mainly impacts the GIC of client #05. This can be explained by the network topology and the long east-west 400 kV transmission lines which are linked to the substation. The same argument is applicable for client #03, but it seems that the impact of the GIC from the north-south 400 kV lines cannot be neglected.

Client #01 and #04 tend to have a larger influence on the north-south field orientation than to the east-west component. The maximum GIC values of the clients #02a and #02b are between the polar (angle) axes 300° to 330° , respectively 120° to 150° . Comparing the directions with the polar plot of the medium and high geoelectric field magnitudes in Figure 6-12, there seems to be a higher risk for higher GIC derived from the field angle, but the network topology decreases the amplitudes at those substations.

A general overview of the most sensitive geoelectric field orientation for each substation in the Austrian power grid, based on a horizontal geoelectric field of 100 mV/km , is shown in Figure 6-14. The direction of the quiver defines the geoelectric field orientation, according to the highest transformer neutral current at each substation. The length of the quiver gives the maximum magnitude of the 400 kV and 230 kV level transformer neutral current.

Two scenarios are plotted in Figure 6-14: The first scenario in the upper subplot shows the actual power transmission system in Austria. The second scenario in the subplot below considers the planned transmission system in Austria until the year 2030, which is defined in the TSO masterplan 2030 [117]. In this case, it is assumed that the planned grid expansion of the 400 kV is completed, which implies the so-called “400 kV ring” in Austria and the change of the line voltage level from 230 kV to 400 kV in the west part of Austria.

⁹ The plotted values of client #05 are half of the computation, because of a better comparison.

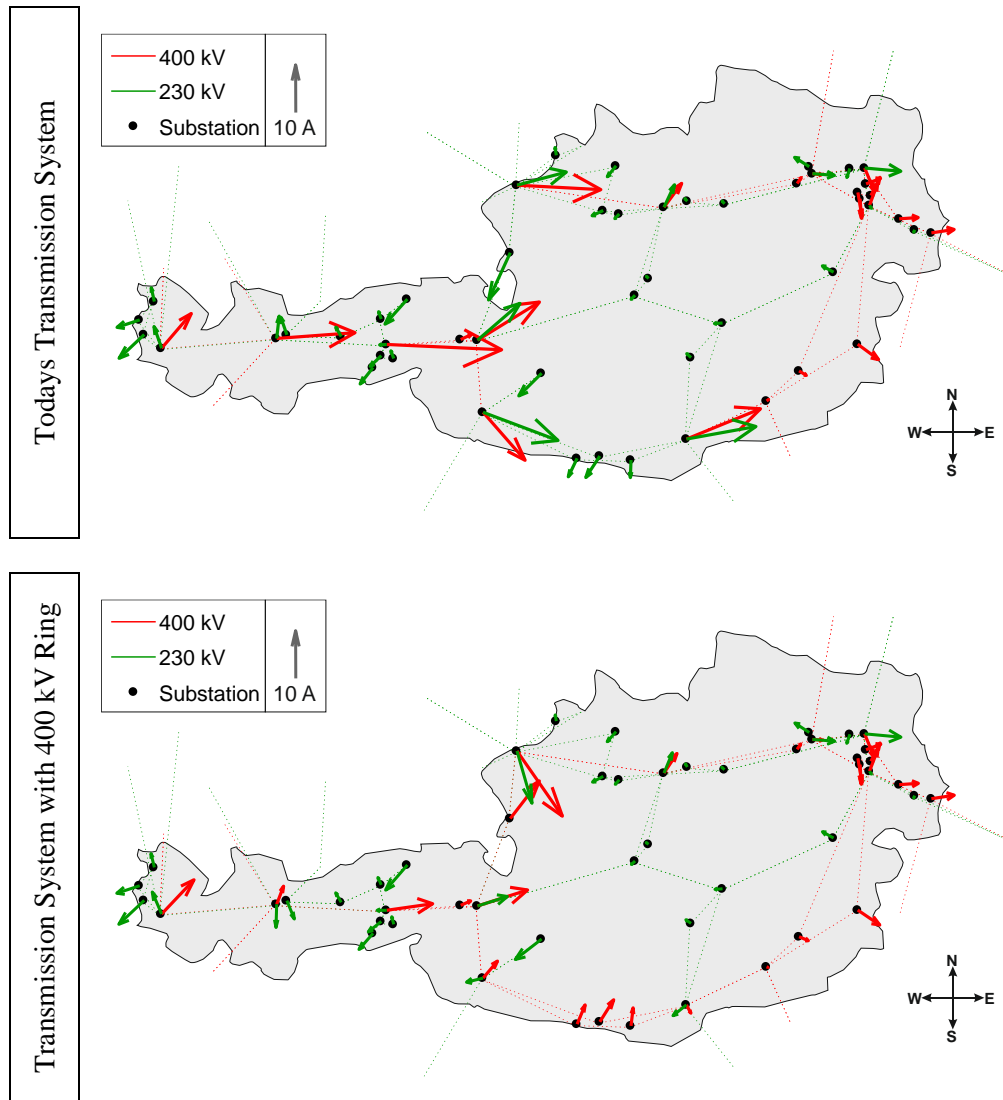


Figure 6-14 Sensitivity map of the actual and planned Austrian transmission system. The quiver direction indicates the most sensitive geoelectric field orientation, based on a horizontal geoelectric field of $E_H = 100 \text{ mV/km}$. The quiver length corresponds to the computed 400 kV and 230 kV transformer neutral current for that field direction.

Focusing on the upper plot of Figure 6-14, there are several substations in the Austrian power transmission system, which experience higher GIC in the transformer neutral. The highest values are detected in the 400 kV, but also the 230 kV system has respectively high values. Considering now the second scenario of the transmission configuration, which is illustrated in the bottom plot of Figure 6-14, the GIC sensitivity changed. Transformers in the 400 kV system, which previously experienced higher values, have now lower GIC sensitivity amplitudes. Only at one substation, where also the measurement client #05 is installed, the amplitudes are consistent and only the sensitivity angle is changed. The sensitivity of the 230 kV substations, which are linked to the modified transmission configuration, also changed to lower GIC sensitivity. Substations, which are further away of the future system modification, showing no amplitude or angle changes.

6.5.3 Transformer Neutral Grounding Sensitivity

The idea behind the transformer sensitivity analysis is to determine the impact of changing the transformer neutral grounding configuration on the remaining network currents. Especially for this investigation, the sensitivity criteria is the change of the transformer neutral current caused by opening the ground connection of selected transformers. For substations with both, 400 kV and 230 kV voltage levels, this means that only one voltage level is disconnected from the substation neutral, whereas the other is still connected via the substation grounding resistance. This seems appropriate for Austria because the voltage levels in one substation are grounded via two separate transformers.

Computations are performed varying all transformer neutrals in the network, but only one case is illustrated in Figure 6-15. In this scenario, an outage of the 400 kV transformer in substation 1 (Neutral Disconnected) is simulated and the network currents of the changed network topology are computed. The computations are performed for the same geoelectric field components $E_x = 100 \text{ mV/km}$ and $E_y = -70 \text{ mV/km}$, as applied in Figure 6-11. The subplot on the top of Figure 6-15 refers to the 400 kV transformer neutral currents and the subplot at the bottom refers to the 230 kV transformer neutral currents. The transformer neutral currents for normal operation are marked in red (400 kV) and green (230 kV). Currents for the 400 kV transformer neutral disconnection in substation 1 are marked in grey. The substations in Figure 6-15 are in ascending order from the left to the right, according to the distance between the transformer outage and the remaining transformers in the power network. The neighbouring substations to substation 1 are marked in cyan. An overview of the location and affiliation of the substation number is outlined in the Appendix D in Figure 8-6.

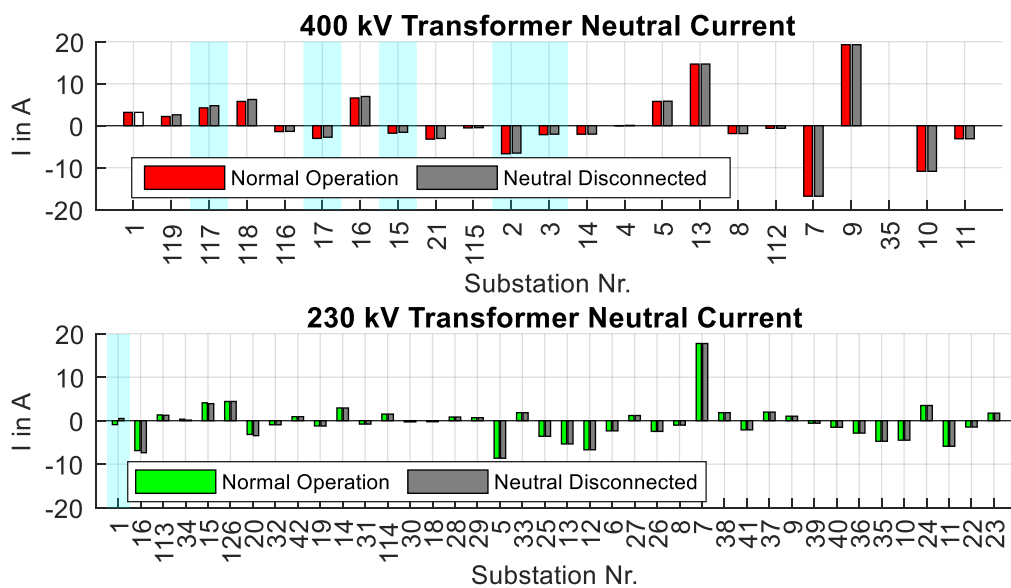


Figure 6-15 Transformer neutral grounding sensitivity. Test case for an outage of the 400 kV transformer in substation 1 (Neutral Disconnected) in the presence of a northward and eastward geoelectric field component of 100 mV/km and -70 mV/km respectively.

It can be seen from Figure 6-15 that in general, the disconnection of the 400 kV transformer neutral in substation 1 has no significant impact on the network currents, with some exceptions. Noticeable changes can be observed for neighbouring transformers or substations, which are very close to the transformer outage. Effects on the transformer neutral currents according to the 400 kV transformer neutral disconnection can also be observed in the 230 kV, but they are still not considerable.

However, in general the impact of a change in transformer neutral configuration (for instance due to a transformer outage) to the network currents depends on the location in the network and the current geoelectric field conditions. In the previously given scenario, the transformer outage occurs on a high degree of intermeshing point. For example, consider the transformer location of client #05 and assume an outage of that transformer in the presence of a strong eastward geoelectric field, this will have a stronger impact on the neighbouring transformers than the previous, illustrated scenario.

6.6 Reverse Calculation of System Parameters

6.6.1 Indirect Determination of the Substation Grounding Resistances

Based on the low correlation between the simulated and measured transformer neutral currents on the 230 kV system, network parameter optimisations are performed to get higher correlation coefficients. The approach is to estimate the grounding values R_G of the network substations based on the available transformer neutral currents. This is performed by defining an optimisation problem, where all grounding resistances in the substations are assumed as optimisation variables. The objective function is to minimise the error between the measured and simulated currents. Therefore, the optimisation algorithm¹⁰ is defined based on the correlation r_{XY} between measurements and computations, as quoted in (6-32) with the condition of the boundary constraint given in (6-33).

$$\min_{R_G} \sum (1 - r_{XY})^2 \quad (6-32)$$

$$0.01 \Omega \leq R_{G,opt} \leq 1 \Omega \quad (6-33)$$

$R_{G,opt}$ optimised substation grounding, [Ω]

The optimisation problem formulated in (6-32) starts by the initial values of all groundings at 200 m Ω , with the boundary constraint of $R_{G,opt}$ given in (6-33), which limitations based on the work [125]. The optimisation algorithm is applied on the same data from subchapter 6.4.3.2 (observation time from 05. - 06. May 2018 and a 1 s sample rate), where the two 230 kV measurements are installed in the transformer neutral. Selected results from the optimisation are stated in Table 6-10 and for comparison reason, the correlation r_{XY} and linear regression β_1 coefficients of the original grounding $R_G = 0.2 \Omega$ are added.

¹⁰ The optimisation problem was solved by the interior point algorithm.

Table 6-10 Optimised substation groundings, correlation coefficient r_{XY} and over-/underestimation coefficient β_1 . Observation from 05. – 06. May 2018 and 1 s sample rate.

	Original			Optimised		
	R_G Ω	r_{XY} -	β_1 -	$R_{G,opt}$ Ω	r_{XY} -	β_1 -
#01	0.2	0.86	0.88	0.07	0.88	1.62
#02a	0.2	-	-	0.56	-	-
#02b	0.2	0	-0.01	0.53	0.41	0.72
#03	0.2	0.72	0.79	0.52	0.79	0.37
#04	0.2	-0.25	-0.07	0.07	0.84	0.88
#05	0.2	0.91	4.21	0.55	0.92	4.02

From the Table 6-10 can be seen, that most of the grounding resistances, where clients are installed, are estimated to be higher than the original selected value of $R_G = 0.2 \Omega$. The increased values are more or less around a level of 0.5Ω . Higher values may be acceptable in case of the geographic locations of mountainous regions, but the value seems to be too high according to substations electrical earthing [125]. Only the grounding value of client #01 and #04, which both correspond to the grounding of one substation, has decreased to a value of 0.07Ω . The reduced grounding value of that substation may be ascribed to the better grounding conditions in valleys, compared to mountainous regions, but this assumes, that also the grounding resistance of client #02a has to be lower, which does not result from the optimisation. Generally, most of the grounding values which are not displayed in the above table, changed to higher values close to $500 \text{ m}\Omega$.

However, changing the power network parameter to the optimised groundings and analysing the correlation r_{XY} and over-/underrating β_1 between simulation and measurement again, the correlation coefficients are generally better (or roughly the same) than compared to the original one. Only the over-/underrating coefficient signifies a more or less inappropriate result.

Notable is that the values for client #04 are significantly better after the optimisation than the original data. Although the correlation coefficient of client #02b is getting better, the value is still low. In general, the impact on the currents of the 230 kV neutral currents is higher than on the 400 kV neutral currents.

6.6.2 Indirect Determination of the Surface Impedance

In general, the GIC modelling starts as shown in the method flow in Figure 6-1, by the geomagnetic field and the earth conductivity structure to compute the geoelectric field. Afterwards network theory is used to calculate the GIC in the grid. In this subchapter, the computation order is the other way around with the idea to determine the geoelectric field from the DC field measurements. Therefore, the GIC equations in section 6.3.3 are used in reversed order, which are hereinafter also referred to as reverse engineering. Before applying the formulas, slightly changes of the matrices, which are clarified in the following subchapters, have to be done.

Once the geoelectric field is computed from the measurements, the next approach is to determine the conductivity of each earth layer. If the geoelectric field E and the geomagnetic field B are known, the surface impedance $Z(\omega)$ can easily be calculated by formulas (6.15) and (6.16). The surface impedance for the 1D-layered earth structure is recursive calculated, starting from the bottom layer to the top to get the transfer function of the earth structure. Therefore, a numerical optimisation algorithm is used to estimate the conductivities.

6.6.2.1 Indirect Determination of the Geoelectric Field

Generally, the reverse calculation procedure can be performed for the transformer, line and substation currents. Due to the existing measurements in the transformer neutral, the calculations are outlined for the transformer neutral current measurements.

The lines and transformers only have connections to the network nodes N_{Net} , whose nodal voltages depicts by V_N . Therefore, the BNM_{Tra} matrix is reduced to BNM_{Tra}^{DC} with the size $N_{Tra} \times N_{Net}$. This means that all columns from the transformer branch-network matrix corresponding to V_S , can be neglected, because they are all zero. For example, select the second row of formula (6-30) to calculate the transformer currents by the reduced branch-network matrix, as shown in (6-34).

$$I_{Tra}^{DC} = BNM_{Tra}^{DC} \cdot V_N \quad (6-34)$$

BNM_{Tra}^{DC} reduced transformer branch-node matrix with size $N_{Tra} \times N_{Net}$
 I_{Tra}^{DC} measured transformer neutral current matrix with size $N_{Tra} \times t$

Afterwards equation (6-27) and (6-29) are inserted into formula (6-34) to calculate the network system matrix C_{Tra} for the transformer as quoted in (6-35).

$$\begin{aligned} I_{Tra}^{DC} &= BNM_{Tra}^{DC} \cdot V_N \\ &= -BNM_{Tra}^{DC} \cdot inv(Y_N) \cdot Y_C \cdot V_S \\ &= -BNM_{Tra}^{DC} \cdot inv(Y_N) \cdot Y_C \cdot [L_x \quad L_y] \cdot \begin{bmatrix} E_x \\ E_y \end{bmatrix} \\ &= C_{Tra}^{DC} \cdot E^{DC} \end{aligned} \quad (6-35)$$

C_{Tra}^{DC} reduced transformer system network matrix with size $N_{Tra} \times 2$
 E^{DC} geoelectric field from DC measurement with size $2 \times t$

The geoelectric field E^{DC} can be calculated from the transformer measurements I_{Tra}^{DC} and reduced transformer system network matrix C_{Tra}^{DC} by rearranging equation (6-35) as quotes formula (6-36). To determine the geoelectric field in northward and eastward direction, a minimum of two measurements are needed. Therefore, the system network matrix C_{Tra}^{DC} has to be adopted to the corresponding lines according to the applied measurements data.

$$E^{DC} = inv(C_{Tra}^{DC}) \cdot I_{Tra}^{DC} \quad (6-36)$$

For example using two measurement data, the (unique) inverse of the reduced transformer system network matrix C_{Tra}^{DC} with the size 2×2 is used to compute the E_x and E_y values, based on the two measurement data. By using more than two transformer neutral measurement data, the linear equations are overdetermined. In that case, the so-called pseudoinverse of the non-square matrix C_{Tra}^{DC} with the size $N_{Tra} \times 2$ is calculated. Due to the overdetermination of the initial linear equations, the pseudoinverse yields to an approximation of the geoelectric field.

The reverse computations are performed for the 400 kV clients #01, #02a, #03 and #05 because the 230 kV clients have no sufficient correlations. The observation time is the same 2 days as in the 400 kV transformer neutral current studies from 07. – 08. September 2017 with the sample rate of 1 s. Additionally, the results of the grounding resistance from the optimisation in subchapter 6.6.1 are considered. Results of E^{DC} in northward E_x^{DC} and eastward E_y^{DC} direction are

plotted in Figure 6-16. Furthermore, the original geoelectric field from the magnetic field and earth conductivity model #39 are added in the figure.

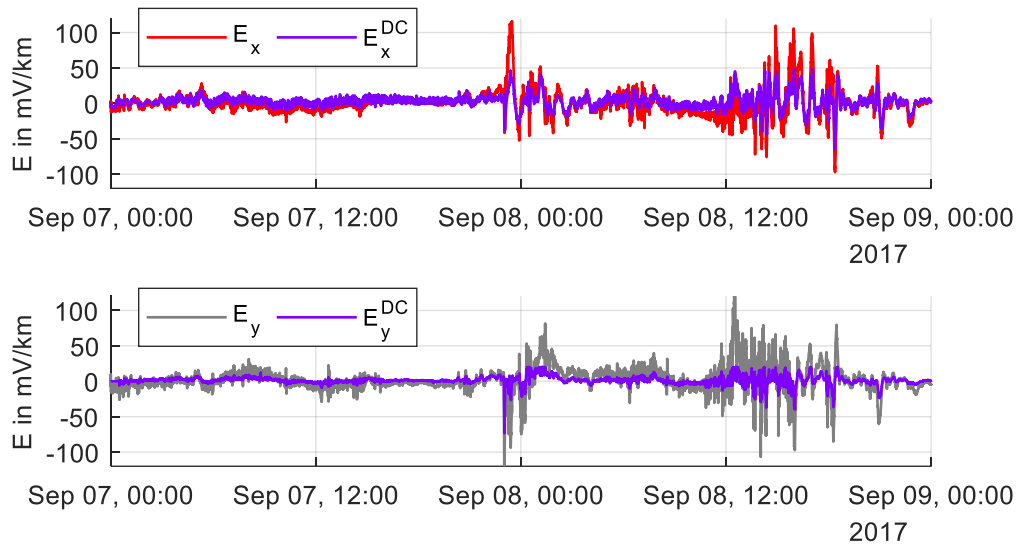


Figure 6-16 Reverse calculation of the geoelectric field E_x^{DC} and E_y^{DC} from the transformer neutral current measurement and optimised grounding resistances (violet curves) and calculated geoelectric field E_x and E_y based on the measured geomagnetic field and the earth model #39 (red/grey curves). The upper subplot shows the northward and the subplot below the eastward geoelectric field component. Observation time from 07. – 08. September 2017 and 1 s sample rate.

The comparison between the two different geoelectric fields shows, that the signal characteristic is for both similar for the most part. Notable is that especially the peak amplitudes of the eastward component are lower in E_y^{DC} than for E_y .

To validate the reverse calculation operation, the geoelectric field E^{DC} was computed for any two arbitrary client measurement data. Afterwards, the reverse calculated geoelectric field E^{DC} was applied in the GIC computation procedure in the “correct” way as given in equation (6-31). The result of the transformer neutral currents by using formula (6-31) and E^{DC} perfectly correlates with the concerned transformer neutral current measurements, which were used to calculate E^{DC} . Therefore, the reverse calculation operation for E^{DC} is correct. By using more than two measurement data, the transformer neutral currents from E^{DC} approximate the initial measured currents because of the already mentioned overdetermined linear equations.

6.6.2.2 Indirect Determination of the Conductivities of the Earth Layers

After computing the geoelectric field E^{DC} from the measurements, the next step is to estimate the earth conductivity structure from the geoelectric and geomagnetic field. Therefore, the fields are transformed into frequency domain to compute the total surface impedance $Z(\omega)$ as stated by formula (6.15) and (6.16). Reordering those formulas for the reverse calculation shows, that there are two solutions for the total surface impedance, depending on which geoelectric and geomagnetic field component is used. The total surface impedance $Z_{xy}^{DC}(\omega)$ in formula (6-37) based on a northward geoelectric E_x^{DC} and eastward geomagnetic field B_y , whereas the surface impedance $Z_{yx}^{DC}(\omega)$ in formula (6-38) is computed the other way around.

$$Z_{xy}^{DC}(\omega) = \mu_0 \cdot \frac{E_x^{DC}(\omega)}{B_y(\omega)} \quad (6-37)$$

$$Z_{yx}^{DC}(\omega) = -\mu_0 \cdot \frac{E_y^{DC}(\omega)}{B_x(\omega)} \quad (6-38)$$

Z_{xy}^{DC}, Z_{yx}^{DC} total surface impedance in xy-component from DC measurement, [Ω]
 E_x^{DC}, E_y^{DC} northward and eastward geoelectric field from DC measurement, [$\frac{V}{m}$]

The next step is to calculate the conductivity σ_{opt} of each earth layer n according to the given thickness of model #39. An optimisation problem is formulated quoted in (6-39) - (6-40) and mainly holds the surface impedances Z^{DC} , based on the impedances Z_{xy}^{DC} or Z_{yx}^{DC} from measurements, and the optimised impedance $Z_{\sigma_{opt}}$, which refers to the searched conductivities. According to the assumption that the thickness d_n of each layer n and the total amount of layers N_{Lay} are known, the surface impedance $Z_{\sigma_{opt}}(\omega)$ can be calculated choosing any arbitrary conductivity value for each layer. Due to the impedance $Z_{\sigma_{opt}}(\sigma_{opt})$ depends only on the conductivities, the objective function is optimised to a minimum.

$$\min_{\sigma_{opt}} \sum (|Z_{\sigma_{opt}}(\omega)| - |Z^{DC}(\omega)|)^2 \quad (6-39)$$

$$Z^{DC}(\omega) = \{Z_{xy}^{DC}(\omega) \vee Z_{yx}^{DC}(\omega)\} \quad (6-40)$$

$Z_{\sigma_{opt}}$ total surface impedance to optimise, [Ω]
 Z^{DC} total surface impedance from DC measurement, [Ω]
 σ_{opt} optimised conductivity, [$\frac{1}{\Omega m}$]

Additional boundary conditions for the conductivity values have to be defined. Only positive values for the conductivities are physically correct and hence the limitations were adjusted to the minimum and maximum values for any conductivity layer in the European lithosphere study [76], [113].

A second boundary condition was set on the frequency range f_{opt} according to the relevant GIC time periods from the measurement analysis in subchapter 5.2.3. Therefore, the observed spectrum range for optimisation was limited from DC up to 1 mHz. Frequencies higher than those limit will influence the optimisation results in a negative way because those frequencies occur from other sources than the geomagnetic field. The mathematical expression of the boundary constraints are given in equation (6-41) and (6-42).

$$\frac{1}{100 \text{ k}\Omega\text{m}} \leq \sigma_{opt} \leq \frac{1}{0.1 \Omega\text{m}} \quad \forall n \in N_{Lay} \quad (6-41)$$

$$f_{opt} \leq 1 \text{ mHz} \quad (6-42)$$

N_{Lay} total amount of horizontal layers

For the optimisation¹¹ problem, the same two observation days are chosen as for calculating E^{DC} in Figure 6-16. The computed conductivities of the optimisation are quoted in Table 6-11 and illustrated in Figure 6-17.

Table 6-11 Optimisation of the layer conductivities, based on the optimised grounding resistances.

Layer n	Thickness d km	$Z_{\#39}$	Z_{xy}^{DC}	Z_{yx}^{DC}
		Conductivity σ 1/ Ωm	Conductivity σ 1/ Ωm	Conductivity σ 1/ Ωm
1	55	1 / 1000.0	1 / 590.5	1 / 119.0
2	45	1 / 300.0	1 / 410.4	1 / 92.4
3	half space	1 / 1000.0	1 / 236.0	1 / 82.4

It can be seen from the table that the conductivities from the optimisation algorithm are generally more evenly distributed than the original one. But it is noticeable, that the optimised resistances are of each layer from Z_{xy}^{DC} and Z_{yx}^{DC} are all lower, with the single exception of the middle layer of Z_{xy}^{DC} , than the given conductivities from $Z_{\#39}$. An explanation for the higher layer conductivities is that the reverse calculated geoelectric field E_x^{DC} and E_y^{DC} , based on the DC measurements, are lower than the computed geoelectric field E_x and E_y from the geomagnetic field as input. In contrast to Z_{xy}^{DC} , the computations of the Z_{yx}^{DC} significantly changed to lower resistances, roughly by a factor of ten. Due to the dependency of Z_{yx}^{DC} from the eastward geoelectric field E_y^{DC} and the northward geomagnetic field B_x , as quoted in (6-38), this can be explained by lower amplitudes in the frequency spectrum of the eastward geoelectric field E_y^{DC} from reverse calculation and therefore lower resistances.

¹¹ The optimisation problem was solved by the interior point algorithm.

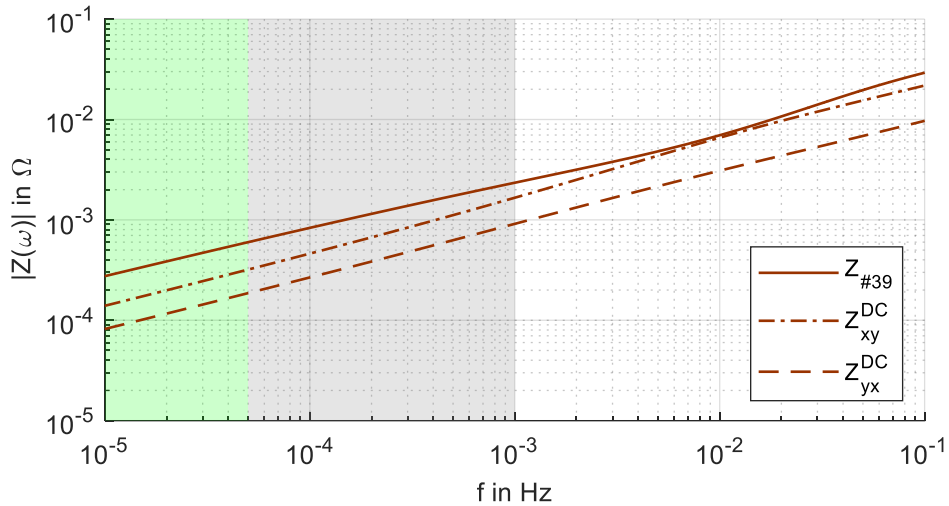


Figure 6-17 Optimised surface impedance of Z_{xy}^{DC} and Z_{yx}^{DC} compared to the original 1D-layered earth model $Z_{\#39}$ in frequency domain, based on the optimised grounding resistances. Observation time from 07. – 08. September 2017 with 1 s samples.

Applying the optimised surface impedance Z_{xy}^{DC} and Z_{yx}^{DC} instead of the original impedance $Z_{\#39}$ of the earth model for geoelectric field calculations and subsequently performing GIC computations by using the optimised grounding resistances R_G , following results can be stated from the correlation coefficient r_{XY} and over/underestimating coefficient β_1 between measurements and simulations, as given in Table 6-12:

- No relevant changes of the correlation value r_{XY} can be obtained between the different earth impedances
- The over/underestimating coefficient β_1 generally decreases for Z_{xy}^{DC} and Z_{yx}^{DC} , compared to $Z_{\#39}$. Due to the lower surface impedances of Z_{yx}^{DC} and Z_{xy}^{DC} , the computed geoelectric field is lower which yields to lower simulated GIC.

Table 6-12 Correlation and linear regression coefficient between measurements and simulations of each client, based on $Z_{\#39}$, Z_{xy}^{DC} , Z_{yx}^{DC} and the optimised grounding resistances R_G . Observation from 05. – 06. May 2018 and 1 s sample rate.

Client	$Z_{\#39}$		Z_{xy}^{DC}		Z_{yx}^{DC}	
	r_{XY}	β_1	r_{XY}	β_1	r_{XY}	β_1
-	-	-	-	-	-	-
#01	0.88	1.62	0.89	0.93	0.89	0.53
#02a	-	-	-	-	-	-
#02b	0.41	0.72	0.40	0.39	0.40	0.23
#03	0.79	0.37	0.78	0.21	0.79	0.12
#04	0.84	0.88	0.86	0.52	0.86	0.30
#05	0.92	4.02	0.93	2.35	0.93	1.35

6.7 Summary

It is shown that the usage of the plane-wave method is an adequate approach for mid-latitude regions and offers a simple and fast computation algorithm. A general method flow chart for GIC computations was illustrated based on the geophysical and power network model. The input parameters for the geophysical model, to compute the geoelectric field, is the horizontal geomagnetic field and the 1D-earth conductivity structure. The input parameters for the power network model, besides the computed geoelectric field from the geophysical model, covers the topology of the investigated power transmission network, geographical location of the substations and the resistances of the lines, transformer windings and substation groundings, due to the very low GIC frequency range. The applied power network model consists only of the 400 kV and 230 kV level because of the longer transmission lines and therefore higher values for the GIC driving source.

In general, the measurements and computations of the transformer neutral currents in the 400 kV result in good correlations, but are still not reaching their optimums. The correlation coefficient of the 230 kV transformer neutral currents leads to no acceptable values. The optimisation of the substation grounding resistances, on the basis of the transformer neutral measurements, concludes that the optimised grounding resistances tend to higher values. Generally, the correlation values are better by applying the optimised grounding resistances for GIC simulation, especially for the 230 kV client #04. Additionally, it is shown in this chapter that besides the uncertainties of the grounding resistances, the conductivities of the earth structure have significant effects on the computed GIC.

The sensitivity analysis of the transmission network shows, that several substations in the investigated power transmission network are at higher risk for higher GIC than others, which are determined by network topology and critical geoelectric field directions.

The last investigation concerns the improvement of the geophysical model. The approach based on the indirect determination of the earth conductivities, based on reverse calculation from the DC field measurements. Results of the indirect determination are that the earth resistances tend to be lower than the given (original) earth model. The application of the optimised earth layers to compute the GIC and the subsequent comparison to the measurements shows, that there are no notable changes of the correlation values, but the simulation underestimates the transformer neutral currents in general.

7 CONCLUSION AND FUTURE WORK

Motivated by unexpected higher noise level of transformer in the field installation, investigations on the causes have been started. The spectrum analysis of the noise shows that DC components occur in the transformer neutral, which were not expected. Triggered by those observations, investigations were started to the subject on low-frequency transformer neutral currents in Austria. It turned out, that the main reason for those currents is from geomagnetic disturbances. The hazard of transformer half-cycle saturation and their consequences of increasing reactive power as rise of harmonics has to be considered for the whole transmission system network. Due to the wide-ranging GMD event, the impact on the power grid is not only locally restricted. Therefore, strong GMD events weaken the power system at all.

Low-frequency neutral point currents on transformers in Austria - What are the amplitudes and their distribution?

The geomagnetic activity analysis in the year 2017 shows, that strong geomagnetic activity occurs during 84 h in total. This information is relevant for TSO risk assessment to estimate the risk of high GIC and transformer exposure in the power system. During strong geomagnetic disturbances, the maximum amplitude of the geoelectric field reaches values close to 160 mV/km on the basis of the earth conductivity model #39. But most of the time the horizontal geoelectric field values were within the range of 30 mV/km. According to the highest geoelectric field value in 2017, the computed GIC in the Austrian transmission system reaches values of 10 A up to 20 A in several transformer neutrals. This matches the recordings of the developed DC monitoring system that shows for high geomagnetic activity transformer neutral currents in the range of about 5 A up to 15 A, depending on the location in the network topology. The measured amplitudes of the transformer neutral currents in the 230 kV power network are generally lower than in the 400 kV level.

For a 100 year worst-case scenario defined in [124], where the geoelectric field values are defined between 500 mV/km up to 2 V/km, the computation in critical stations reaches values between 20 A up to 100 A for a 500 mV/km geoelectric field and 100 A up to 400 A for a 2 V/km geoelectric field.

Low-frequency neutral point currents on transformers in Austria - What is the typical spectral distribution?

The FFT analysis of the field measurements, which consist of the DC transformer neutral currents and the geomagnetic field, shows that the frequency spectrum can be categorised in three main sections, according to their sources.

The first spectrum section ranges from 10 μ Hz up to 50 μ Hz, respectively cycles from 30 h down to 6 h. Within that range, significant frequency magnitudes of the 24 h, 12 h, 8 h and 6 h cycle are obtained in both, the DC transformer neutral currents and the geomagnetic field. The observed periods are characteristic for weak geomagnetic activity.

The second spectrum section ranges from 50 μ Hz up to 1 mHz, with the corresponding cycles between 6 h down to 15 min. From the frequency spectrum of both field measurements again is obtained, that the magnitudes of the entire spectrum section differ depending on the geomagnetic activity. If the geomagnetic activity is weak, the magnitudes within the frequency range are low. But for moderate or strong geomagnetic activity, the magnitudes within the same range considerably increase.

The last spectrum section is defined for frequencies above 1 mHz and occurs only in the spectrum of the transformer neutral current measurements. Especially for the clients, which are installed close to Vienna, significant magnitudes of the, for example, 15 min period can be observed, which may be caused from human activity, but not from geomagnetic activity. Therefore, the frequency range above 1 mHz is associated with man-made activities.

What are the sources of the very low frequency transformer neutral currents?

It is pointed out in this thesis, that two main sources can be determined from the field measurement analysis. The main cause of very low frequency currents in the transmission system is from the space weather ground effects and therefore the impact of geomagnetically induced currents. The GIC are continuously present in all substations and transformer windings. The reasoning behind this statement is firstly, the same significant frequencies in the spectrum of the current and geomagnetic field measurements as stated before, and secondly, the high correlation between the measurement and computation of the transformer neutral current in the transmission system. Especially the 400 kV measurements reach very high correlation values.

A second source, which could be clearly identified in this work, is the impacts of public transport DC operating systems on the 50 Hz power transmission system. This is obtained from the high-frequency fluctuations in the range of $\Delta t = 1$ s from the DC measurement units, which are installed in regions close to DC public transport systems. It has turned out, that the computed effective values on working days have always the same pattern, which is approximately zero in the early morning hours and increase to higher values for the rest of the day. Furthermore, the weekend and holidays are also characteristic because the effective values during those days are more or less at a constant level. This strongly indicate a human impact, which could be confirmed by simply looking on the operation time schedule for those public transport systems.

A third hypothesis of a so-called photoelectric effects, which cause potential difference between the substation groundings and therefore a more or less constant DC offset, could not been confirmed by this study.

How significant is the impact of geomagnetically induced currents in the power transmission grid for a mid-latitude region like Austria?

A crucial factor for higher GIC values in any transmission grid is the geomagnetic location to the north and south poles. This is due to the higher variations and further the derivation of the geomagnetic field yields to significant higher values closer to the geomagnetic poles than for mid-latitude regions. Another aspect is the structure of the earth conductivity. The higher the surface impedance, the higher are the geoelectric fields, which acts like a driving source for GIC. The third crucial point is the distance of the transmission line, respectively the distance between two transformer grounding points. Since the driving GIC voltage source depends on the path integral of the geoelectric field, long transmission distances mean higher voltage sources and therefore higher GIC.

Austria is a mid-latitude region, so the geomagnetic field variations are not that high as for northern or southern countries. Also the longest transmission line is “only” about 150 km long. But due to the Alps, the earth conductivities are one of the lowest in Central Europe and therefore higher GIC can occur in contrast to other countries in Central Europe. However, the GIC amplitudes are not that high as in countries close to the geomagnetic poles and longer transmission lines.

What earth conductivity model is valid for Austria and how reliable are the computations compared to the measurements?

It is outlined, that the most sensitive parameter for the GIC modelling is the earth surface impedance and therefore the 1D-layered earth structure, which determines the geoelectric field values. Two models exist for Austria to represent the mountainous regions. Applying both earth models for simulation, the model #39 yields slightly better correlations between measurements and computations. The decision on a more appropriate earth model, only based on the correlation coefficient, seems to be not sufficient in this thesis, although it is the main characteristic. Due to the over- and underestimation of the simulations, compared to the measurements, a second criteria was introduced based on the gradient of the linear regression trend line. Based on both coefficients, the earth model #39 is assumed to be more appropriate than the earth model #55.

The comparison of the simulations with the measurements shows that for the 400 kV transformer neutral currents, high correlation values are reached. But especially for peak values, when high geomagnetic activity occurs, the simulation tends to overestimate the currents as they are recorded by the monitoring system. Particularly the simulated amplitudes of client #05 are overestimated by a factor of 2.

However, for the 230 kV transformer neutral current, the correlation coefficient between measurement and simulation is low. It is shown that the optimisation of the grounding resistances, on the basis of the transformer neutral measurements, yields to partly better results of the 230 kV transformer neutral currents. Positive progress can be obtained for the measurement point of client #04, where the correlation changed to very high values. For the second measurement point (client #02b) in the 230 kV system, also improvements can be achieved by the optimisation.

Where are the endangered points in the Austrian transmission grid based on simulations?

It is pointed out, that the GIC values are generally higher for the 400 kV level due to longer transmission lines between two groundings and lower network resistances than for the 230 kV level. The occurrence of high GIC in the transformer depends generally on the topology of the power grid network and field orientation. This means that the GIC amplitudes are higher for substations and transformers, which are located at the ends of the voltage-level-subnetwork (stub-lines). Investigations on strong geoelectric field directions reveal that the critical orientation of the field occurs in northward, respectively northwestward direction. In the worst case, the stub-lines have the same direction as the critical geoelectric field orientation. In Austria, several of those stub-lines exist, especially in the 400 kV transmission system.

It is further shown that by completion the masterplan 2030 of the Austrian TSO, which include the changeover of several 230 kV transmission circuits to 400 kV level, this plan would generally decrease the GIC amplitudes in several substations in both voltage levels and therefore in the transformer windings.

Is it possible to determine reliable values of specified simulation model parameters based on the transformer neutral current measurements?

It has been shown that the determination of the grounding resistances by reverse calculation from the measurement data leads to better correlations between the current measurements and simulations, especially in the 230 kV system. However, the computed results of higher grounding resistances have to be questioned to represent realistic grounding conditions.

Additionally the transformer neutral current measurements are also used to determine the earth layers conductivities, based on the previous reverse computed grounding resistances. The reverse calculated geoelectric field values (from the current measurements) are generally lower than the

computed ones from the geomagnetic field. This can be explained by the lower, measured current amplitudes, which are the input parameters for the reverse calculation, and therefore lower, computed geoelectric field values. Based on the reverse computed geoelectric field, the surface impedances are calculated and by using an optimisation algorithm, the conductivity of each earth layer is determined. The results of the optimisation show, that the conductivities are more evenly distributed and generally lower than the original earth model, which concludes from the lower geoelectric field. However, the great difference between the two optimised earth impedances indicates, that the dominant surface impedance depends more on the northward geoelectric and the eastward geomagnetic field component than the other way around.

Future Work

Future work relating to the monitoring system may focus on installing more DC measurement systems in the transformer neutral in the Austrian transmission grid. Especially installing at exposed and endangered locations in the power grid will be vulnerable for GIC observation. An interesting and challenging part will be measurements installed in the 400 kV transmission lines to measure the very low DC currents besides the high AC load currents.

All the measurements will be also useful to adjust the simulation network parameters and for selective trials on transformer neutral switching, to refine the DC flow from the field measurements and network theory. Due to the particular geological structure in Austria, refining the simulation model towards to a 3D-earth conductivity model will be an interesting topic further. Another step in simulation will be a possible implementation of the GIC simulation model in TSO power flow computations, according to reactive var consumption of transformer during high GIC.

However, further investigations on determining the sources of the very low frequency currents in the transformer neutral, besides the geomagnetic disturbances and undergrounds / subways, should be performed. One question could consider the DC impacts of power electronics or converters from wind and solar power plants on the transmission grid, according to the neutral point currents. Beyond that, the influence of HVDC transmission systems to neighbouring substations with neutral grounding is a further interesting research field.

Furthermore, an operational GIC risk management should be implemented in the future, derived from the mentioned protection guidelines, in combination with space weather forecasting systems and possible effective countermeasures on the existing transmission grid in Austria. Additional evaluation of the settings of the relays in the power transmission grid due to harmonic sensitivities from transformer half-cycle saturation should be done.

Also interesting will be measurements of vibration of the transformer tank in order to evaluate the noise level change from the very low DC exposure.

8 REFERENCES

- [1] T. Halbedl, H. Renner, M. Sakulin, and G. Achleitner, ‘Measurement and analysis of neutral point currents in a 400-kV-network’, in *2014 Electric Power Quality and Supply Reliability Conference (PQ)*, 2014, pp. 65–68.
- [2] C. Clauser, *Einführung in die Geophysik*. Berlin, Heidelberg: Springer Berlin Heidelberg, 2016.
- [3] H. W. Newton, ‘Solar Flares and Magnetic Storms’, *Monthly Notices of the Royal Astronomical Society*, vol. 103, no. 5, pp. 244–257, Oct. 1943.
- [4] S. T. Suess and B. T. Tsurutani, Eds., *From the sun: auroras, magnetic storms, solar flares, cosmic rays*. Washington, DC: American Geophysical Union, 1998.
- [5] ‘GFZ German Research Centre for Geosciences’, *Helmholtz Centre Potsdam*, 2018. [Online]. Available: <https://www.gfz-potsdam.de/>.
- [6] ‘National Oceanic and Atmospheric Administration (NOAA)’, *National Centers for Environmental Information*, 2018. [Online]. Available: <https://www.ngdc.noaa.gov/stp/spaceweather.html>.
- [7] ‘World Data Center (WDC) for Geomagnetism, Kyoto’, 2018. [Online]. Available: <http://wdc.kugi.kyoto-u.ac.jp/index.html>.
- [8] J. Elovaara, P. Lindblad, A. Viljanen, T. Mäkinen, S. Larsson, and B. Kielen, ‘Geomagnetically Induced Currents in the Nordic Power System and their Effects on Equipment, Control, Protection and Operation’, presented at the Cigré SC36, Paris, 1992, vol. 36-301_1992.
- [9] A. Pulkkinen, *Geomagnetic induction during highly disturbed space weather conditions: studies of ground effects*. Helsinki: Finn. Meteorological Inst, 2003.
- [10] M. Lehtinen and R. Pirjola, ‘Currents produced in earthed conductor networks by geomagnetically induced electric fields.’, presented at the Annales Geophysivae, 1985, vol. 3(4).
- [11] L. Lanzerotti and G. Gregori, ‘The Natural Environment and Interactions with Man-made Systems’, in *The Earth’s electrical environment*, G. American Geophysical Union, Ed. Washington, D.C: National Academy Press, 1986.
- [12] C. W. Anderson, L. J. Lanzerotti, and C. G. MacLennan, ‘Outage of the L4 System and the Geomagnetic Disturbances of 4 August 1972’, *Bell System Technical Journal*, vol. 53, no. 9, pp. 1817–1837, Nov. 1974.
- [13] D. H. Boteler and R. J. Pirjola, ‘Nature of the geoelectric field associated with GIC in long conductors such as power systems, pipelines, and phone cables’, in *Electromagnetic Compatibility Proceedings, 1997 International Symposium on*, 1997, pp. 68–71.
- [14] D. H. Boteler and R. J. Pirjola, ‘Modeling geomagnetically induced currents: MODELING GIC’, *Space Weather*, vol. 15, no. 1, pp. 258–276, Jan. 2017.
- [15] *C57.163-2015 IEEE Guide for Establishing Power Transformer Capability while under Geomagnetic Disturbances. ///*
- [16] R. Carrington, ‘Description of a Singular Appearance seen in the Sun on September 1, 1859’, 1860, vol. Vol. 20, pp. 13–15.
- [17] R. Hodgson, ‘On a curious Appearance seen in the Sun’, 1860, vol. Vol. 20, pp. 15–16.
- [18] B. T. Tsurutani, ‘The extreme magnetic storm of 1–2 September 1859’, *Journal of Geophysical Research*, vol. 108, no. A7, 2003.
- [19] A. Pulkkinen, E. Bernabeu, J. Eichner, C. Beggan, and A. W. P. Thomson, ‘Generation of 100-year geomagnetically induced current scenarios: 100-YEAR SCENARIOS’, *Space Weather*, vol. 10, no. 4, p. n/a-n/a, Apr. 2012.
- [20] M. A. Shea and D. F. Smart, ‘Compendium of the eight articles on the “Carrington Event” attributed to or written by Elias Loomis in the American Journal of Science, 1859–1861’, *Advances in Space Research*, vol. 38, no. 2, pp. 313–385, Jan. 2006.
- [21] E. Loomis, ‘On the great auroral exhibition of Aug. 28th to Sept. 4th, 1859 and on auroras generally; 8th article’, *American Journal of Science*, vol. s2-32, no. 96, pp. 318–335, Nov. 1861.

- [22] D. S. Kimball, 'A Study of the Aurora of 1859', Geophysical Institute at the University of Alaska, Alaska, Scientific Report 6, Apr. 1960.
- [23] L. Bolduc, 'GIC observations and studies in the Hydro-Québec power system', *Journal of Atmospheric and Solar-Terrestrial Physics*, vol. 64, no. 16, pp. 1793–1802, Nov. 2002.
- [24] P. Czech, S. Chano, H. Huynh, and A. Dutil, 'The Hydro-Québec System Blackout of March, 13, 1989: System Response to Geomagnetic Disturbance', presented at the Geomagnetically Induced Currents, San Francisco, California, 1989, vol. Report TR-100450.
- [25] 'International Real-time Magnetic Observatory Network (INTERMAGNET)', 2018. [Online]. Available: <http://www.intermagnet.org/index-eng.php>.
- [26] NOAA, 'Intense Space Weather Storms October 19 - November 07, 2003', Silver Spring, Maryland, Service Assessment, 2004.
- [27] A. Pulkkinen, S. Lindahl, A. Viljanen, and R. Pirjola, 'Geomagnetic storm of 29-31 October 2003: Geomagnetically induced currents and their relation to problems in the Swedish high-voltage power transmission system: GEOMAGNETICALLY INDUCED CURRENTS', *Space Weather*, vol. 3, no. 8, p. n/a-n/a, Aug. 2005.
- [28] C. T. Gaunt and G. Coetzee, 'Transformer failures in regions incorrectly considered to have low GIC-risk', 2007, pp. 807–812.
- [29] R. A. Marshall, E. A. Smith, M. J. Francis, C. L. Waters, and M. D. Sciffer, 'A preliminary risk assessment of the Australian region power network to space weather: RISK ASSESSMENT AUSTRALIAN POWER NETWORK', *Space Weather*, vol. 9, no. 10, Oct. 2011.
- [30] A. J. Schwab, *Elektroenergiesysteme*. Berlin, Heidelberg: Springer Berlin Heidelberg, 2012.
- [31] E. C. Cherry, 'The Duality between Interlinked Electric and Magnetic Circuits and the Formation of Transformer Equivalent Circuits', *Proceedings of the Physical Society. Section B*, vol. 62, no. 2, pp. 101–111, Feb. 1949.
- [32] R. Fischer, *Elektrische Maschinen*, 12., neu Bearb. Aufl. München: Hanser, 2004.
- [33] M. J. Heathcote and D. P. Franklin, *The J & P transformer book: a practical technology of the power transformer*, 13th ed. Burlington, MA: Newnes, 2007.
- [34] S. Paul and R. Paul, *Grundlagen der Elektrotechnik und Elektronik 2*. Berlin, Heidelberg: Springer Berlin Heidelberg, 2012.
- [35] T. S. Molinski, 'Why utilities respect geomagnetically induced currents', *Journal of Atmospheric and Solar-Terrestrial Physics*, vol. 64, no. 16, pp. 1765–1778, Nov. 2002.
- [36] R. A. Walling and A. N. Khan, 'Characteristics of transformer exciting-current during geomagnetic disturbances', *IEEE Transactions on Power Delivery*, vol. 6, no. 4, pp. 1707–1714, Oct. 1991.
- [37] R. Girgis, K. Vedante, and K. Gramm, 'Effects of Geomagnetically Induced Currents on Power Transformers and Power Systems', presented at the Cigré - SC A2, Paris, 2012, vol. A2-304_2012, p. 8.
- [38] F. Bachinger, P. Hamberger, A. Leikermoser, G. Leber, and H. Passath, 'Direct Current in Transformers - Experience, Compensation', presented at the Cigré SC A2 & C4 Joint Colloquium, Zurich, 2013, p. 8.
- [39] W. McNutt, 'The effect of GIC on power transformers', in *Geomagnetic storm cycle 22: Power system problems on the horizon*, Minneapolis, 1990, pp. 32–37.
- [40] F. Bachinger *et al.*, 'Direct current in transformers: effects and compensation', *e & i Elektrotechnik und Informationstechnik*, pp. 1–5, 2012.
- [41] R. S. Girgis, M. S. Bernesjo, S. Thomas, J. Anger, D. Chu, and H. R. Moore, 'Development of Ultra-Low-Noise Transformer Technology', *IEEE Transactions on Power Delivery*, vol. 26, no. 1, pp. 228–234, Jan. 2011.
- [42] J. G. Kappenman, 'Geomagnetic Storms and Their Impact on Power Systems', *IEEE Power Engineering Review*, vol. 16, no. 5, p. 5, May 1996.
- [43] J. Raith and U. Schichler, 'Risk assessment of electrical equipment under the influence of GIC', 2016, pp. 341–344.

- [44] L. Marti, A. Rezaei-Zare, and A. Narang, ‘Simulation of Transformer Hotspot Heating due to Geomagnetically Induced Currents’, *IEEE Transactions on Power Delivery*, vol. 28, no. 1, pp. 320–327, Jan. 2013.
- [45] G. Hosemann, Ed., *Elektrische Energietechnik. Bd. 3: Netze*, 30., unveränd. Aufl. Berlin: Springer, 2001.
- [46] H. Renner and M. Sakulin, ‘Power Quality’, Graz, 2007.
- [47] R. P. Jayasinghe, ‘Investigation of Protection Problems due to Geomagnetically Induced Currents’, University of Manitoba, Canada, 1996.
- [48] ‘Geomagnetic disturbance effects on power systems’, *IEEE Transactions on Power Delivery*, vol. 8, no. 3, pp. 1206–1216, Jul. 1993.
- [49] NERC, ‘Effects of Geomagnetic Disturbances on the Bulk Power System - Interim Report’, NERC North American Electric Reliability Corporation, Atlanta, 2012.
- [50] ‘Geomagnetic Disturbances: Their Impact on the Power Grid’, *IEEE Power and Energy Magazine*, vol. 11, no. 4, pp. 71–78, Jul. 2013.
- [51] V. D. Albertson, J. G. Kappenman, N. Mohan, and G. A. Skarbakka, ‘Load-flow studies in the presence of geomagnetically-induced currents’, *IEEE transactions on power apparatus and systems*, no. 2, pp. 594–607, 1981.
- [52] G. Müller, B. Ponick, and G. Müller, *Grundlagen elektrischer Maschinen*, 9., völlig neu bearb. Aufl., 1. Nachdr. Weinheim: Wiley-VCH, 2009.
- [53] K. Heuck, K.-D. Dettmann, and D. Schulz, *Elektrische Energieversorgung: Erzeugung, Übertragung und Verteilung elektrischer Energie für Studium und Praxis*, 8., überarb. und aktualisierte Aufl. Wiesbaden: Vieweg + Teubner, 2010.
- [54] W. B. Gish, W. E. Feero, and G. D. Rockefeller, ‘Rotor heating effects from geomagnetic induced currents’, *IEEE Transactions on Power Delivery*, vol. 9, no. 2, pp. 712–719, Apr. 1994.
- [55] R. J. Pirjol, A. T. Viljanen, and A. A. Pulkkineni, ‘Research of Geomagnetically Induced Currents (GIC) in Finland’, 2007, pp. 269–272.
- [56] R. . Gummow and P. Eng, ‘GIC effects on pipeline corrosion and corrosion control systems’, *Journal of Atmospheric and Solar-Terrestrial Physics*, vol. 64, no. 16, pp. 1755–1764, Nov. 2002.
- [57] J. G. Kappenman, ‘Low-Frequency Protection Concepts for the Electric Power Grid - Geomagnetically Induced Current and E3 HEMP Mitigation - Metatech 2010.pdf’, Metatech Corporation, Goleta, Meta-R-322, 2010.
- [58] I. A. Erinmez, J. G. Kappenman, and W. A. Radasky, ‘Management of the geomagnetically induced current risks on the national grid company’s electric power transmission system’, *Journal of Atmospheric and Solar-Terrestrial Physics*, vol. 64, no. 5–6, pp. 743–756, Mar. 2002.
- [59] B. Kovan and F. de Leon, ‘Mitigation of Geomagnetically Induced Currents by Neutral Switching’, *IEEE Transactions on Power Delivery*, vol. 30, no. 4, pp. 1999–2006, Aug. 2015.
- [60] B. Bozoki *et al.*, ‘The effects of GIC on protective relaying’, *IEEE Transactions on Power Delivery*, vol. 11, no. 2, pp. 725–739, Apr. 1996.
- [61] I. A. Erinmez *et al.*, ‘Application of Modelling Techniques to Assess Geomagnetically Induced Current Risks on the NGC Transmission System’, presented at the Cigré - SC 39, Paris, 2002, vol. 39-304_2002, p. 10.
- [62] R. L. Bailey and R. Leonhardt, ‘Automated detection of geomagnetic storms with heightened risk of GIC’, *Earth, Planets and Space*, vol. 68, no. 1, Dec. 2016.
- [63] A. G. Hafez, E. Ghamry, H. Yayama, and K. Yumoto, ‘Systematic examination of the geomagnetic storm sudden commencement using multi resolution analysis’, *Advances in Space Research*, vol. 51, no. 1, pp. 39–49, Jan. 2013.
- [64] A. Pulkkinen *et al.*, ‘Solar shield: forecasting and mitigating space weather effects on high-voltage power transmission systems’, *Natural Hazards*, vol. 53, no. 2, pp. 333–345, May 2010.
- [65] J. G. Kappenman, ‘Geomagnetic Storms and Their Impacts on the US Power Grid’, Metatech Corporation, Goleta, Meta-R-319, 2010.

- [66] M. Lahtinen and J. Elovaara, ‘GIC occurrences and GIC test for 400 kV system transformer’, *IEEE Transactions on Power Delivery*, vol. 17, no. 2, pp. 555–561, Apr. 2002.
- [67] R. Pirjola, A. Viljanen, A. Pulkkinen, S. Kilpua, and O. Amm, ‘Ground Effects of Space Weather’, in *Effects of Space Weather on Technology Infrastructure*, I. A. Daglis, Ed. Dordrecht: Springer Netherlands, 2005, pp. 235–256.
- [68] J. M. Torta, L. Serrano, J. R. Regué, A. M. Sánchez, and E. Roldán, ‘Geomagnetically induced currents in a power grid of northeastern Spain: GICs IN A SPANISH POWER GRID’, *Space Weather*, vol. 10, no. 6, p. n/a-n/a, Jun. 2012.
- [69] M. B. Barannik, A. N. Danilin, Y. V. Kat’kalov, V. V. Kolobov, Y. A. Sakharov, and V. N. Selivanov, ‘A system for recording geomagnetically induced currents in neutrals of power autotransformers’, *Instruments and Experimental Techniques*, vol. 55, no. 1, pp. 110–115, Jan. 2012.
- [70] J. Koen and C. T. Gaunt, ‘Disturbances in the Southern African Power Network due to Geomagnetically Induced Currents’, presented at the Cigré SC 36, 2002, vol. 36-206_2002, p. 6.
- [71] C. Liu, Y. Li, and R. Pirjola, ‘Observations and modeling of GIC in the Chinese large-scale high-voltage power networks’, *Journal of Space Weather and Space Climate*, vol. 4, p. A03, 2014.
- [72] C.-M. Liu, L.-G. Liu, and R. Pirjola, ‘Geomagnetically Induced Currents in the High-Voltage Power Grid in China’, *IEEE Transactions on Power Delivery*, vol. 24, no. 4, pp. 2368–2374, Oct. 2009.
- [73] R. A. Marshall *et al.*, ‘Modeling geomagnetic induced currents in Australian power networks: Modeled GICs in Australian Power Network’, *Space Weather*, vol. 15, no. 7, pp. 895–916, Jul. 2017.
- [74] NERC and US Department of Energy, ‘High Impact, Low Frequency Event Risk to the Bulk Power System of North America’, Jun. 2010.
- [75] A. Viljanen, R. Pirjola, E. Prácsér, S. Ahmadzai, and V. Singh, ‘Geomagnetically induced currents in Europe: Characteristics based on a local power grid model: GIC CHARACTERISTICS IN EUROPE’, *Space Weather*, vol. 11, no. 10, pp. 575–584, Oct. 2013.
- [76] A. Ádám, E. Prácsér, and V. Wesztergom, ‘Estimation of the electric resistivity distribution (EURHOM) in the european lithosphere in the frame of the eurisgic WP2 project’, *Acta Geodaetica et Geophysica Hungarica*, vol. 47, no. 4, pp. 377–387, Dec. 2012.
- [77] ‘EURISGIC’, 16-Jul-2018. [Online]. Available: www.eurisgic.eu. [Accessed: 16-Jul-2018].
- [78] R. Girgis, K. Vedante, and G. Burden, ‘A process for evaluating the degree of susceptibility of a fleet of power transformers to effects of GIC’, 2014, pp. 1–5.
- [79] ‘CIGRE’, *SC C4 System Technical Performance*, 11-Jul-2018. [Online]. Available: <http://c4.cigre.org/WG-Area>. [Accessed: 11-Jul-2018].
- [80] ‘Zentralanstalt für Meteorologie und Geodynamik (ZAMG) - Conrad Observatory’, 2018. [Online]. Available: <http://www.zamg.ac.at>.
- [81] P. N. Mayaud, *Derivation, Meaning, and Use of Geomagnetic Indices*, vol. 22. Washington, D. C.: American Geophysical Union, 1980.
- [82] J. Bartels, ‘The technique of scaling indices K and Q of geomagnetic activity’, 1957, vol. Year 4, pp. 215–226.
- [83] J. Bartels, ‘The geomagnetic measures for the time-variations of solar corpuscular radiation, described for use in correlation studies in other geophysical fields’, 1957, vol. Year 4, pp. 227–236.
- [84] J. Bartels, N. H. Heck, and H. F. Johnston, ‘The three-hour-range index measuring geomagnetic activity’, *Journal of Geophysical Research*, vol. 44, no. 4, p. 411, 1939.
- [85] J. Bartels, ‘The Standardized Index Ks and the Planetary Index Kp’, presented at the IATME Bull 126, Paris, 1949.
- [86] M. Sugiura, ‘Hourly Values of Equatorial Dst for the IGY’, 1964, vol. Vol: 35.

- [87] L. von Wangenheim, *Analoge Signalverarbeitung: Systemtheorie, Elektronik, Filter, Oszillatoren, Simulationstechnik*, 1. Aufl. Wiesbaden: Vieweg + Teubner, 2010.
- [88] U. Tietze, C. Schenk, and E. Gamm, *Halbleiter-Schaltungstechnik: mit 189 Tabellen*, 11., völlig neu bearb. und erw. Aufl., 1. korr. Nachdr. Berlin: Springer, 2001.
- [89] T. Halbedl, H. Renner, and G. Achleitner, ‘Geomagnetically Induced Currents Modelling and Monitoring Transformer Neutral Currents in Austria’, presented at the CIGRE 2018, Paris, 2018.
- [90] Austrian Power Grid AG, ‘APG - Transmission Network’. [Online]. Available: <https://www.apg.at/de/netz/anlagen/leitungsnetz>. [Accessed: 01-Feb-2018].
- [91] M. Meyer, *Signalverarbeitung: analoge und digitale Signale, Systeme und Filter*, 8., verbesserte Auflage. Wiesbaden: Springer Vieweg, 2017.
- [92] A. V. Oppenheim, R. W. Schaffer, and J. R. Buck, *Discrete-time signal processing*, 2nd ed. Upper Saddle River, N.J: Prentice Hall, 1999.
- [93] G. Fischer, M. Lehner, and A. Puchert, *Einführung in die Stochastik: die grundlegenden Fakten mit zahlreichen Erläuterungen, Beispielen und Übungsaufgaben*, 2., neu Bearb. Aufl. Wiesbaden: Springer Spektrum, 2015.
- [94] J. W. Cooley and J. W. Tukey, ‘An Algorithm for the Machine Calculation of Complex Fourier Series’, 1965, pp. 297–301.
- [95] ‘FFTW’, *FFTW*, 01-Oct-2018. [Online]. Available: <http://www.fftw.org/>.
- [96] D. C. von Grünigen, *Digitale Signalverarbeitung: mit einer Einführung in die kontinuierlichen Signale und Systeme*, 5., neu Bearbeitete Auflage. München: Fachbuchverlag Leipzig im Carl-Hanser-Verlag, 2014.
- [97] ‘Wiener Linien’. [Online]. Available: <https://www.wienerlinien.at/>.
- [98] I. V. Hertel, C.-P. Schulz, and I. V. Hertel, *Atome und Grundlagen ihrer Spektroskopie*, 2. Auflage. Berlin: Springer Spektrum, 2017.
- [99] V. Quaschnig, *Regenerative Energiesysteme: Technologie - Berechnung - Simulation ; mit ... 117 Tabellen und einer DVD*, 8., aktualisierte und erw. Aufl. München: Hanser, 2013.
- [100] L. Cagniard, ‘BASIC THEORY OF THE MAGNETO-TELLURIC METHOD OF GEOPHYSICAL PROSPECTING’, *GEOPHYSICS*, vol. 18, no. 3, pp. 605–635, Jul. 1953.
- [101] J. R. Wait, ‘ON THE RELATION BETWEEN TELLURIC CURRENTS AND THE EARTH’S MAGNETIC FIELD’, *GEOPHYSICS*, vol. 19, no. 2, pp. 281–289, Apr. 1954.
- [102] D. H. Boteler, ‘Geomagnetically induced currents: present knowledge and future research’, *IEEE Transactions on Power Delivery*, vol. 9, no. 1, pp. 50–58, 1994.
- [103] R. Pirjola, ‘Electromagnetic Induction in the Earth by a Plane Wave or by Fields of Line Currents Harmonic in Time and Space’, in *Geophysica*, 1982, vol. Vol. 20, Nos. 1-2, pp. 1–161.
- [104] O. Amm and A. Viljanen, ‘Ionospheric disturbance magnetic field continuation from the ground to the ionosphere using spherical elementary current systems’, *Earth, Planets and Space*, vol. 51, no. 6, pp. 431–440, Jun. 1999.
- [105] D. H. Boteler, R. Pirjola, and L. Trichtchenko, ‘On calculating the electric and magnetic fields produced in technological systems at the Earth’s surface by a “wide” electrojet’, *Journal of Atmospheric and Solar-Terrestrial Physics*, vol. 62, no. 14, pp. 1311–1315, Sep. 2000.
- [106] D. H. Boteler and R. J. Pirjola, ‘The complex-image method for calculating the magnetic and electric fields produced at the surface of the Earth by the auroral electrojet’, *Geophysical Journal International*, vol. 132, no. 1, pp. 31–40, 1998.
- [107] D. J. Thomson and J. T. Weaver, ‘The complex image approximation for induction in a multilayered Earth’, *Journal of Geophysical Research*, vol. 80, no. 1, pp. 123–129, Jan. 1975.
- [108] R. Pirjola, ‘Induction in power transmission lines during geomagnetic disturbances’, *Space Science Reviews*, vol. 35, no. 2, Jun. 1983.
- [109] A. J. McKay, ‘Goelectric Fields and Geomagnetically Induced Currents in the United Kingdom’, University of Edinburgh, Edinburgh, 2003.
- [110] J. T. Weaver, *Mathematical methods for geo-electromagnetic induction*. Taunton, Somerset, England : New York: Research Studies Press ; Wiley, 1994.

-
- [111] O. Georg, *Elektromagnetische Wellen: Grundlagen und durchgerechnete Beispiele*. Berlin Heidelberg New York Barcelona Budapest Hongkong London Mailand Paris Santa Clara Singapur Tokio: Springer, 1997.
- [112] Bo Dong, Zezhong Wang, D. Boteler, and R. Pirjola, 'Review of earth conductivity structure modelling for calculating geo-electric fields', 2013, pp. 1–5.
- [113] A. Ádám, I. Lemperger, A. Novák, E. Prácser, L. Szarka, and V. Wesztergom, 'Geoelectric Litosphere Model of the Continental Europe', MTA Research Centre for Astronomy and Earth Sciences, 2012.
- [114] L. Marti, A. Rezaei-Zare, and D. Boteler, 'Calculation of Induced Electric Field During a Geomagnetic Storm Using Recursive Convolution', *IEEE Transactions on Power Delivery*, vol. 29, no. 2, pp. 802–807, Apr. 2014.
- [115] D. H. Boteler, 'Calculating the voltages induced in technological systems during a geomagnetic disturbance', *IEEE transactions on electromagnetic compatibility*, vol. 41, no. 4, pp. 398–402, 1999.
- [116] D. H. Boteler and R. J. Pirjola, 'Modelling geomagnetically induced currents produced by realistic and uniform electric fields', *IEEE Transactions on Power Delivery*, vol. 13, no. 4, pp. 1303–1308, 1998.
- [117] APG, 'Masterplan 2030', Austrian Power Grid AG, Vienna, 2018.
- [118] ETH Zürich and FEN Forschungsstelle Energienetze, 'Geomagnetically Induced Currents in the Swiss Transmission Network', Research Centre for Energy Networks - ETH Zürich, Zurich.
- [119] R. Horton, D. Boteler, T. J. Overbye, R. Pirjola, and R. C. Dugan, 'A Test Case for the Calculation of Geomagnetically Induced Currents', *IEEE Transactions on Power Delivery*, vol. 27, no. 4, pp. 2368–2373, Oct. 2012.
- [120] D. H. Boteler and R. J. Pirjola, 'Comparison of methods for modelling geomagnetically induced currents', *Annales Geophysicae*, vol. 32, no. 9, pp. 1177–1187, Sep. 2014.
- [121] NERC, 'Application Guide - Computing Geomagnetically Induced Current in the Bulk-Power System', NERC North American Electric Reliability Corporation, Atlanta, 2013.
- [122] R. Pirjola, 'On Currents Induced in Power Transmission Systems During Geomagnetic Variations', *IEEE Power Engineering Review*, vol. PER-5, no. 10, pp. 42–43, Oct. 1985.
- [123] R. H. Rapp, 'GEOMETRIC GEODESY PART I', Apr-1991.
- [124] J. Taylor, 'Analysis of Geomagnetic Disturbance (GMD) Related Harmonics', Electric Power Research Institute, Palo Alto, 3002002985, 2014.
- [125] M. Lindinger, 'Nachweis globaler Erdungssysteme durch Messung und Berechnung von verteilten Erdungsanlagen', Graz University of Technology, Graz, 2012.

Appendix A Timescale of the Total Measurement Observation

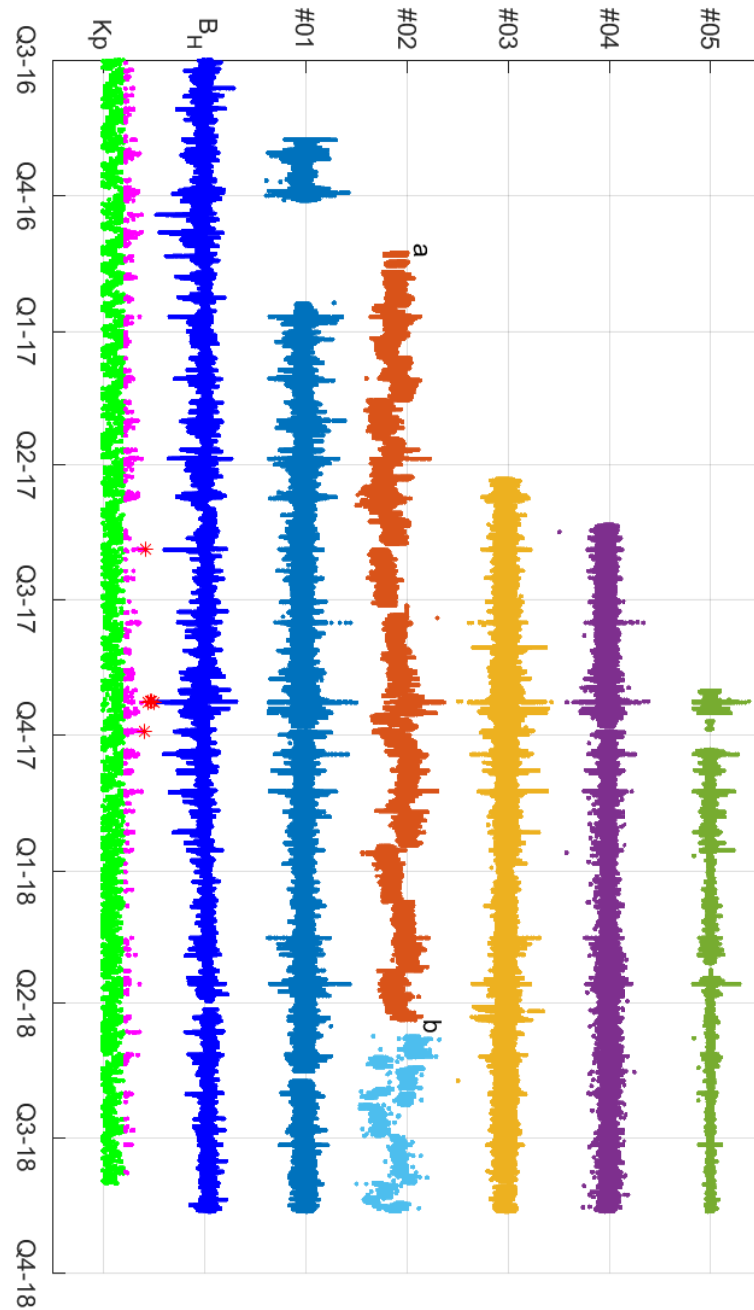


Figure 8-1 Timescale of the measured transformer neutral currents for all clients #01 to #05. All the measurements are in p.u. to the maximum magnitude during observation. For client #02 two installation points exist (tagged as *a* and *b*) which are separated by different colours. Additional data of the horizontal geomagnetic field component B_H and geomagnetic activity index K_p are added to complete the overview. The activity index K_p is classified into weak (green), moderate (magenta) and strong (red, stars).

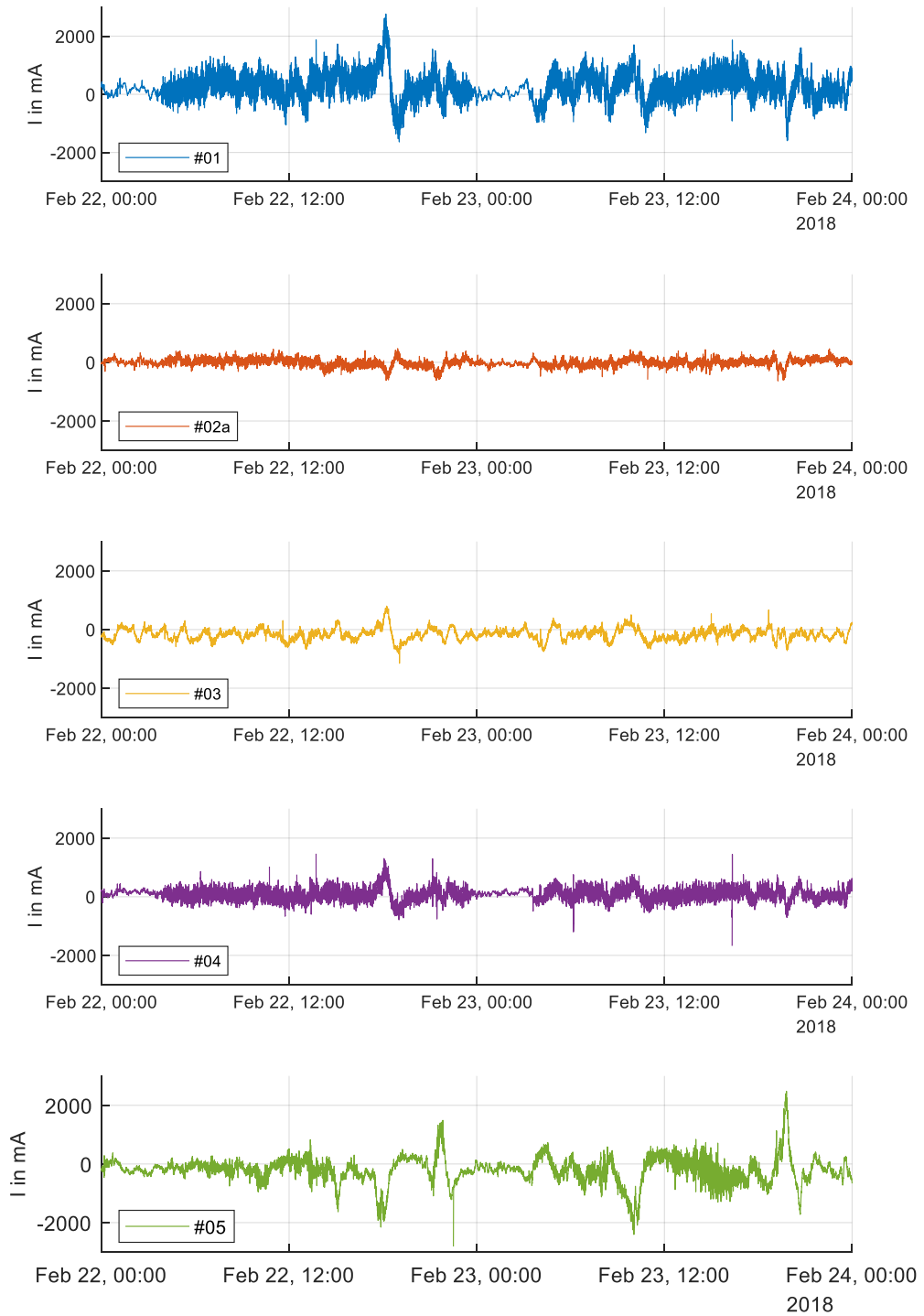


Figure 8-2 Measurements of the transformer neutral currents for each client with a sample rate of 1 s from 22. - 23. February 2018.

Appendix B Geoelectric Field based on the Geomagnetic Activity

The plotted geoelectric field from the 1D-layered earth model #39 in Figure 8-3 and Figure 8-4 are digitally low-pass filtered with $f_c = 1$ mHz and reduced to 1 minute samples for better display.

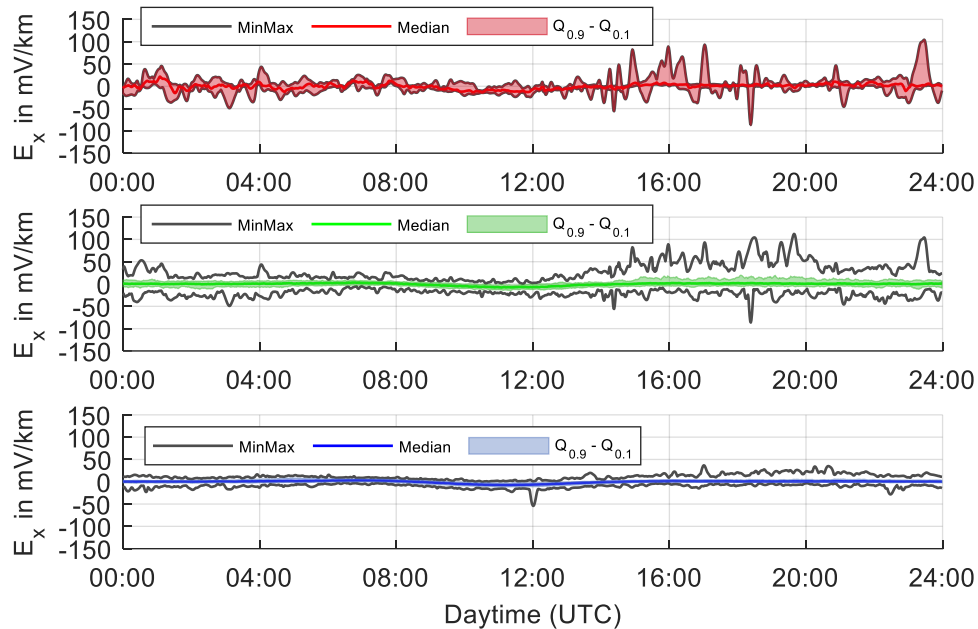


Figure 8-3 Northward geoelectric field for strong (red), moderate (green) and weak (blue) geomagnetic activity in the year 2017. Displayed are the minimum, maximum, median and envelope curve of the 10 %- and 90 %-quantiles.

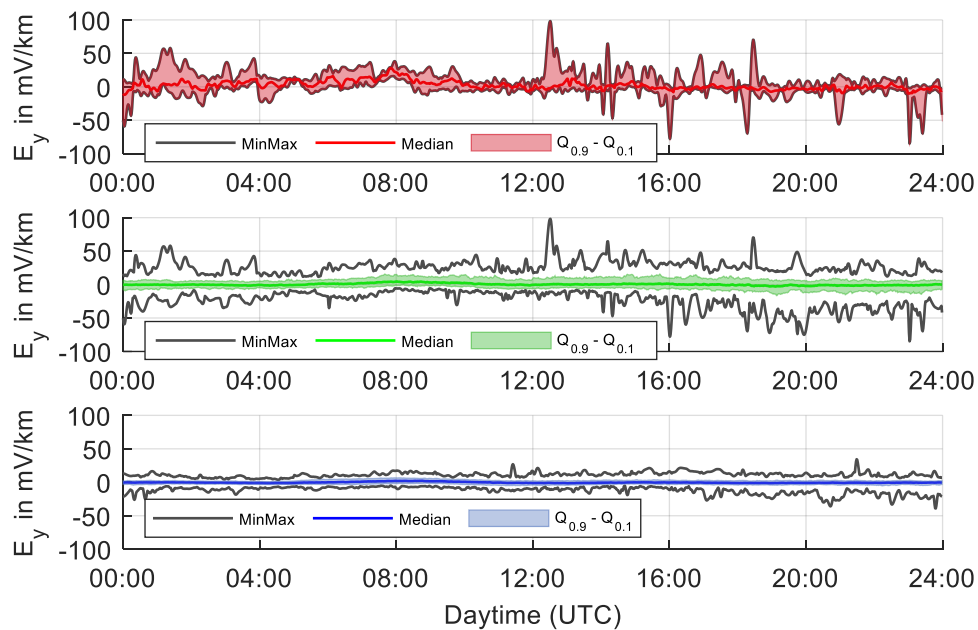


Figure 8-4 Eastward geoelectric field for strong (red), moderate (green) and weak (blue) geomagnetic activity in the year 2017. Displayed are the minimum, maximum, median and envelope curve of the 10 %- and 90 %-quantiles.

Appendix C Seasonal Geoelectric Field Directions

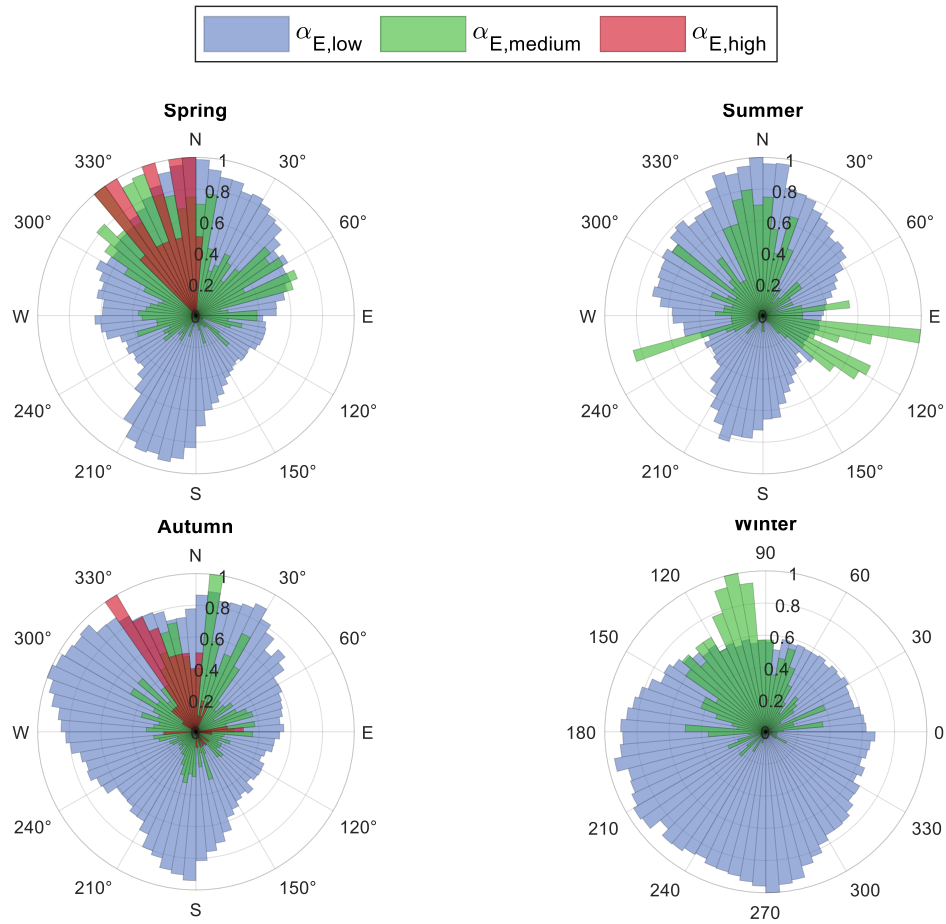


Figure 8-5 Seasonal polar histogram (in p.u.) of the geoelectric field angle α_E during a one year observation in 2017.

Table 8-1 Bin count of the seasonal polar histogram.

	Angle of the Geoelectric Field	Total Count	Maximum Bin Count
Spring	$\alpha_{E,low}$	131 362 #	2 817 #
	$\alpha_{E,medium}$	1 091 #	44 #
	$\alpha_{E,high}$	15 #	2 #
Summer	$\alpha_{E,low}$	132 041 #	3 066 #
	$\alpha_{E,medium}$	417 #	20 #
	$\alpha_{E,high}$	-	-
Autumn	$\alpha_{E,low}$	128 128 #	2 473 #
	$\alpha_{E,medium}$	1 393 #	67 #
	$\alpha_{E,high}$	77 #	10 #
Winter	$\alpha_{E,low}$	127 226 #	2 422 #
	$\alpha_{E,medium}$	501 #	28 #
	$\alpha_{E,high}$	-	-

Appendix D Map of Austria with Substation Numbers

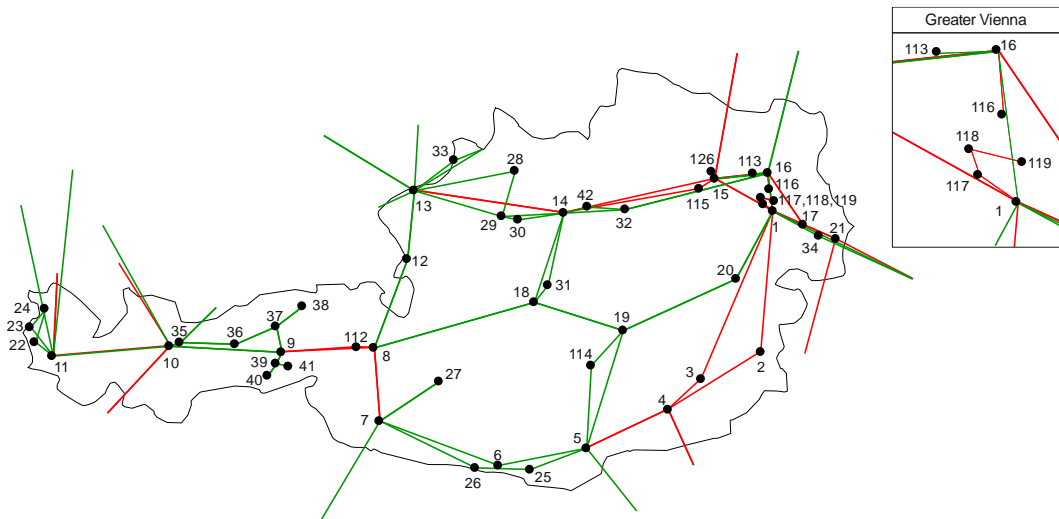


Figure 8-6 Map of Austria with substation numbers.